# Growth properties of carbon nanomaterials: towards tuning for electronic applications

Proefschrift voorgelegd tot het behalen van de graad van doctor in
de wetenschappen aan de Universiteit Antwerpen te verdedigen door

**Charlotte Vets**

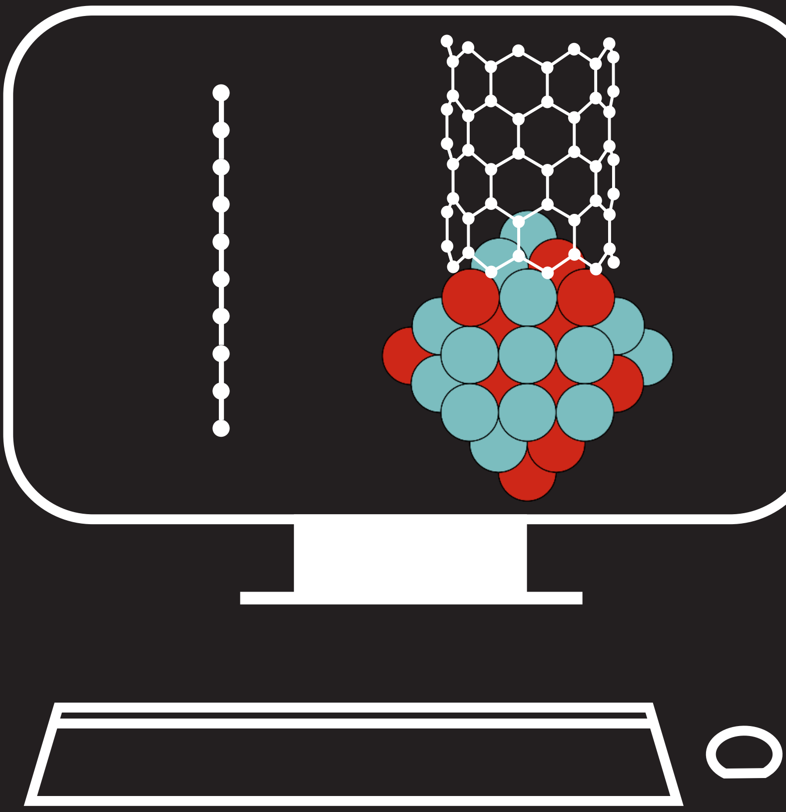

Promotor
prof. dr. Erik Neyts

Faculteit Wetenschappen
Departement Chemie
Antwerpen 2020

Universiteit
Antwerpen

Universiteit
Antwerpen

Faculteit Wetenschappen
Departement Chemie

# Growth properties of carbon nanomaterials: towards tuning for electronic applications

Proefschrift voorgelegd tot het behalen
van de graad van doctor in de wetenschappen
aan de Universiteit Antwerpen
te verdedigen door

Charlotte Vets

Promotor: prof. dr. Erik Neyts

Antwerpen, 2020

*Possunt quia posse videntur.*

Vergilius, Aeneis

# Contents

# List of Figures

# List of Tables

# Dankwoord

Vier jaar werken aan een doctoraat met regelmatig tegenvallende resultaten was helemaal niet makkelijk. Ik heb moeilijke periodes gekend en zou dit proefschrift niet geschreven hebben zonder hulp en steun uit mijn omgeving. Aan de andere kant waren er natuurlijk ook goede periodes en heb ik enorm veel geleerd uit dit doctoraat.

Ik wil beginnen met mijn promotor Prof. Dr. Erik Neyts te bedanken. Voor het vertrouwen om mij een doctoraat te laten beginnen, om me te helpen een IWT/FWO-SB beurs in de wacht te slepen, en om klaar te staan wanneer er wetenschappelijke problemen opdoken. Wanneer de problemen te groot werden en ik twijfelde om ermee te stoppen, heb je naar oplossingen gezocht om mijn project weer nieuw leven in te blazen. Heel erg bedankt daarvoor! Bedankt ook aan Prof. Dr. Annemie Bogaerts. Zo'n vierenhalf jaar geleden stuurde ik haar uit het niets een mailtje met de boodschap dat ik graag in haar onderzoeksgroep een doctoraat wou beginnen, en ik kreeg de kans om langs te komen en te praten over de mogelijkheid voor een doctoraat.

During my PhD, I was lucky enough to go to the Luleå Tekniska Universitet for a research stay. I learned a lot from my hosts there, Dr. Daniel Hedman and Prof. Dr. Andreas Larsson. I want to thank you for giving me the opportunity to learn from you, for the discussions during and after my stay, and for the nice collaboration. Tack så mycket!

A thank you to my colleagues in the PLASMANT and LADCA groups for the talks during lunch, just between work, and also the help and discussions about science. A few people I want to mention especially. Umid for the nice collaborations we did. Kristof for helping me out with simulation issues and for the talks when we happened to run into each other at workshops. Stijn, for helping me out with starting work on supercomputers and using DFT, you were so helpful to me in the beginning of my PhD, I really don't know how I would've done it without your help. Yannick and Parisa for being my office mates during most of my PhD. I really liked our office. Additional thanks to Yannick for simulation discussions. Parisa, you became a true friend during this time. I will miss our talks in the future, but I hope we will remain friends even though we won't see so much of each other anymore.

Voor alle administratieve en technische hulp wil ik Fabiana, Ingrid, Luc, Karel, Tania en Anita bedanken. Bedankt ook aan het CalcUA team voor alle hulp met supercomputerproblemen. Prof. Dr. Dirk Lamoen wil ik bedanken voor de hulp met DFT. Tine, Els en Barbara van het Levenslag Leren team: dankzij jullie heb ik de kans gekregen om me te verdiepen in wetenschapscommunicatie en me hierin verder te ontplooien. Dat heeft me veel leuke momenten opgeleverd tijdens mijn doctoraat en het heeft me zelfs geholpen om oude interesses nieuw leven in te blazen. Bedankt!

Aan mijn vrienden Stephanie, Jantiene, Nele, Annelies, Jonas, Marijn, Mark, Gertjan en Bart: de momenten waarop we afspraken waren altijd een lichtpuntje om naar uit te kijken. Ook op momenten dat het met mijn doctoraat niet zo goed ging, kon ik met jullie altijd praten, maar ook lachen en lekker gek doen. Net wat ik op zulke momenten nodig had. Dikke merci!

En dan als laatste mijn familie. Over dit stukje heb ik heel lang moeten nadenken. Nu denken jullie misschien: Oei, dat klinkt niet meteen positief. Integendeel. Jullie hebben zoveel voor me gedaan en voor me betekend, dat ik het gevoel heb dat een simpel bedankje hier niet genoeg is. Want zonder jullie hulp zou ik hier niet geraakt zijn. Zonder jullie steun had ik mijn doctoraat niet volgehouden. En zonder jullie onwankelbaar geloof in mij, had ik misschien niet genoeg in mijzelf kunnen geloven. Oma en opa, heel mijn leven al staan jullie voor mij paraat, altijd bereid om me te helpen. Jullie hebben altijd het volste vertrouwen dat ik het ga kunnen en zijn altijd zo trots op me. Papa, jij kan me altijd laten lachen op een moment dat het wat moeilijker gaat, en zal voor de nodige afleiding zorgen, maar je steunt me ook wanneer ik dat nodig heb. Mama, eigenlijk ben je veel meer voor me dan dat. Je bent ook mijn beste vriendin en mijn psycholoog. Hoeveel uren jij kwijt bent aan mij een luisterend oor bieden, het zullen er ontelbaar veel zijn. Daarnaast bood je mij ook altijd oplossingen aan, suggesties voor verbetering, motiverende berichtjes op exact de juiste momenten. Je kan precies het juiste zeggen om mij te doen beseffen wat ik eigenlijk al lang wist. Zo hard bedankt, en hopelijk kan ik voor jou soms ook betekenen wat jij voor mij betekent. Jeroen, zonder mijn doctoraat hadden we elkaar waarschijnlijk nooit ontmoet. Jij bent zowat mijn rots in de branding geworden. Je hebt vele van mijn breakdowns meegemaakt, maar bent altijd kalm gebleven. Je gelooft in me en helpt me om meer in mezelf te geloven (met een Kampioenen-grapje dan nog wel, beter wordt het niet). Een enorm dikke merci!

# Summary

Carbon nanomaterials have shown tremendous promise for various types of electronic devices. Here we study carbon nanotubes and carbyne. Carbon nanotubes are extremely interesting as channel material in field-effect transistors, as interconnects in integrated circuits, and as thermal conductors, whereas carbyne shows promise for spintronic devices, for interconnecting molecular devices, and for thermal conductors too. As the electric properties of these materials are defined by their geometrical structures, which are in turn defined during their growth processes, controlling these growth processes is crucial for their use in electronic devices. This thesis will therefore try to elucidate the influence of some of the mechanisms important during growth, with a view to gaining more insight into how to tune the growth towards materials with specific electric properties. Exploring growth mechanisms of the carbon nanomaterials will be done using computer simulations, more specifically density functional theory (DFT) and molecular dynamics (MD).

Carbon nanotube growth requires a catalyst to break the precursor bonds and form a hexagonal carbon network. The edge structure of the hexagonal network i.e. its chirality, then defines the carbon nanotube's electric properties. Most often used catalysts are Ni, Fe or Co nanoparticles. However, bimetallic catalysts have been deemed promising for chirality control. Therefore, we did a combined DFT and Born-Oppenheimer MD study on stabilities of NiFe, NiGa and FeGa nanoparticles. During the growth process, carbon atoms dissolve in the catalyst nanoparticle, and we thus also study the effect of carbon dissolved in NiFe nanoparticles. We establish that nanoparticles with more Fe in the core and more Ga on the surface are more stable, and compare these results with well-known properties such as surface energy and atom size. Furthermore, we find that the nanoparticles become more stable with increasing carbon content, both at 0 K and at 700 K.

Both thermodynamic and kinetic mechanisms are at play in carbon nanotube growth. The thermodynamic mechanism will be studied through the carbon nanotube-catalyst adhesion energy using DFT calculations. Of the several kinetic mechanisms, defect healing is chosen, as it highly influences the chirality formation. Defect healing will be studied using classical MD.

First, we address the question whether the carbon nanotube-catalyst adhesion energy can be tuned using bimetallic catalysts in order to achieve chirality-selective growth. We analyse the adhesion energies of SWCNTs of various chi-

ralities on Fe, Ni and FeNi bimetallic nanoparticles. The atom distributions of the FeNi nanoparticles were chosen based on their stabilities as described earlier. Our results show that the adhesion energy can be tuned by changing the FeNi composition of the catalyst. Based on our findings, we conclude that for $Fe_{1.0}$, $Ni_{1.0}$ and $Fe_{0.5}Ni_{0.5}$ compositions the adhesion energy shows no chiral selectivity. However, for bimetallic catalysts of less equal compositions $Fe_{0.75}Ni_{0.25}$ and $Fe_{0.25}Ni_{0.75}$ our results point to zigzag and armchair selectivity respectively. The computational adhesion results are validated with and confirmed by existing experimental work on Ni and FeNi bimetallic catalysts.

Second, we address the influence of the defect-catalyst contact on defect healing. We explore the defect healing process through the stabilities of carbon nanotubes with 5-7 defects, Stone-Wales defects and vacancies, and evaluate them on five different Ni nanoparticles. Our study demonstrates that the structure of the nanoparticle contributes significantly to the defect healing process. Moreover, an impact on the relative defect stabilities is exhibited. These results not only support the proposed influence of metal-defect interface, but also make apparent a significant influence of the exact catalyst structure on the defect stabilities and defect healing process.

Lastly, we did not only study carbon nanotubes, but also carbyne. Carbyne is a novel material that has more recently attracted interest in nanotechnology. Similarly as for carbon nanotubes, the growth process of carbyne determines the resulting structural properties. We will demonstrate that this in turn also influences the carbyne's electric properties. Despite successfully having been synthesized within double walled carbon nanotubes, the carbyne growth mechanism is still elusive. However, it is known that this endohedral growth is dependent on the catalyst and the feedstock. We study the nucleation and growth mechanism of different carbon chains in a Ni-containing double walled carbon nanotube, using carbon and hydrocarbon precursors. We find that understanding the competitive role of the metal catalyst and the hydrocarbon is important to control the growth of one dimensional carbon chains, including Ni- or H-terminated carbyne. Also, we find that the electronic properties of the Ni-terminated carbyne can be tuned by steering the H concentration along the chain. These results suggest catalyst-containing carbon nanotubes as a possible synthesis route for carbyne formation.

# Samenvatting

Nanomaterialen van koolstof zijn veelbelovend voor verschillende elektronische toepassingen. Hier bestuderen we nanobuisjes van koolstof en carbyn. Nanobuisjes van koolstof zijn enorm interessant om te gebruiken als kanaalmateriaal in veldeffecttransistoren, als "interconnect" in geïntegreerde circuits, en als thermische geleiders, terwijl carbyn veelbelovend is voor toepassingen in "spintronics", voor moleculaire componenten, en ook voor thermische geleiders. Aangezien de elektrische eigenschappen van deze materialen gedefinieerd worden door hun geometrieën, die op hun beurt gedefinieerd worden tijdens hun groei, is het cruciaal om deze groei te controleren, opdat deze materialen gebruikt kunnen worden in bovenstaande elektronische toepassingen. Daarom proberen we met deze thesis de invloed van een aantal mechanismen die belangrijk zijn tijdens de groei, uit te klaren. Zo hopen we meer inzicht te krijgen in hoe de groei gestuurd kan worden richting materialen met specifieke elektrische eigenschappen. Computersimulaties, meer bepaald dichtheidsfunctionaaltheorie (DFT) en moleculaire dynamica (MD), zullen worden gebruikt om de groeimechanismen van koolstofbuisjes en carbyn te onderzoeken.

Om koolstofbuisjes te kunnen groeien, is er een katalysator nodig die de bindingen in de precursor kan breken en een hexagonaal koolstofnetwerk kan vormen. De randstructuur van dit hexagonaal netwerk, ofwel de chiraliteit, definieert de elektrische eigenschappen van het koolstofbuisje. De meest gebruikte katalysatoren zijn nanodeeltjes van Ni, Fe of Co. Uit experimenten komen bimetallische katalysatoren echter veelbelovend naar voren voor chiraliteitscontrole. Daarom deden we een studie met zowel DFT als Born-Oppenheimer MD naar stabiliteiten van NiFe, NiGa en FeGa nanodeeltjes. Tijdens de groei lossen koolstofatomen op in het katalytisch nanodeeltje, en daarom onderzoeken we ook het effect van opgelost koolstof in NiFe nanodeeltjes. We stellen vast dat nanodeeltjes met meer Fe in de kern en meer Ga op het oppervlak stabieler zijn, en vergelijken deze resultaten met gekende eigenschappen, zoals oppervlakenergie en atoomgrootte. Verder vinden we ook dat de nanodeeltjes stabieler worden met stijgende koolstofconcentratie, zowel op 0 K als op 700 K.

Zowel thermodynamische als kinetische mechanismen spelen een rol in de groei van koolstofbuisjes. Het thermodynamische mechanisme zal onderzocht worden door middel van de adhesie-energie tussen koolstofbuisje en katalysator, waarbij we gebruik maken van DFT-berekeningen. Uit de verschillende kinetische mechanismen werd defectheling gekozen, omwille van de hoge invloed op chiraliteitsvorming. Defectheling zal bestudeerd worden met behulp van klassieke MD.

Eerst bekijken we de vraag of de adhesie-energie tussen koolstofbuisje en katalysator kan gestuurd worden door het gebruik van bimetallische katalysatoren, om zo chiraliteitsselectieve groei mogelijk te maken. We analyseren de adhesie-energieën van koolstofbuisjes met verschillende chiraliteiten op Ni, Fe en FeNi nanodeeltjes. De atoomverdelingen werden gekozen op basis van hun stabiliteit, die we eerder besproken. Onze resultaten tonen aan dat de adhesie-energie gestuurd kan worden door de FeNi-samenstelling van de katalysator te veranderen. Gebaseerd op onze bevindingen, besluiten we dat de adhesie-energie voor $Fe_{1.0}$, $Ni_{1.0}$ en $Fe_{0.5}Ni_{0.5}$ geen chirale selectiviteit vertoont. Aan de andere kant wijzen onze resultaten voor $Fe_{0.75}Ni_{0.25}$ en $Fe_{0.25}Ni_{0.75}$ op een selectiviteit voor respectievelijk zigzag en “armchair” koolstofbuisjes. We valideren deze computationele resultaten met bestaand experimenteel werk op katalysatoren van Ni en FeNi, dat onze resultaten inderdaad bevestigt.

Daarna bekijken we de invloed op defectheling van het contact tussen het defect en de metaalkatalysator. We onderzoeken het proces van defectheling door middel van de stabiliteiten van koolstofbuisjes met 5-7 defecten, Stone-Wales defecten en vacatures, en evalueren deze resultaten op vijf verschillende Ni nanodeeltjes. Onze studie toont aan dat de structuur van de nanodeeltjes de defectheling significant beïnvloedt. Bovendien toont ze ook de impact op de relatieve stabiliteiten van de defecten. Deze resultaten ondersteunen niet enkel de hypothese van de invloed van het metaal-defectgrensvlak, maar maken ook de significante invloed van de exacte structuur van de metaalkatalysator op de stabiliteiten van de defecten en op het proces van defectheling duidelijk.

Uiteindelijk bestudeerden we ook carbyn. Carbyn is een nieuw materiaal dat sinds kort veel aandacht krijgt binnen de nanotechnologie. Gelijkaardig aan koolstofbuisjes, bepaalt de groei van carbyn de resulterende structurele eigenschappen. We tonen aan dat dit op zijn beurt ook de elektrische eigenschappen van carbyn beïnvloedt. Hoewel carbyn met succes is gesynthetiseerd in dubbelwandige koolstofbuisjes, is het groeimechanisme nog niet gekend. Het is echter wel duidelijk dat dit groeimechanisme afhankelijk is van de katalysator en het type precursor. We bestuderen de nucleatie en de groei van verschillende koolstofketens in een dubbelwandig koolstofbuisje dat Ni bevat, met koolstoffen en koolwaterstoffen als precursors. Het begrijpen van de competitie tussen de metaalkatalysator en de koolwaterstoffen is belangrijk om de groei van ééndimensionale koolstofketens te controleren. Door de waterstofconcentratie langs de keten te controleren, kunnen de elektrische eigenschappen van carbyn gestuurd worden. Deze resultaten suggereren dat koolstofbuisjes die een katalysator bevatten de synthese van carbyn kunnen stimuleren.

# 1 Carbon nanomaterials

Carbon nanomaterials have shown promise for various types of opto-electronic devices. In this thesis, two of such carbon nanomaterials, i.e. carbon nanotubes and carbyne were studied. The growth process of these materials is paramount for their use in opto-electronic devices. Therefore, we studied properties important for the growth processes. In the case of carbon nanotubes, we first did a study on potential catalysts for carbon nanotube growth. This chapter will first give a general overview of carbon nanomaterials for opto-electronic devices (section 1.1), and then a background on carbon nanotubes (section 1.2) and carbyne (section 1.3). The computational framework used in this thesis will be discussed in chapter 2 and the results are explored in chapter 3 - chapter 6. We will round up this thesis with the conclusions in chapter 7.

## 1.1 Carbon nanomaterials for opto-electronic applications

Carbon nanomaterials are promising for a plethora of opto-electronic applications. Well-known examples of carbon nanomaterials for opto-electronic applications are carbon nanotubes, graphene and fullerenes, but also less well-known examples such as carbyne have shown tremendous potential. These materials are represented in figures 1.1 and 1.2.

Graphene has been implemented in transistors experimentally,[1,2] whereas fullerenes have potential for organic photovoltaic applications.[3]

Carbon nanotubes (CNTs) are extremely attractive to use as channel material in field-effect transistors (FETs),[4,5] as interconnects in integrated circuits,[6] as thermal conductors,[7] and in gas sensors.[8] Figure 1.3 shows examples of these applications.

Carbyne on the other hand has shown promise for spintronic devices,[9] for interconnecting molecular devices,[10] and for thermal conductors.[11]

Interestingly, CNTs and carbyne have electronic properties that are structure-dependent. This allows for inherent tuning opportunities that do not require the assistance of e.g. an electric field, in contrast to graphene, rendering them useful for a wider variety of applications. For this reason, this thesis focuses on CNTs and carbyne. Sections 1.2 and 1.3 will elaborate on CNTs and carbyne, respectively.

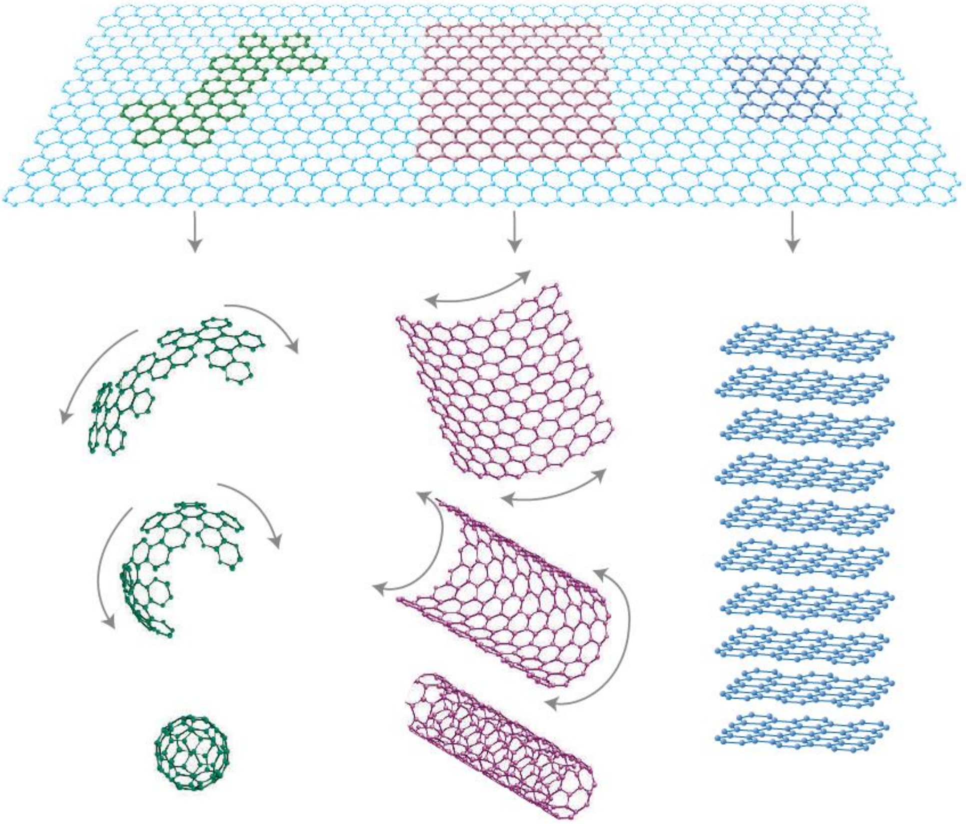

Figure 1.1: Top: Graphene (top) is a 2D carbon nanomaterial, and exists of one layer of graphite (right). From graphene, parts can be “cut out” and rolled up to make fullerene (left) and carbon nanotubes (middle).[12]

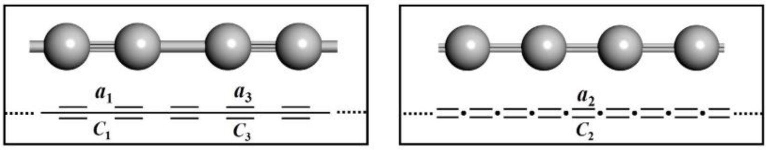

Figure 1.2: Carbyne exists in two forms: one in which triple and single bonds alternate (left), and one where all bonds are double bonds (right). The first form is called polyyne, the second cumulene.[11]

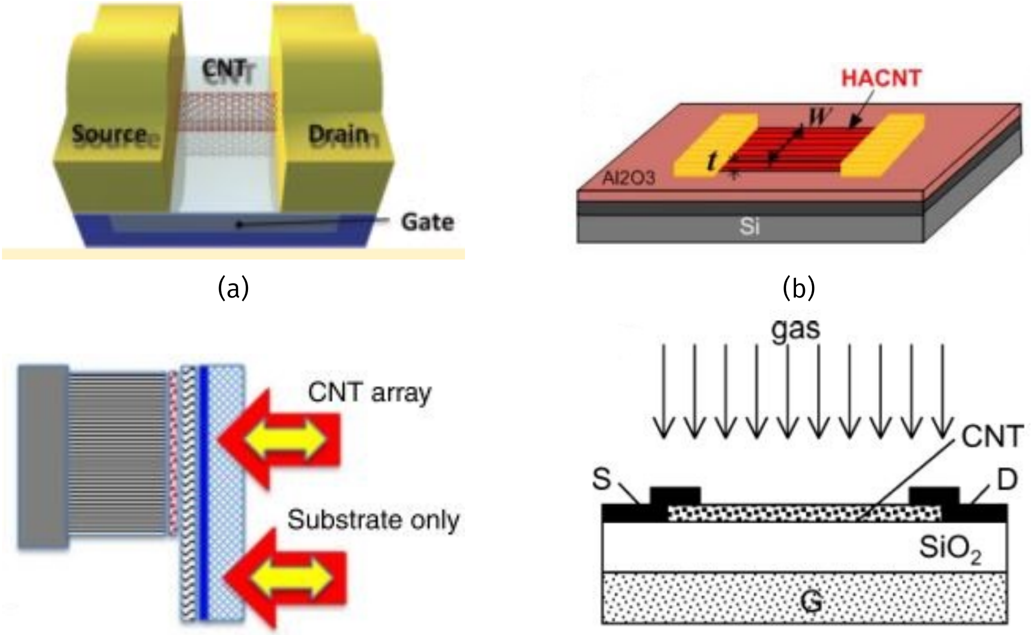

(a) (b) (c) (d)

Figure 1.3: Examples of electronic applications for which CNTs are promising: CNT as channel material in FET (figure 1.3a),[4] CNTs as interconnect in integrated circuit (figure 1.3b),[6] CNTs as thermal conductors (figure 1.3c),[7] and CNTs in gas sensors (figure 1.3d).[8]

## 1.2 Carbon nanotubes

### 1.2.1 Structure and properties

CNTs exist of one or more rolled up carbon monolayers, in which the carbon atoms are arranged in a hexagonal network (i.e. a layer of graphene). A non-exhaustive list of CNTs' outstanding properties are: a Young's modulus up to 4.15 TPa,[13] tensile strength up to 22.2 GPa,[14] ballistic transport,[15] current density up to $10^9$ A/cm$^2$,[16] a thermal conductance of 2.4 nW/K and thermal conductivity of 3500 Wm$^{-1}$K$^{-1}$ along its axis at room temperature,[17] high surface-volume ratio, and a high aspect ratio. We will focus on CNTs with only one rolled up monolayer, i.e. single-walled CNTs (SWCNTs). The monolayers can be rolled up along various chiral directions, leading to various chiralities. The chirality depends on the diameter of the CNT and on the roll direction, or chiral angle, of the monolayer,[18] as can be seen on the chirality map in figure 1.4 and on the CNTs in figure 1.5. SWCNTs with a chiral angle $\theta$ = 0° are zigzag SWCNTs, and SWCNTs with a chiral angle $\theta$ = 30° are armchair SWCNTs. All SWCNTs with 0°

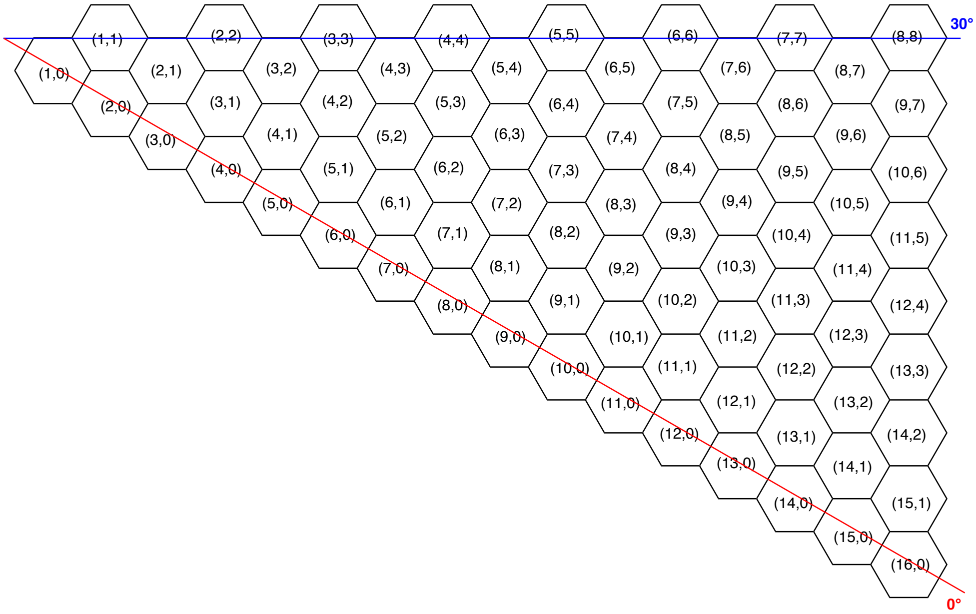

Figure 1.4: Chirality map. Along the red line, the zigzag tubes ($\theta$ = 0°) can be found, and along the blue line, the armchair tubes ($\theta$ = 30°) can be found.

$< \theta <$ 30° are called chiral SWCNTs. The relationships between chirality (n,m) and chiral angle $\theta$ and diameter d are given by equations 1.1 and 1.2, respectively. $\theta$ is expressed in degrees (°) and d in nm.

$$\theta = tan^{-1}\left(\frac{\sqrt{3}m}{2n+m}\right) \tag{1.1}$$

$$d = 0.0783\sqrt{n^2+m^2+nm} \tag{1.2}$$

SWCNTs' electronic properties depend on their structural properties, more specifically on their chirality. The large variety in chiralities thus leads to an equally large spread in electronic properties. For opto-electronic applications, the main property of interest is the band gap. SWCNTs can be either metallic or semiconducting, with various band gaps. If n-m $=$ 3k, with k an integer number, then the SWCNT is metallic. If n-m $\neq$ 3k, then the SWCNT is semiconducting. A detailed discussion of the SWCNT growth will be given in section 1.2.2, but SWCNT growth inevitably results in a distribution of chiralities, and hence in a distribution of band gaps.

This puts the use of SWCNTs in opto-electronic applications in jeopardy. A first example is the use of SWCNTs as channel material in FETs: for the FET to work

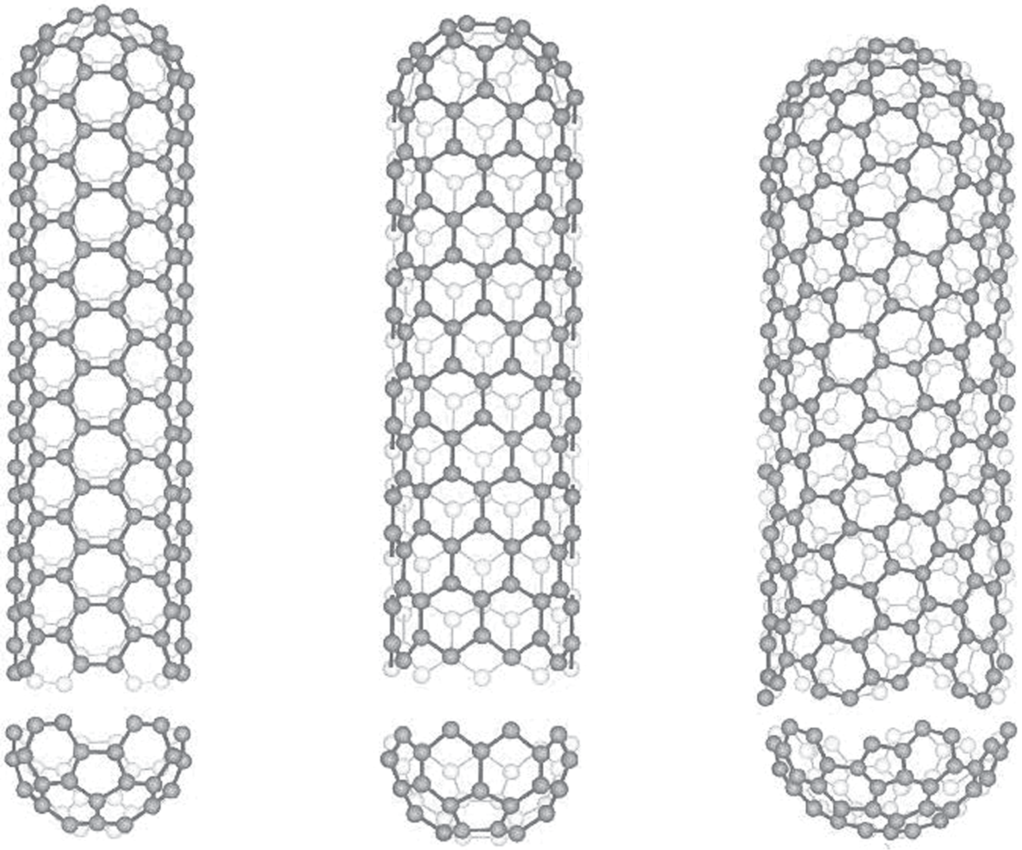

(a) (b) (c)

Figure 1.5: Examples of armchair ($\theta = 30°$), zigzag ($\theta = 0°$) and chiral ($0° < \theta < 30°$) CNTs in figures 1.5a, 1.5b and 1.5c, respectively. Adapted from Singh et al.[19]

properly, control over the channel material's band gap is paramount, and the band gap should be very well defined. This is not possible if we do not know upfront which chirality will be grown. The second example is the use of SWCNTs as interconnects in integrated circuits. Interconnects have to be metallic to conduct current in the integrated circuit. Again, if we don't know beforehand which type of SWCNTs we will end up with, it will be extremely difficult to use them in industrial applications.

To obtain SWCNTs that all have the same chirality, there are two options. We can either add a separation step after the growth process, or we can try to implement direct chirality-selective growth. Several separation methods exist, such as sorting, selective chemical etching or single-device electrical breakdown. In sorting, SWCNT solutions are spincoated onto funtionalized surfaces. Chirality can then be tuned by selecting the right surface functional groups.[20] In selective chemical etching, a chemical process is used to remove metallic SWCNTs from the mix. Various possibilities exist for the chemicals to be used, e.g. a methane plasma.[21] Single-device electrical breakdown applies high voltage to aligned CNTs. This will cause the metallic CNTs to breakdown, while the semiconducting CNTs are turned off.[5,22] There are however some disadvantages to separation methods: they are expensive, time-consuming, a large part of the material grown is lost, and the quality of the material remaining after separation decreases. Therefore, direct chirality-selective growth is preferred. Here, we try to influence parameters of the growth process to tune the product coming out of the growth process. This method will be elaborated on in section 1.2.2.

### 1.2.2 Catalytic growth

The main method to grow CNTs is catalytic chemical vapour deposition (CCVD). Here, a catalyst is present on a horizontal substrate. During the CCVD process, a precursor gas is decomposed on the surface of the catalyst. Precursors for CNT growth are e.g. methane,[24] carbon monoxide,[25] or ethanol.[26] Carbon atoms subsequently dissolve in the catalyst until eventually a carbon network precipitates on the catalyst surface due to excess carbon in the catalyst. This process, called the vapour-liquid-solid (VLS) model, is shown schematically in figure 1.6. Another possibility is that the catalyst remains solid and that carbon diffuses over the catalyst surface before a carbon network is formed, which is the vapour-solid-solid (VSS) growth model.[27–29] After the precursor has reacted with the catalyst to form CNTs, volatile by-products are formed, which are removed again.

There are many possible materials to use as catalyst, such as metallic catalysts, SWCNT seeds,[30] or $SiO_2$.[31] Metallic catalysts are by far the most widely used, and are needed in CCVD. Usually, these catalysts come in the form of na-

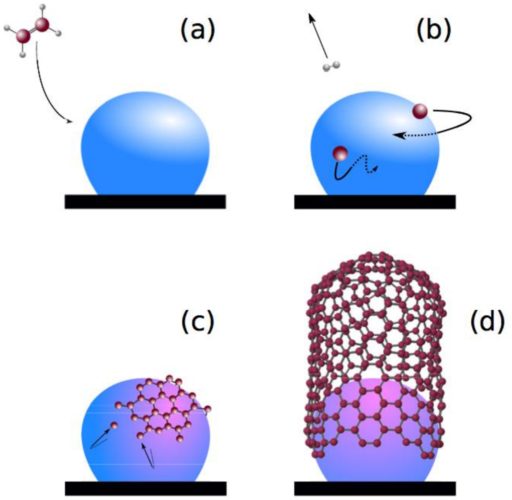

Figure 1.6: Schematic of the VLS model for CNT growth on a metal catalyst: the precursor falls onto the metal NP (a), and subsequently decomposes on the NP (b). The by-product is removed, while the carbon atoms dissolve in the NP (b), until a carbon network is formed on the surface of the NP (c). The hexagonal network will grow to eventually form a CNT (d).[23]

noparticles (NPs).[32] In this thesis, we study metallic NPs for catalysts. CNTs grown on metallic NPs can have either a diameter similar to the one of the NP, or a diameter smaller than the one of the NP. Consequently, two growth modes emerge, defined by the ratio of CNT diameter on NP diameter. These growth modes are called tangential and perpendicular mode respectively,[33] and are depicted in figure 1.7.

The catalyst needs to fulfil three conditions: first, it needs to decompose the precursor gas, second, it needs to form CNT-caps on its surface, and third, it needs to stabilize the growing end of the CNT for it to retain its hollow structure. Hence, the catalyst-carbon interaction must be strong enough to retain a hollow CNT end, while at the same time this interaction must not be too strong so as to prevent metal carbide formation. This is called the Goldilocks principle. Only a few metals, such as Ni, Fe, and Co, lie insie this Goldilocks zone. Ni, Fe, and Co NPs are in fact typically used as catalysts for CNT growth. And yet, the strength of the catalyst-carbon interaction can also be tuned by combining two metals of which one forms a weak and the other a strong bond with carbon.[18]
As discussed in section 1.2.1, CNTs' electronic properties are governed by their chirality, and when growing CNTs with the traditional monometallic NPs, such as Ni, Fe and Co, one ends up with a wide spread in chiralities. As the chirality is

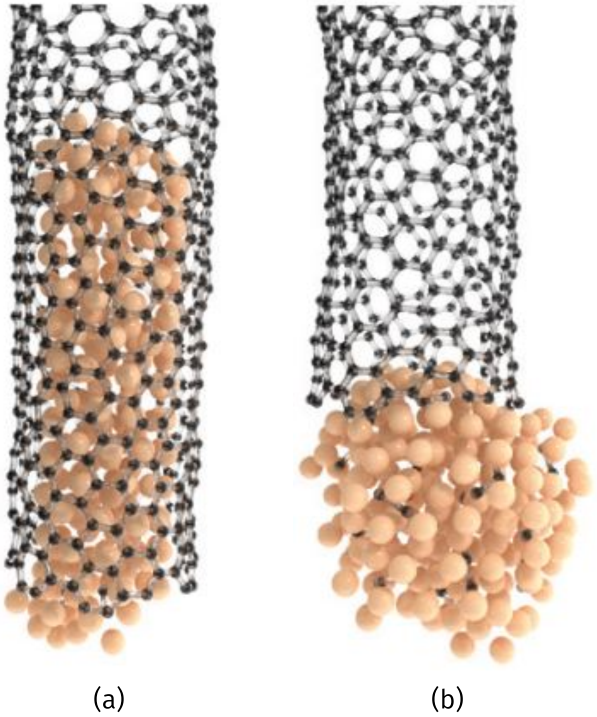

Figure 1.7: Tangential (1.7a) and perpendicular (1.7b) growth modes as described by He et al.[33]

(a) (b)

defined by the diameter and the chiral angle of the nanotube, we need to control these two parameters during the growth process. Controlling the diameter of the CNT can be accomplished by tuning the NP diameter.[34] However, controlling the chiral angle is much more challenging, whereas it also is crucial to achieve chirality-specific growth.[35–38] To obtain narrower chirality distributions, bimetallic NPs such as NiFe, CoMo and CoPt have been used experimentally as catalysts with promising results.[39–41] Bimetallic NPs have the advantage over pure NPs that their properties can be tuned not only by their size, but also by their chemical composition and chemical ordering,[42,43] leaving additional opportunities for tuning. In other words, they can be tuned to fall inside the Goldilocks zone so that they are able to catalyze CNT growth, while maintaining their other interesting properties. Therefore, part of this work will explore the opportunities for bimetallic NPs as chirality-selective growth catalysts. Before doing so, we investigated the stabilities of bimetallic NPs and the influence of carbon interstitials in chapter 3.

In the interaction between catalyst and CNT, there is a variety of factors influencing the chirality that will eventually be formed. However, the driving factor for the chirality formation is still a matter of debate. The thermodynamic stability of the CNT-NP complex has been put forward as a possible driving factor.[37,44,45] Suggestions for possible reasons behind this are a correlation between the NP structure and the CNT chirality,[46,47] the edge energy of a graphene strip with a certain chirality,[48] and a combination of edge energy and curvature effects in the CNT.[49] In particular, the thermodynamic stability of the CNT-NP complex can be investigated using the adhesion energy of a CNT attached to a NP.[18,50,51] Nevertheless, other research suggests that the adhesion energy differences between chiralities are not high enough to promote chirality selective growth.[52] To get a better insight in its influence on CNT growth, we studied adhesion energies of CNTs with various chiralities on monometallic as well as bimetallic NPs in chapter 4.

On the other hand, CNT growth is a non-equilibrium process that is controlled largely by the kinetics of underlying individual processes, especially the process of defect healing. Defect healing becomes much easier while the defect is still in contact with the metal NP. Namely, healing for example a Stone-Wales defect in a pure carbon network has an energy barrier in the order of 5 - 7 eV,[53] whereas healing the same defect in contact with the metal only has a barrier in the order of 1 - 2 eV.[54] Defects growing into the CNT can cause the chirality to change, which is clearly not desirable for chirality selective growth. Therefore, the ability of the catalyst to heal defects on the CNT-NP interface is an important factor influencing the chirality.[53] In chapter 5 we focus on the energies of defects in CNTs adhered to a Ni catalyst, to investigate whether healing the defect will be energetically favoured or not.

## 1.3 Carbyne

### 1.3.1 Structure and properties

Carbyne is a linear chain of carbon atoms. As mentioned in section 1.1, two forms exist: carbyne with alternating single and triple bonds (or polyyne), and carbyne with all double bonds (or cumulene). Its mechanical properties have been reported to even outperform those of graphene and CNTs. Examples include its Young's modulus of 32.71 TPa, its shear modulus of 11.8 TPa, and its specific stiffness in the order of $10^9$ Nm/kg.[55] Moreover, carbyne has a thermal conductivity of 80 kWm$^{-1}$K$^{-1}$,[11] ballistic electron transport,[10] and spin properties.[9] Furthermore, carbyne has a direct band gap that is tunable by changing the length of the carbyne chain.[56] This renders carbyne interesting for a number of applications in electronics. In chapter 6, some of the structure-dependent electronic properties will be discussed. Unfortunately, carbyne has a high chemical reactivity and instability,[57,58] hence synthesis of long carbyne is not straightforward. To stabilize a carbyne chain, it should either be protected by heavy end-capping groups[59,60] or, preferably, by a double walled CNT (DWCNT) wrapped around it.[61] Carbyne synthesis will be discussed in section 1.3.2.

### 1.3.2 Synthesis

Even though carbyne synthesis faces challenges, carbyne growth has been shown to be successful when it occurs inside a multi-walled CNT, more specifically double-walled CNTs (DWCNTs). Typically, the DWCNT must have a suitable inner diameter, furthermore the DWCNT must have received high temperature treatment.[58,61,62] Endohedral carbyne growth is thus being studied as a possibility to obtain these electrically interesting materials.
Endohedral carbyne growth requires the insertion of a precursor into the DWCNT. Precursors that have been employed are ethanol,[63] graphitic nanoflakes,[64] and hydrocarbons.[65,66] In this thesis the focus lies on hydrocarbons.
To aid the carbyne synthesis, a metal catalyst could be embedded in the DWCNT. When the precursor adsorbs on the catalyst, precursor bond breaking and C-C bond formation could be facilitated, owing to the lowering of activation energy barriers of those reactions by the metal. The roles of the catalyst and of the precursor in endohedral carbyne growth are examined in chapter 6.

## 1.4 Research questions and aims of the thesis

To enable CNTs and carbyne to be used on a large scale in electronic applications, we need to unravel their growth mechanisms.
More specifically for CNTs, we need to find a way to control the growth process so that only one chirality is grown. This requires a better understanding of the processes that play a role in CNT growth, in order to find the driving force(s) for chirality formation. In this thesis, we delve deeper into two processes that are deemed important in CNT growth, namely the CNT-catalyst adhesion and defect healing. Moreover, the catalyst plays an important role in CNT growth, and bimetallic catalysts are believed to aid in chirality control. We aim to get a better understanding of the role of these bimetallic catalysts, especially in the case of CNT-catalyst adhesion. Our overall goal is to improve the knowledge of chirality formation in CNT growth, with a view to enable chirality controlled CNT growth in the future.
On the other hand, carbyne is a recent player in nanotechnology and its potential growth processes have not yet been fully explored. As its electronic properties are also defined during the growth process, we want to control this

growth as well. Since the growth mechanism of carbyne is still elusive, we aim to understand the role of catalyst and precursor in controlling carbyne growth.

# 2 Simulation techniques

Computer modelling has received considerable attention in the last decades, as computers have been getting more and more powerful. Computer simulations have become indispensable for studying chemical processes, such as the growth of carbon nanomaterials. Those are extremely complicated processes, in which many factors exert their influence at the same time. These processes can be studied using computer simulations such as molecular dynamics. Although conducting experiments and dynamics simulations is crucial because they can exhibit the full picture of the process, they are limited in the way that they do not enable measuring only one factor in the process, e.g. the adhesion energy. Whereas computer simulations such as density functional theory are not able to give the full picture of such a complicated process, they are particularly useful to separately study one factor at a time. This allows for calculating e.g. the adhesion energy without any other external influences. Both a density functional theory and a molecular dynamics framework are used in this work, and some background on both techniques is given in sections 2.1 and 2.2, respectively. Section 2.3 provides an overview of why and how we implemented those methods in this work.

## 2.1 Density functional theory

Density functional theory (DFT) is an electronic structure calculation method, based on the principles of quantum mechanics. A brief discussion on the quantum mechanics lying at the basis of DFT is given in sections 2.1.1 and 2.1.2. The theoretical foundations of DFT are given in sections 2.1.3 - 2.1.6. The practical implementations for computation then are explained in sections 2.1.7 - 2.1.8.

### 2.1.1 Quantum mechanics

A stationary quantum mechanical system is described by the time-independent Schrödinger equation:

$$H\Psi = E\Psi. \tag{2.1}$$

Here, $H$ is the Hamiltonian operator, the wave function $\Psi$ gives the state of the system, and $E$ is the total energy of the system described by the Schrödinger equation. The energy eigenvalues and the eigenstates are obtained by solving the Schrödinger equation. The Hamiltonian for a coupled electron-nucleus system, in a non-relativistic description, looks like this:

$$\begin{aligned} H = &-\sum_i \frac{\hbar^2}{2m_e}\nabla_i^2 - \sum_I \frac{\hbar^2}{2M_I}\nabla_I^2 - \sum_{i,I}\frac{1}{4\pi\epsilon_0}\frac{Z_I e^2}{|\vec{r}_i - \vec{R}_I|} \\ &+ \frac{1}{2}\sum_{i\neq j}\frac{1}{4\pi\epsilon_0}\frac{e^2}{|\vec{r}_i - \vec{r}_j|} + \frac{1}{2}\sum_{I\neq J}\frac{1}{4\pi\epsilon_0}\frac{Z_I Z_J e^2}{|\vec{R}_I - \vec{R}_J|}, \end{aligned} \tag{2.2}$$

where $\vec{r}_i$ and $\vec{R}_I$ are the coordinates of the N electrons and M nuclei respectively, $M_I$ and $Z_I$ are the masses and atomic number of the nuclei, $m_e$ and $e$ are the electron mass and charge, and $\epsilon_0$ is the permittivity of vacuum. The first two terms describe the kinetic energy of the electrons and nuclei respectively, whereas the last three terms describe potential energies. In particular, the third term describes the attractive electrostatic interaction between electrons and nuclei, and the fourth and fifth term describe the repulsive electrostatic interaction between electrons and between nuclei, respectively. In short, one can write down the Hamiltonian as

$$H = T_e + T_n + V_{ne} + V_{ee} + V_{nn} \tag{2.3}$$

and the Schrödinger equation as

$$[T_e + T_n + V_{ne} + V_{ee} + V_{nn}]\Psi(\vec{x}, \vec{X}) = E\Psi(\vec{x}, \vec{X}) \tag{2.4}$$

with $\vec{x} \equiv (\vec{r}_1, ..., \vec{r}_N, \sigma_1, ..., \sigma_N)$ and $\vec{X} \equiv (\vec{R}_1, ..., \vec{R}_M, \Sigma_1, ..., \Sigma_M)$ the position coordinates and spins of the electrons and nuclei respectively. Since this leads to 4(M+N) coupled degrees of freedom, solving the Schrödinger equation of such a system is almost impossible. In the following sections, approximations made to enable solving the Schrödinger equation will be introduced.[67]

### 2.1.2 Born-Oppenheimer approximation

The Born-Oppenheimer approximation introduces an idea based on the difference in mass between electrons and nuclei.[68] Since the nuclei are much heavier, they move much more slowly than the electrons, and hence the electrons will follow the nuclei's motion instantaneously. The wave function of the system can thus be factorized into a nuclear wave function and an electronic wave function:

$$\Psi(\vec{x}, \vec{X}) = \Psi_e(\vec{x}; \vec{X})\Psi_n(\vec{X}). \tag{2.5}$$

Note that the nuclear wave function $\Psi_n(\vec{X})$ only depends on the nuclear coordinates, whereas the electronic wave function $\Psi_e(\vec{x}; \vec{X})$ depends on both electronic and nuclear coordinates, albeit only parametrically on the latter. We thus get a separation of the Schrödinger equation into the nuclear part

$$[T_n + V_{nn}]\Psi_n(\vec{X}) = E_n\Psi_n(\vec{X}), \tag{2.6}$$

and the electronic part

$$[T_e + V_{ee} + V_{ne}]\Psi_e(\vec{x}; \vec{X}) = E_e\Psi_e(\vec{x}; \vec{X}), \tag{2.7}$$

where electrons move around in field of fixed nuclei. As the electronic wave function only depends on the nuclear coordinates through the electrostatic nuclei-electron interactions, the electrons move in an external potential generated by the nuclei. Once the positions of the nuclei are chosen, the electronic Schrödinger equation needs to be solved for this nuclear configuration. Hence this is called an electronic structure calculation. Therefore we will note $\Psi_e(\vec{x}; \vec{X}) \equiv \Psi(\vec{x})$ and $V_{ne} \equiv V_{ext}$ as the external potential generated by the nuclei.[67]

### 2.1.3 Hohenberg-Kohn theorems

The Hohenberg-Kohn theorems have been extremely important for DFT.[69] The first Hohenberg-Kohn theorem states that "the external potential $V_{ext}(\vec{r})$ is determined uniquely, except for an additive constant, by the ground state electron density $\rho_0(\vec{r})$". Now we know already that when the external potential is known, the Schrödinger equation can be solved, leading to the wave functions and eigenvalues. Moreover, the electron density is actually defined from the wave function:

$$\rho(\vec{r}) = N \int |\Psi(\vec{r}, \vec{r}_2, ..., \vec{r}_N)|^2 d\vec{r}_2 ... d\vec{r}_N. \tag{2.8}$$

Note that we will omit spin-dependence for the rest of section 2.1. Combining this definition with the first Hohenberg-Kohn theorem, we get a one-on-one correspondence between wave function and electron density. Owing to this correspondence, the energy is a unique functional of the density. The high computational cost of solving the Schrödinger equation for N interacting particles can thus be reduced by using the electron density as the only fundamental variable.

However, the exact form of this functional is still elusive. A clue about a property of this functional is given by the second Hohenberg-Kohn theorem: "for a density $\rho'$ such that $\rho' \geq 0$ and $\int \rho'(\vec{r}) d\vec{r} = N$, holds $E_0 = E[\rho_0] \leq E[\rho']$". This implies that when we want to find the ground state energy $E_0$, we need to solve

$$\delta E[\rho] = 0. \tag{2.9}$$

Varying the electron density until the ground state energy is minimized is called the variational principle. It will lead to the relevant electron density, provided that we know the form of the functional. However, how to find the energy functional is not elucidated by the Hohenberg-Kohn theorems.[67]

### 2.1.4 Kohn-Sham equations

To minimize equation 2.9, we need the method provided by Kohn and Sham.[70] We know from the first Hohenberg-Kohn theorem that the total energy is a unique functional of the electron density. The total energy can be written as

$$E[\rho] = T[\rho] + E_H[\rho] + E_{ext}[\rho] + E'_{XC}[\rho], \tag{2.10}$$

where $T[\rho]$ is the kinetic energy of the interacting electrons, $E_H[\rho]$ is the Hartree term, i.e. the Coulomb repulsive interaction:

$$E_H[\rho] = \frac{1}{2} \int V_H(\vec{r}) \rho(\vec{r}) d\vec{r} = \frac{1}{2} \int \int \frac{1}{4\pi\epsilon_0} \frac{e^2 \rho(\vec{r'}) \rho(\vec{r})}{|\vec{r} - \vec{r'}|} d\vec{r'} d\vec{r},$$

$E_{ext}[\rho]$ is the energy due to the external potential:

$$E_{ext}[\rho] = \int V_{ext}(\vec{r}) \rho(\vec{r}) d\vec{r},$$

and $E'_{XC}[\rho]$ contains all other contributions. Due to the second Hohenberg-Kohn theorem with the condition that the total number of electrons is fixed, i.e. $N = \int \rho(\vec{r})d\vec{r}$, we minimize the energy using a Lagrange multiplier $\mu$:

$$\delta \left\{ E[\rho] - \mu \left( \int \rho(\vec{r})d\vec{r} - N \right) \right\} = 0, \tag{2.11}$$

leading to

$$\mu = \frac{\delta T[\rho]}{\delta \rho} + V_H(\vec{r}) + V_{ext}(\vec{r}) + \frac{\delta E'_{XC}[\rho]}{\delta \rho}. \tag{2.12}$$

$T[\rho]$ and $E'_{XC}[\rho]$ are unknown and making reasonable approximations for the kinetic energy of interacting electrons is difficult. Kohn and Sham showed that the system of interacting electrons can be mapped onto a system with non-interacting electrons with the same energy and density, but moving around in an effective external potential $V_S$. This system has an energy

$$E_S[\rho] = T_S[\rho] + \int V_S(\vec{r})\rho(\vec{r})d\vec{r}, \tag{2.13}$$

with $\rho(\vec{r})$ equal to the electron density of the original interacting system. For the non-interacting system, the variation principle leads to

$$\mu = \frac{\delta T_S[\rho]}{\delta \rho} + V_S(\vec{r}). \tag{2.14}$$

We can now extract the effective single-particle potential of the non-interacting system by comparing equations 2.12 and 2.14:

$$\begin{aligned} V_S(\vec{r}) &= \frac{\delta T[\rho]}{\delta \rho} - \frac{\delta T_S[\rho]}{\delta \rho} + V_H(\vec{r}) + V_{ext}(\vec{r}) + \frac{\delta E'_{XC}[\rho]}{\delta \rho} \\ &= V_H(\vec{r}) + V_{ext}(\vec{r}) + V_{XC}(\vec{r}), \end{aligned} \tag{2.15}$$

where

$$V_{XC}(\vec{r}) = \frac{\delta E_{XC}[\rho]}{\delta \rho}$$

is the exchange-correlation (XC) potential of the interacting electron gas with

$$E_{XC}[\rho] = T[\rho] - T_S[\rho] + E'_{XC}[\rho]$$

the XC energy, which also includes the kinetic correlation for the interacting system ignored in $T_S[\rho]$. The total energy thus becomes

$$E[\rho] = T_S[\rho] + E_H[\rho] + E_{ext}[\rho] + E_{XC}[\rho]. \tag{2.16}$$

We can write down the Hamiltonian for the non-interacting system as

$$H = \sum_i \left( -\frac{\hbar^2}{2m_e} \nabla_i^2 + V_{KS} \right) \tag{2.17}$$

with the Kohn-Sham potential $V_{KS} \equiv V_S$. Since the solution of the Schrödinger equation can be expressed as a Slater determinant, one gets the single-particle Kohn-Sham equations:

$$\left( -\frac{\hbar^2}{2m_e} \nabla^2 + V_{KS} \right) \psi_i(\vec{r}) = \epsilon_i \psi_i(\vec{r}) \tag{2.18}$$

where $V_{KS} = V_H + V_{ext} + V_{XC}$ with

$$V_H = \int \frac{1}{4\pi\epsilon_0} \frac{e^2 \rho(\vec{r'})}{|\vec{r} - \vec{r'}|} d\vec{r'},$$

$$V_{ext} = \sum_I \frac{1}{4\pi\epsilon_0} \frac{e^2 Z_I}{|\vec{r} - \vec{R}_I|},$$

$$V_{XC} = \frac{\delta E_{XC}}{\delta \rho},$$

and

$$\rho(\vec{r}) = 2 \sum_{i\ occ} |\psi_i(\vec{r})|^2 \tag{2.19}$$

is the density of the original interacting system. The sum runs over all occupied orbitals and the factor 2 takes into account the spin degeneracy.
The Kohn-Sham equations are thus single-particle equations for a non-interacting system with the same density and energy as the original interacting system. To find the wave functions, one needs to solve the Kohn-Sham equations. Therefore, we need to know the electron density to be able to calculate $V_{KS}$. However, the electron density is only known as a function of the wave functions, and hence the Kohn-Sham equations need to be solved self-consistently. The first three terms of equation 2.16 are easily computable, only the last term, the XC functional of the electron density, includes the difficult many-body terms. The Kohn-Sham approach is in principle exact, but since the XC functional is not known, it needs to be approximated. A number of reasonable approximations exist, a few of which will be explained in section 2.1.5.[67]

### 2.1.5 Exchange-correlation functional

Many expressions for the XC functional exist, but only the relevant ones for this thesis will be discussed. The most simple approximation is based on a hypothetical uniform electron gas, in which electrons move on a positive background charge distribution, so that the total ensemble is electrically neutral. We can now set the exchange-correlation potential at each position to the known exchange-correlation potential from the uniform electron gas at the electron density at that position. The total XC energy then becomes

$$E_{XC}[\rho] = \int \rho(\vec{r})\epsilon_{XC}(\rho)d\vec{r}, \tag{2.20}$$

with $\epsilon_{XC}(\rho)$ the XC energy per electron of the uniform electron gas with density $\rho$. Since we only need to know the local electron density to define the exchange-correlation approximation, it is called the local density approximation (LDA).
Although the LDA has applications, it is usually not accurate enough for applications in computational chemistry. In real systems the electron density varies in space. Therefore, next to information about the local electron density, the local inhomogeneities in the electron density can be taken into account. To do this, the local gradient in electron density is used, and we thus get the generalized gradient approximation (GGA). The XC term is then a functional of both density and its gradient:

$$E_{XC}[\rho] = \int \rho(\vec{r})f(\rho, \nabla\rho)d\vec{r}. \tag{2.21}$$

Note that the XC energy is still local.[67,71] Various forms for $f(\rho, \nabla\rho)$ can be included in the GGA, meaning that there are many varieties in GGA functionals,[71] such as Perdew-Wang (PW91)[72] and Perdew-Burke-Ernzerhof (PBE).[73]

### 2.1.6 Ionic optimization

Up to this point we only looked at solutions of the electronic Schrödinger equation, which is for fixed nuclear positions. To find the lattice constants or atomic positions for a system, we also need to find nuclear coordinates for which the atoms reach equilibrium, i.e. for which the forces are zero:

$$\vec{F}_I = -\frac{\delta E}{\delta \vec{R}_I} = 0 \tag{2.22}$$

with $I = 1, ..., M$ and E the energy of both the electrons and the nuclei:

$$E = E_e + \frac{1}{2}\sum_{I \neq J} \frac{1}{4\pi\epsilon_0} \frac{Z_I Z_J e^2}{|\vec{R}_I - \vec{R}_J|}.$$

The Hellmann-Feynman theorem now states that the derivative of the energy with respect to a parameter $\lambda$ is equal to the expectation value of the derivative of the Hamiltonian with respect to that parameter:[74,75]

$$\frac{\delta E}{\delta \lambda} = \langle \Psi | \frac{\delta H}{\delta \lambda} | \Psi \rangle. \tag{2.23}$$

Applying the Hellman-Feynman theorem, we can calculate the partial derivative in equation 2.22:

$$\begin{aligned} \vec{F}_I &= -\langle \Psi | \frac{\delta H}{\delta \vec{R}_I} | \Psi \rangle \\ &= -\langle \Psi | \frac{\delta T_e}{\delta \vec{R}_I} | \Psi \rangle - \langle \Psi | \frac{\delta V_{ee}}{\delta \vec{R}_I} | \Psi \rangle - \langle \Psi | \frac{\delta V_{ne}}{\delta \vec{R}_I} | \Psi \rangle - \frac{\delta E_n}{\delta \vec{R}_I}. \end{aligned} \tag{2.24}$$

Here, the first two terms do not depend on the nuclear coordinates, so they are equal to zero. Moreover, $V_{ne}$ is the external potential generated by the nuclei in which the electrons move $V_{ext}$. Hence, equation 2.24 becomes

$$\vec{F}_I = -\int \rho(\vec{r}) \frac{\delta V_{ext}}{\delta \vec{R}_I} d\vec{r} - \frac{\delta E_n}{\delta \vec{R}_I}. \tag{2.25}$$

The forces on the atoms in the system can now be calculated using the atom positions $\vec{R}_I$ and the electron density $\rho(\vec{r})$. The forces are used in combination with a minimization algorithm to find the equilibrium positions of the atoms in the crystal.[76]

### 2.1.7 Bloch theorem

In principle, all electrons in a system should be considered when solving the Kohn-Sham equations. However, using the periodicity of the crystal, this can be simplified. Free electrons in a crystal feel an effective single-particle potential which is periodic:

$$V_{eff}(\vec{r}) = V_{eff}(\vec{r} + \vec{T}) \tag{2.26}$$

with $\vec{T}$ a translation vector. The Bloch theorem now states that the solutions of the Kohn-Sham equations 2.18 for a periodic potential can be written as:[77]

$$\psi_{n,\vec{k}}(\vec{r}) = u_{n,\vec{k}}(\vec{r}) e^{i\vec{k}\cdot\vec{r}}. \tag{2.27}$$

These Bloch wave functions are the product of plane waves $e^{i\vec{k}\cdot\vec{r}}$, which are the eigenstates of a free electron in vacuum, and a periodic function $u_{n,\vec{k}}(\vec{r})$, which has the same periodicity as the crystal lattice:

$$u_{n,\vec{k}}(\vec{r}) = u_{n,\vec{k}}(\vec{r} + \vec{T}). \tag{2.28}$$

Note that $\psi_i$ is replaced here with $\psi_{n,\vec{k}}$, where $\vec{k}$ is a wave vector within the first Brillouin zone and n is the band index. The band index labels the multiple solutions to the Kohn-Sham equations for each value of $\vec{k}$.

Since $u_{n,\vec{k}}(\vec{r})$ is periodic, it can be expanded in a Fourier series over reciprocal lattice vector $\vec{G}$:

$$u_{n,\vec{k}}(\vec{r}) = \sum_{\vec{G}} C_{\vec{k}+\vec{G}} e^{i\vec{G}\cdot\vec{r}}, \tag{2.29}$$

leading to the Bloch wave function

$$\psi_{n,\vec{k}}(\vec{r}) = \sum_{\vec{G}} C_{\vec{k}+\vec{G}} e^{i(\vec{k}+\vec{G})\cdot\vec{r}}. \tag{2.30}$$

The expression for the electron density for an infinitely extended crystal then becomes

$$\rho(\vec{r}) = 2 \int_{1^{st}\ BZ} \sum_{n\ occ} |\psi_{n,\vec{k}}(\vec{r})|^2 d\vec{k} \tag{2.31}$$

where the factor 2 is for spin degeneracy, $\vec{k}$ is indeed a wave vector within the first Brillouin zone, and n runs over all occupied bands. Closely located $\vec{k}$-points yield nearly equal eigenvalues, so practical calculations replace the integral by a summation over a finite set of $\vec{k}$-points, leading to an efficient sampling of the first Brillouin zone and a decrease of computational cost.[67]

### 2.1.8 Basis set

In practical calculations, the Kohn-Sham orbitals are expanded in a set of predefined basis functions. They can be localized or delocalized. The Bloch theorems makes delocalized plane waves a natural choice for periodic systems. In principle, an infinite number of plane waves is needed for the expansion. However, coefficients $C_{\vec{k}+\vec{G}}$ for plane waves with small kinetic energies $\frac{\hbar^2}{2m_e}|\vec{k}+\vec{G}|^2$ are more relevant than those with large kinetic energies. Therefore, the plane wave basis set can be truncated so that only plane waves with kinetic energies smaller than a certain cutoff energy are included:

$$\frac{\hbar^2}{2m_e}|\vec{k}+\vec{G}|^2 \leq E_{cut}. \tag{2.32}$$

A higher cutoff energy leads to a more accurate calculation, but also to a higher computational cost. Therefore, a reasonable value for $E_{cut}$ must be found.[67]

Within the plane wave basis set, simplifications can be made to deal with the large number of electrons for which the Kohn-Sham equations need to be solved. An observation that is important here, is that the core electrons are not important for the chemical bonding between atoms and the physical properties of a material, only the valence electrons are. Moreover, close to the nucleus, the atomic wave functions will oscillate strongly, but it will be much smoother in the interatomic region. Close to the nucleus, the number of plane waves needed to represent a wave function would be too high for practical calculations on realistic systems.[67]

In the pseudopotential approach, one makes use of the frozen core approximation, which fixes the properties of the core electrons. The strong ionic potential is then replaced by a weaker pseudopotential to act on a set of pseudo wave functions rather than on the true wave functions. Beyond a certain cutoff radius, the pseudopotential and pseudo wave functions will be equal to the true potential and true wave functions. This approach reduces the number of plane waves needed to describe the wave function in the core region.

All electron methods on the other hand do not artificially separate the core and valence electrons, and all electrons are explicitly used. A so-called muffin-tin sphere is constructed around each atom, which represents the atomic region. The interstitial regions between muffin-tin spheres represent the interatomic bonding regions. Within the atomic regions, atomic-like basis functions are used, whereas within the interstitial regions, the plane wave expansion is used. At the boundary, both wave functions must match each other.

A third and very common approach is the projector augmented wave (PAW) method.[78,79] It is not an all electron method, because again the frozen core approximation is used. The true wave functions are decomposed in terms of smooth pseudo wave functions, which can easily be expanded in plane waves. However, since the true and pseudo wave functions are related by a linear transformation, the true wave functions can always be reconstructed, in contrast with the pseudopotential approach. Within the PAW spheres surrounding the atoms, the pseudo wave functions are a bad approximation to the true wave functions, but in the interatomic regions between the PAW spheres, they are identical to the true wave functions.[80]

## 2.2 Molecular dynamics

In contrast to DFT, molecular dynamics (MD) is an atomistic scale simulation method and builds on classical mechanics, rather than on quantum mechanics. The classical mechanics framework used in MD is discussed in 2.2.1. The advantage of MD is that dynamic phenomena can be simulated, contrary to DFT, that does not allow for dynamic calculations. Two types of MD exist: classical MD and ab initio MD. Classical MD employs empirical force fields to calculate the forces, whereas ab initio MD obtains the forces from ab initio calculations, such as DFT. Both were used during the course of this thesis, and will be discussed in the following sections: classical MD in section 2.2.2, and ab initio MD in section 2.2.3. The manner in which to obtain physical properties from MD simulations is explained in section 2.2.4. Section 2.2.5 gives an overview of methods to improve phase space sampling.

### 2.2.1 Classical mechanics

Considering N atoms of which we want to study the dynamics, we can describe the state of the N-atom system using the total kinetic energy and the total potential energy, which are respectively defined as

$$K = \frac{1}{2}\sum_{i=1}^{N} m_i \vec{v}_i^2, \tag{2.33}$$

where $m_i$ and $\vec{v}_i$ are the mass and the velocity of the $i^{th}$ atom, and

$$U = U(\vec{r}_1, ..., \vec{r}_N), \tag{2.34}$$

where $\vec{r}_1$ until $\vec{r}_N$ are the positions of the N atoms. The force on the $i^{th}$ atom can then be defined as the derivative of the total potential energy:

$$\vec{F}_i = -\vec{\nabla}_i U(\vec{r}_1, ..., \vec{r}_N). \tag{2.35}$$

Using Newton's laws, which are applicable in the framework of classical mechanics, we can also write down the force as

$$\vec{F}_i = m_i \vec{a}_i = m_i \frac{d\vec{v}_i}{dt}, \tag{2.36}$$

where $\vec{a}_i$ is the acceleration of the $i^{th}$ atom.
These equations define the deterministic trajectories of the atoms through time and space. These trajectories are exactly what MD simulations calculate.[71]
MD is an iterative method, and the forces are calculated using equation 2.35. The interatomic potential we get either from force fields (in classical MD) or from DFT (in ab initio MD), using the positions and velocities of the previous time step. More about how to obtain the forces will be explained in sections 2.2.2 and 2.2.3. Once we have the forces, we can solve the equations of motion (equation 2.36) numerically over time step Δt. Subsequently, we can obtain the physical properties we are interested in. How to do this exactly is the subject of section 2.2.4.

### 2.2.2 Calculating forces in classical MD

In classical MD, the interatomic potentials are obtained using a force field. These force fields are normally material-specific, and represent all possible interactions between the material's elements. Two large groups of force fields exist: non-reactive force fields and reactive force fields. The first groups only takes into account the energy of the stable compounds, whereas the second group takes into account the energy of all steps in the reaction. Hence, using reactive force fields, we can analyse the reactivity of the system. On the other hand, this ability increases the calculation time. Using an accurate force field is a prerequisite for an accurate MD simulation. For the CNT-NP systems with bimetallic catalysts studied in this thesis, no (accurate) force field was available. Therefore, for all calculations conducted with classical MD in this thesis we use monometallic catalysts.

### 2.2.3 Calculating forces in ab initio MD

With ab initio MD, higher accuracy can be reached than with classical MD. In ab initio MD, DFT is used to calculate the potential energy $U$. This means the ground state energy of the system of interest is calculated using DFT, subsequently the positions of the atoms are updated using one MD time step, then the ground state energy is calculated again, until this iterative approach reaches the preset amount of MD time steps. Two main ab initio MD methods can be discerned, Car-Parrinello MD (CPMD) and Born-Oppenheimer MD (BOMD). In the Car-Parrinello approach, equations of motion for both nuclei and electronic degrees of freedom are simultaneously followed by MD. Consequently, the total energy calculated at each time step is not at the true Born-Oppenheimer potential energy surface for the nuclear coordinates.[71] In the Born-Oppenheimer approach, it is assumed that the Born-Oppenheimer approximation is valid, as well as the adiabatic approximation. In this last approximation, the electronic wave functions adapt quasi-instantaneously to a change in nuclear configuration. It is also assumed that the electronic wave function is in the ground state.[81] Electronic information from the previous MD run is used as an initial approximation for the ground state of the updated nuclei's positions in order to enable a more efficient calculation of the energy and the forces for a new time step. Contrary to CPMD, here nuclei do move on the ground state Born-Oppenheimer potential energy surface, hence the name of the method.[71]

### 2.2.4 Obtaining physical properties from MD

To describe how a physical property A is computed in MD, we first need to take a closer look at statistical mechanics. In statistical mechanics, one works with positions and momenta rather than velocities:

$$\vec{p}^N(t) = \vec{p}_1(t), ..., \vec{p}^N(t) \tag{2.37}$$

where $\vec{p}_1(t) = m\vec{v}_1(t)$. Now, the vector $\vec{x} = (q_1, ..., q_{3N}, p_1, ..., p_{3N})$ is interpreted as the microstate of a mechanical system. This $\vec{x}$ is a point in the 6N-dimensional phase space and corresponds to one microscopic state of motion of the whole system.[82] At any instant in time, the complete phase space vector of a system can be specified as a microsystem. The collection of microsystems that match the same macroscopical state is then called an ensemble.

Looking at one member in the ensemble, you can define the probability that its phase space vector will be in a small volume $d\vec{x}$ around point $\vec{x}$ in the phase space at time $t$ as $\rho(\vec{x}, t)d\vec{x}$. This $\rho(\vec{x}, t)$ is called the phase space probability density. According to Liouville's theorem, $\rho$ should be stationary:

$$\frac{d}{dt}\rho(q^N, p^N, t) = 0. \tag{2.38}$$

and hence the total number of systems in the ensemble should be constant.[83]

Furthermore, knowing that usually we are only interested in the global system properties rather than the individual trajectories, a physical property A can be computed as

$$\langle A \rangle_{ensemble} = \int\int dp^N dr^N A(p^N, r^N)\rho(p^N, r^N) \tag{2.39}$$

However, in MD, we don't calculate $\langle A \rangle_{ensemble}$, but we follow the time evolution of this 6N-dimensional vector $\vec{x}$, and we thus calculate

$$\langle A \rangle_{time} = \lim_{\tau \to \infty} \frac{1}{\tau} \int_{t=0}^{\tau} A(p^N(t), r^N(t))dt \approx \frac{1}{M} \sum_{t=1}^{M} A(p^N, r^N). \tag{2.40}$$

Now, $\langle A \rangle_{time} = \langle A \rangle_{ensemble}$ only if the system is in thermodynamic equilibrium and the ergodicity principle applies. The ergodicity principle states that the system will go through all points in phase space if the duration of simulation is long enough. Therefore, under the right conditions, we can calculate physical properties as averages over time.

Various ensembles can be used in MD, but the two best-known ensembles are the microcanonical ensemble (NVE) and the canonical ensemble (NVT). The microcanonical ensemble is the natural ensemble for an MD simulation, because

MD simulations preserve energy. The microcanonical ensemble represents an isolated system, where the number of particles (N), the volume (V) and the total energy ($E = K + U$) are constant. The energy cannot be exactly constant, due to the finite precision of the atomic forces evaluation, and the finite time step. For the energy error to be controlled, the time step will have a maximum magnitude.

In spite of the natural ensemble being NVE, an NVT ensemble can also be used in MD simulations. This canonical ensemble represents a closed system, that is however not heat-isolated. The number of particles (N), the volume (V) and the temperature (T) are constant. Energy can now be exchanged with the environment. To use the NVT ensemble, a modification is needed in order to force the temperature to remain constant during the simulation. Two types of modification exist. The first type is velocity scaling, in which the velocities are modified each time step. Either direct velocity scaling can be used, where the velocity is scaled by $\sqrt{^{T_{set}}/_{T_{actual}}}$,[81] or Berendsen scaling, where the direct scaling factor is dampened by a time constant.[84] The damping in Berendsen scaling was introduced to decrease the disturbance of the system. None of the velocity scaling methods are truly canonical, because the dynamics of the system are altered. The second type of modification is to couple the system to a heat bath. The heat bath will correspond to an environment with which energy is gradually exchanged. The rate of this exchange is called a thermostat. These thermostat methods, however widely used, again do not reproduce the true canonical ensemble.[81] On the other hand, the Andersen thermostat, that assigns particles a new velocity taken from a Maxwell-Boltzmann distribution at $T_{set}$, does reproduce the true canonical ensemble, but not the correct dynamics.[85]

To get a completely true canonical ensemble, the Nosé-Hoover thermostat can be used. Here, the heat bath is considered an integral part of the system, and fictive dynamic variables are assigned. These variables have their own kinetic and potential energy and control the temperature.[86,87]

Similar to the thermostat methods, the NpT ensemble can be used through a barostat and a pressure bath. Not the velocities of the particles are scaled, but the volume of the system. Again, to produce a completely correct ensemble, a Nosé-Hoover approach must be used.[81]

### 2.2.5 Phase space sampling

In section 2.2.4, the ergodicity principle was mentioned. For ergodicity to be a valid assumption, we need to obtain sufficient sampling of the phase space. However, this sampling is very inaccurate in ab initio MD. Ab initio MD is much more computationally expensive, leading to much shorter possible time scales. Evidently, this in turn causes the inaccurate sampling.

Methods to improve sampling of the system in phase space can be divided into two categories: enhanced sampling and accelerated MD. During a simulation, the system can remain trapped in a metastable state for a long time, without any transition occuring. This will lead to an incorrent sampling of the phase space, since other relevant metastable states are never reached. Obtaining a more balanced sampling of relevant states is the objective of enhanced sampling techniques. Accelerated MD on the other hand will accelerate the global system evolution, leading to the correct transitions sequence. It is important here that while accelerating the escape rate from metastable states, the correct probability of all escape pathways is reproduced.[88]

Many methods exist within enhanced sampling, of which we will discuss two. One is replica exchange. Multiple statistically independent replicas of the same system state at different temperatures are independently simulated in parallel. It is easier for the high-temperature replicas to escape metastable states and thus to provide better sampling. The lowest temperature replica on the other hand is at the desired temperature. During the simulation, system coordinates are swapped between replicas, allowing the lowest-temperature replica to benefit from the enhanced sampling of the higher-temperature replicas.[88–90]

The other method is metadynamics, in which a history dependent bias potential is generated during the simulation. The simulation will continue on the biased potential. When the system ends up in a metastable state, the basin will be filled up gradually until the system escapes the state. This continues until all metastable states have been visited.[88,91]

Within accelerated MD, three main methods exist: temperature-accelerated dynamics (TAD), hyperdynamics, and parallel replica dynamics (PRD). We briefly discuss each of these three methods.

In TAD, the temperature is increased to facilitate the crossing of high barriers. However, increasing the temperature will lead to a different system, hence the following approach is needed to get a correct prediction of the system evolution. When an event is detected at the elevated temperature, the associated barrier is computed and stored together with the final configuration and escape time. The system is then returned to its initial stated to resume the simulation. When a sufficient number of escape pathways has been simulated, all possible escape times are extrapolated to the lower target temperature. The state with the lowest escape time will be selected as the product state, from which the simulation at higher temperature can be continued.[88,92]

In the hyperdynamics method, the true potential energy surface is modified by adding a bias potential. This bias potential lowers high barriers, so that events allowing escape from the metastable state are accelerated.[88,93]

PRD is the most accurate accelerated MD method. PRD uses multiple statistically independent replicas of the same system state. Each of these replicas is simulated on a different processor until an event occurs at any one of the replicas. The simulation clock is advanced with the total waiting time on all replicas. The new state initiates a new cycle in all other replicas.[88,94]

## 2.3 Implementation of techniques to study phenomena in carbon nanomaterials growth

### 2.3.1 Nanoparticle stabilities and CNT-metal adhesion energies

As mentioned in chapter 1, we study bimetallic NPs because of their promise as catalysts for CNT growth in chapter 3. Firstly, we investigated the stabilities of various bimetallic NPs, in function of their composition and atom distribution. This will tell us which nanoparticles will be more suitable for CNT growth. We also consider C interstitials in the NPs, since they play an important role during CNT growth, according to the VLS model. The influence of C interstitials on NP stabilities is studied. NP stabilities are all calculated using DFT calculations. In addition to DFT calculations, BOMD simulations are used to investigate C interstitials at finite temperature. BOMD was used instead of classical MD, as no accurate force field is available for Ni, Fe and C combinations.

Subsequently, the results of the NP calculations above are used in chapter 4. There we calculate adhesion energies of various CNTs on mono- and bimetallic NPs to verify if the adhesion energy can be tuned by the NP alloy composition. Furthermore, we discuss whether the adhesion energy is the driving force for chirality formation during CNT growth. DFT calculations were again employed, here to calculate the adhesion energies.

The software package we used for DFT and BOMD calculations is the Vienna Ab initio Simulation Package (VASP).[95–98]

The electronic structure optimization can be executed using various algorithms. One of the possibilities is the blocked Davidson algorithm, which is always stable. On the other hand there is the Residual Minimization Method Direct Inversion in the Iterative Subspace (RMM-DIIS), which is much faster, but also less reliable than the blocked Davidson algorithm. Therefore a combination of both can be used where the first couple of iterative steps are executed with blocked Davidson, and all the following steps with RMM-DIIS.[99] For most calculations, this combination scheme was used, except for the adhesion systems, where we employed the blocked Davidson algorithm, and for the BOMD calculations, where we employed the RMM-DIIS algorithm. Convergence is reached when the magnitude of the energy difference between iterates is smaller than a predefined value.[71] The tolerance for this is $1 \times 10^{-4}$ eV for most calculations, except for the adhesion systems, where it is $1 \times 10^{-6}$ eV, and for the BOMD calculations, where it is $1 \times 10^{-5}$ eV.

We use a GGA functional called revised PBE (RPBE), which is an improvement of PBE for the study of adhesion systems.[100] This is obviously important for our

calculations of CNT-NP adhesion energies.
For the ionic optimization as described in section 2.1.6, we used the conjugate-gradient method, where the atoms are moved along the direction of the steepest descent. Convergence is reached when the magnitude of the forces on all atoms are smaller than a predefined value, in our case 0.01 eV/Å.
VASP works with periodic systems, however, our model systems are not periodic. We put them in a box (i.e. supercell) that is repeated periodically. This has consequences for the supercells we use and the number of $\vec{k}$-points we define. The supercell describes the cell volume and the atom positions. Since we are modelling non-periodic systems in a periodic framework, we need to choose our supercell large enough so as to not get interference between systems in two neighbouring supercells. And yet, the size of the supercell should be kept small enough in the light of computational efficiency. Our supercells were (20 x 20 x 20) Å for the optimization of the NPs and of the CNTs, and (20 x 23 x 30) Å for the adhesion systems. As discussed in section 2.1.7, we need to define the number of $\vec{k}$-points over which we want to sum. However, since the model systems we use are not periodic, we work with one k-point. This to prevent the introduction of artificial dispersion, which is a known problem when using more than one k-point with non-periodic systems. Therefore, all our calculations are executed using a $\Gamma$-centered (1 x 1 x 1) k-point mesh. Calculating integrals in reciprocal space can be complicated in the sense that functions are discontinuous for a lot of materials. This means that the boundaries of this function need to be smoothed out to be able to calculate the integral. This is done by smearing out the discontinuity.[71] We used Methfessel-Paxton (MP) smearing of the first order,[101] with a smearing width of 0.2. MP smearing is used here owing to its superior performance in calculations with metals.[99]
VASP is based on plane wave basis sets as described in section 2.1.8, where we also discussed the cut-off energy that needs to be defined. We used a cutoff energy of 400 eV. We used the projector augmented wave approximation.[78,79]
For Ni and Fe, the 4s and 3d electrons are treated as valence electrons, for Ga the 4s and 4p, but also the 3d electrons, for C the 2s and 2p electrons, and for H the 1s electron.
For the BOMD simulations, there are a number of specific parameters that we do not need for DFT calculations. We will discuss those here. VASP employs a Verlet algorithm to integrate Newton's equations of motion.[99] We set the temperature to 700 K, and used 2000 time steps of 1 fs. The ensemble was canonical with a Nosé-Hoover thermostat.[86,87]

### 2.3.2 Defect healing in CNTs

In chapter 1 it was mentioned that not only thermodynamics govern CNT growth, but also kinetics. An important kinetic process active during CNT growth is defect healing. When we want to control the chirality, it should remain the same during CNT growth. However, when defects grow into the CNT, they will give rise to a change in chirality, which is troublesome for chirality selective growth. Therefore we look into defect stabilities and defect healing in chapter 5. As the process of defect healing is intrinsically kinetic, and DFT does not allow for the study of kinetic processes, defect healing was studied using classical MD. Here we study monomatallic (Ni) catalysts, and for Ni-C(-H) systems, a good force field is available. Therefore we used classical MD instead of ab initio MD, as sampling of the phase space will be more accurate. We calculated energy differences of model systems with defective CNTs and perfect CNTs, and investigated whether defect healing would occur during the MD simulation.

The software package used here is ReaxFF, in which reactive force fields are used.[102] For defect healing, we use the Mueller reactive force field. ReaxFF uses the velocity-Verlet algorithm to integrate the equations of motion. We employ the NpT ensemble with Nosé-Hoover chain thermostat.[86,87] The NpT ensemble keeps the number of particles (N), the pressure (p) and the temperature (T) constant. This is a relevant ensemble for chemical reactions. We apply a maximum atomic displacement of 0.01 Å in each time step. A time step of 0.25 fs is used, and we run the simulation for 10 ns. The temperature is set to 1000 K.

### 2.3.3 Encapsulated carbyne growth

Besides CNT growth, we also studied carbyne growth. More specifically we study the growth of carbyne encapsulated in a DWCNT. Carbyne shows promise for electronic applications, but due to the challenges that the growth process faces, the growth of this material still requires a lot of research. In chapter 6 we focus on the role of the catalyst and of the precursor during the growth. MD simulations and DFT calculations were used to study nucleation and growth of carbon chains in DWCNT. We used Ni as a catalyst and (hydro)carbon species as precursors. Firstly, Ni-assisted nucleation and growth were investigated using classical MD, whereas then both classical MD and DFT were employed to compare energy differences of various chain structures. Lastly, density of states and band gaps for some of the chain structures were calculated using DFT. Again, classical MD was used for the same reasons as mentioned for the process of defect healing.

As well as for defect healing, ReaxFF is also used for the classical MD simulations in this chapter. The ReaxFF potential is used with parameters by Zou et al.[103] Again, the velocity-Verlet algorithm is used to integrate the equations of motion. Periodicity is applied along the z-axis, so that we have an infinitely long DWCNT. The MD simulations were executed in two steps. First, an equilibration of the system at the desired temperature is done in the NpT ensemble with the Berendsen thermostat.[84] Second, the actual simulation is done in the canonical ensemble with the Bussi thermostat.[104] A time step of 0.25 fs is used, the total number of time steps depends on the type of precursor. Simulations were executed at various temperatures between 500 K and 1700 K.

For the DFT calculations, again VASP was used. Input parameters were largely the same as discussed in section 2.3.1. Therefore we will only discuss the parameters that are different for this work. Here we use (20 x 20 x 20) Å for all calculations. Although we still have a metal catalyst, the size of the NP is so small that it does not show metallic behaviour any more. Consequently, we changed the smearing method to Gaussian smearing,[105, 106] with a smearing width of 0.1. The electronic optimization was executed through the combined algorithm of blocked Davidson and RMM-DIIS, and its break condition was set to $1 \times 10^{-4}$ eV.

# 3 Stabilities of bimetallic nanoparticles for chirality-selective carbon nanotube growth and the effect of carbon interstitials

Bimetallic nanoparticles play a crucial role in various applications. A better understanding of their properties would facilitate these applications and possibly even enable chirality-specific growth of carbon nanotubes (CNTs). We here examine the stabilities of NiFe, NiGa and FeGa nanoparticles and the effect of carbon dissolved in NiFe nanoparticles through density functional theory (DFT) calculations and Born-Oppenheimer molecular dynamics (BOMD) simulations. We establish that nanoparticles with more Fe in the core and more Ga on the surface are more stable, and compare these results with well-known properties such as surface energy and atom size. Furthermore, we find that the nanoparticles become more stable with increasing carbon content, both at 0 K and at 700 K. These results provide a basis for further research into the chirality-specific growth of CNTs.

*Publication:* Charlotte Vets and Erik C. Neyts. Stabilities of bimetallic nanoparticles for chirality-selective carbon nanotube growth and the effect of carbon interstitials. *J. Phys. Chem. C*, 121(28):15430-15436, 2017. `https://doi.org/10.1021/acs.jpcc.7b02880`

## 3.1 Introduction

Bimetallic nanoparticles have for a long time been intensively studied for their exceptional behavior.[42] While the properties of pure clusters can only be tuned by their size, the properties of bimetallic nanoparticles can additionally be tuned by chemical composition and chemical ordering.[42,43] Numerous computational studies exist on bimetallic nanoparticles, using different types of simulation methods. A genetic algorithm approach was used by Rapallo et al.[107] and by Rossi et al.[108] to study various bimetallic nanoalloys. Kilimis et al. used density functional theory (DFT) to study Ag-Pd nanoparticles.[109] In addition, conducting DFT computations, Song et al.[110] and Ge et al.[111] investigated the interaction of CO with Pt-Au nanoparticles. The adsorption of O, OH and $H_2O$ on bimetallic nanoparticles has also been studied through DFT calculations by Balbuena et al.[112] Another option is to combine the genetic algorithm and DFT for nanoparticle optimization.[43] Molecular dynamics simulations are regularly performed to analyze the melting behavior of nanoparticles, e.g. that of Au-Ag by Qi et al.[113] and of Cu-Ni by Huang et al., who combined molecular dynamics with Monte Carlo simulations.[114]

Owing to their interesting properties, bimetallic nanoparticles are useful in a plethora of applications, including magnetic sensors,[115] memory devices,[115,116] metal inks,[117] fuel cells[118–120] and catalysis.[118,121–123]

Adding elements to a nanoparticle can change its properties significantly, rendering it even more interesting for certain applications.[124] One particularly interesting example of this is the dissolution of carbon atoms in a nanoparticle, influencing carbon nanotube (CNT) growth.[124,125]

CNTs have attractive properties for numerous applications. For example, they have been used as reinforcements in composite materials because of their spectacular tensile strength (up to 100 GPa),[126] as tips for atomic force microscopy because of their high stiffness, with an elastic modulus up to 1 TPa[127] and in membranes for water filtration.[128,129] However, their application in electronic and optoelectronic devices e.g. as channel material in field-effect transistors,[4,5] or as heat conductors in various devices such as integrated circuits and batteries,[7] may be even more interesting. For CNTs to reach their full potential and be of use in such systems, it is therefore of major importance that their electronic properties can be controlled.

The electronic properties of CNTs are governed by their chirality (n,m), which is in turn determined by the diameter and roll direction of the graphene sheet.[18] Hence it is paramount to achieve chirality-selective growth. This is dependent on the catalyst[130] and unfortunately still very challenging. Narrow chirality distributions, however, have been obtained experimentally with bimetallic catalysts, like NiFe,[39] CoMo[40] and CoPt.[41]

A promising method for chirality-selective growth is catalytic chemical vapor deposition (CCVD). During the CCVD process, a hydrocarbon gas is decomposed on the surface of a catalytic nanoparticle. Carbon atoms subsequently dissolve in the nanoparticle until eventually a carbon network precipitates on the nanoparticle surface due to excess carbon in the nanoparticle. This process is called the vapor-liquid-solid (VLS) model. Another possibility is that the nanoparticle remains solid and that carbon diffuses over the nanoparticle surface before a carbon network is formed, which is the vapor-solid-solid (VSS) growth model.[28,29]

In this work we employ DFT calculations to compute the stabilities of various bimetallic nanoparticles,[110] to investigate which nanoparticles are more likely to be formed in terms of composition and atom distribution. Carbon interstitials are included in the nanoparticles in accordance with the VLS model. We investigate the influence of the carbon interstitials on the nanoparticles' stabilities, as dissolved carbon is crucial for CNT growth,[125] and nanoparticles containing carbon interstitials are precursors to CNT growth. To the best of our knowledge, although nanoparticles containing carbon have been investigated computationally before,[125,131–135] carbon interstitials have so far not been considered in DFT calculations of bimetallic nanoparticles. Control of the atom distribution in bimetallic nanoparticles may be useful for low temperature applications, such as the aforementioned low temperature fuel cells[119,120] and plasma catalysis of CNTs.[28]

## 3.2 Computational Details

The nanoparticles are modelled as 55-atom cuboctahedra, which have a diameter of about 0.8 nm, a diameter also commonly found for CNTs.[136,137] Three different nanoalloys were chosen: NiFe, NiGa and FeGa. Ni and Fe were selected since they are well-known catalysts for CNT growth and a narrow chirality distribution has been obtained with a NiFe catalyst by Chiang et al.[39] Ga was selected as a novel material with potential for CNT growth, as shown by Rao et al.[138] Moreover, $Ga_2O_3$ has exhibited the ability to catalyze dry reforming of methane,[139] a process with similarities to CNT growth.[140,141] Bulk phase diagrams exist for the three nanoalloys,[142–144] however the phase diagrams at the nanoscale will exhibit different features. An example of this was established for Ni-C by Magnin et al.[125] Therefore, all nanoparticles were modelled in the same structure, the aforementioned cuboctahedra. They contain both (111) and (100) planes, which renders them interesting for further studies. Each of the three alloys (NiFe, NiGa, FeGa) is modelled in three compositions: 25/75, 50/50 and 75/25 in at%. Five atom distributions were selected for each composition which are described in at% of the nanoparticle core being Ni (in the case of NiFe and NiGa) or Fe (in the case of FeGa). These five distributions were selected to be 0, 25, 50, 75 and 100 at%. The notation that will be used is e.g. Ni25F75_c25Ni for a 25/75 NiFe nanoparticle with 25% of the core being Ni. Visualizations of some nanoparticles are presented in appendix A. All nanoparticles were subjected to a geometrical optimization as described below.

When the VLS model is applicable, carbon dissolves in the nanoparticles. Hence, the study of interstitial carbons in these nanoparticles is very important as well.[125] We therefore also study the influence of carbon interstitials on the NiFe stabilities, through both DFT calculations and Born-Oppenheimer molecular dynamics (BOMD) simulations. Carbon atoms at the nanoparticle surface according to the VSS model are not considered.

The stability of each of the nanoparticles is computed using two different quantities. The first quantity is the cohesive energy:[110]

$$E_{coh} = -\frac{E_{A_mB_n} - mE_A - nE_B}{m+n} \tag{3.1}$$

where $m$ and $n$ are the number of A and B atoms respectively, $E_A$ and $E_B$ are the total energies of single atoms A and B respectively, and $E_{A_mB_n}$ is the total energy of the AB nanoparticle. A higher cohesive energy indicates a higher structural stability of the cluster with respect to its constituent atoms.[110]

The second quantity is the formation enthalpy, where, in contrast to the cohesive energy, lower formation enthalpies indicate higher thermodynamic stabilities. The formation enthalpy for bimetallic nanoparticles is computed with respect to pure nanoparticles:[110]

$$\Delta H_{f,NP} = \frac{E_{A_mB_n} - \frac{m}{m+n}E_{A_{m+n}} - \frac{n}{m+n}E_{B_{m+n}}}{m+n} \tag{3.2}$$

where $E_{A_{m+n}}$ and $E_{B_{m+n}}$ are the total energies of pure A and B nanoparticles with the same number of atoms as the alloyed nanoparticles.

Carbon atoms were included as interstitials in 4 concentrations in the NiFe nanoparticles: 4, 7, 10 and 13 at%, corresponding to 2, 4, 6 and 8 carbon interstitials, respectively. For these nanoparticles, the computation of the cohesive energy was repeated. To account for the additional carbon atoms, the term $-kE_C$ is added to the numerator and the term $+k$ to the denominator of $E_{coh}$, where $k$ is the number of carbon atoms and $E_C$ is the total energy of a single carbon atom.

To check if these results are consistent with results at finite temperature, BOMD simulations[145] were performed on the most stable NiFe nanoparticles with and without interstitial carbons. The average cohesive energies were computed and compared to the cohesive energies from DFT results.

For both DFT and BOMD calculations, the VASP software was used.[95–98] The generalized gradient approximation (GGA) with revised Perdew-Burke-Ernzerhof (RPBE) functional[100] and the projector augmented wave method (PAW)[78,79] were used for all calculations. All nanoparticles were modelled in a (20x20x20)Å supercell. A $\Gamma$-centered (1x1x1) k-point mesh and Methfessel-Paxton smearing of the first order were used.[101] All calculations were spin polarized, with no symmetry constraints and an energy cutoff of 400 eV. The energy convergence was set to $1 \times 10^{-4}$ eV for the DFT calculations and to $1 \times 10^{-5}$ eV for the BOMD calculations. For the canonical ensemble, a Nosé-Hoover thermostat[86,87] at 700 K was used. The BOMD calculations ran for 2000 time steps of 1 fs.

## 3.3 Results and Discussion

The nanoparticles' stabilities as measured by the cohesive energy and formation enthalpy are given in figures 3.1 and 3.2, respectively. $E_{coh}$ is used to compare different atom distributions within one composition, whereas $\Delta H_{f,NP}$ can also be used to compare the stabilities of different compositions. Figures 3.1a and 3.2a exhibit the results for NiFe, figures 3.1b and 3.2b for NiGa, and figures 3.1c and 3.2c for FeGa.

For each composition we are now able to determine which nanoparticle is most stable. For NiFe, the cohesive energy and the formation enthalpy give the same results. Disagreements between cohesive energy and formation enthalpy may exist due to their different nature: the cohesive energy is a measure of structural stability of the nanoparticle, whereas the formation enthalpy is a measure of thermodynamic stability. In the 25/75 and 75/25 compositions, the most stable nanoparticles are Ni25Fe75_c25Ni and Ni75Fe25_c25Ni. In the 50/50 composition, the most stable nanoparticle is the one where there is no Ni in the core. For NiGa, the cohesive energy and the formation enthalpy do not agree for all compositions. In the 25/75 composition, the highest cohesive energy is found for Ni25Ga75_c50Ni, whereas the lowest formation enthalpy is found for Ni25Ga75_c75Ni. In the 50/50 composition, the highest cohesive energy is found for Ni50Ga50_c100Ni, whereas the lowest formation enthalpy is found for Ni50Ga50_c75Ni. In the 75/25 composition, the cohesive energy and formation enthalpy do agree and the most stable nanoparticle is the one where all of the core atoms are Ni atoms. For FeGa, the cohesive energy and formation enthalpy agree as well, and for all compositions the most stable nanoparticles have a full Fe core.

The differences in cohesive energy and in formation enthalpy for different nanoparticles are rather small, in particular for the NiFe alloys. The stability differences for NiGa and FeGa are slightly larger. These observations can be explained by considering that Ni and Fe have much more similarities than Ni and Ga or Fe and Ga. Notwithstanding the relatively small differences, two general conclusions are drawn from these results: it is more favorable in terms of the stability to have more Fe in the core and more Ga on the surface of a nanopar-

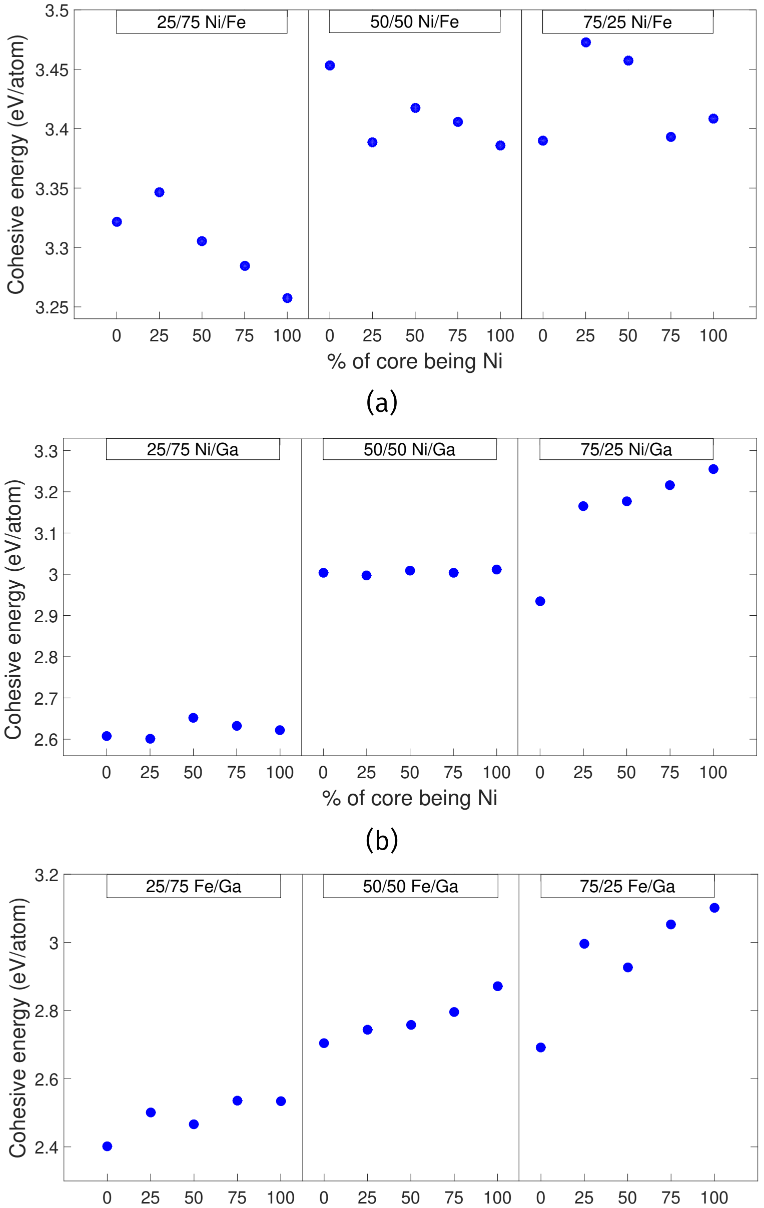

Figure 3.1: Cohesive energies of NiFe (a), NiGa (b) and FeGa (c) nanoparticles. Stabilities are compared for each composition, over atom distributions.

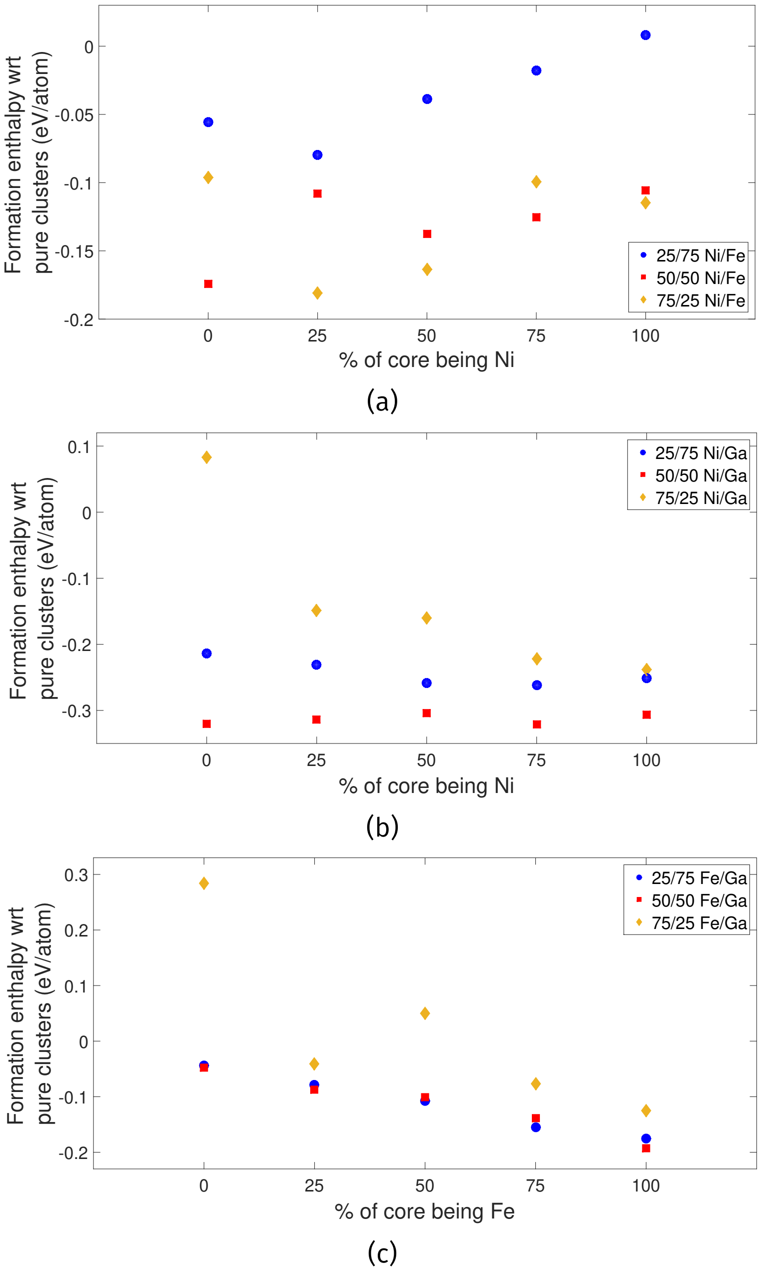

Figure 3.2: Formation enthalpies of NiFe (a), NiGa (b) and FeGa (c) nanoparticles. Stabilities are compared over atom distributions and over compositions.

ticle. These trends can be explained by comparing them with four properties. Firstly, we calculated the cohesive energies of the pure Ni, Fe and Ga cuboctahedra to be 3.31 eV/atom, 3.25 eV/atom, 2.08 eV/atom respectively. The large difference in cohesive energy between Ga and the other two may indicate a preference towards more Ga on the surface of a nanoparticle. Secondly, also the cohesive energies for the pure elements Ni, Fe and Ga indicate this same preference, as they amount to 4.44 eV/atom, 4.28 eV/atom and 2.8 eV/atom respectively.[146] Thirdly, the atom sizes may play a role in the observed effects. For the atom sizes the so-called “crystal” radii described by Shannon et al. were taken.[147,148] In this case Ni, Fe and Ga have radii of 0.70 Å, 0.69 Å and 0.76 Å, respectively. Larger atoms are more likely to be present on the surface of a nanoparticle, thus the atom sizes corroborate the observed trends. Lastly, an element’s smaller surface energy may indicate a preference towards a surface position. The surface energy references were taken from two sources. Aqra et al. calculated solid metals’ energies from theoretical calculations for liquid metals, and give 0.16 eV/Å$^2$, 0.14 eV/Å$^2$ and 0.062 eV/Å$^2$ for Ni, Fe and Ga, respectively.[149] Surface energy computations of an element’s different crystal facets based on DFT were conducted by Vitos et al.[150] They computed energies for Ni fcc, Fe bcc and Ga body centered tetragonal systems. Cuboctahedra have both (111) and (100) facets, and we therefore specifically considered these facets. For the (111) facet, Vitos et al. found surface energy values of 0.13 eV/Å$^2$ and 0.17 eV/Å$^2$ for Ni and Fe, respectively.[150] For Ga no results for this facet are available. For the (100) facet 0.15 eV/Å$^2$, 0.14 eV/Å$^2$ and 0.048 eV/Å$^2$ were found for Ni, Fe and Ga respectively.[150] The Ga (001) facet, which is not equivalent to (100) in this crystal structure, has a surface energy of 0.041 eV/Å$^2$.[150] For the (111) facet, Fe has the highest surface energy and hence the highest tendency to be present in the core of a nanoparticle. For the (100) facet, the surface energy of Fe is only slightly lower than that of Ni. Ga exhibits the lowest surface energy and can thus be expected to be preferred on the surface over Ni and Fe. In general, these four properties validate our results.

Based solely on the formation enthalpy, we can also determine the compositions with the highest stability. For NiFe, the 25/75 composition is the least stable, irrespective of the atom distribution. The most stable composition, in contrast, does depend on the atom distribution: the 50/50 composition is most stable for Ni50Fe50_c0Ni and Ni50Fe50_c75Ni, and the 75/25 composition is most stable for Ni75Fe25_c25Ni, Ni75Fe25_c50Ni and Ni75Fe25_c100Ni. For NiGa, the 50/50 composition has the highest stability for all atom distributions. For FeGa, again 2 compositions have very similar stabilities. The 25/75 composition has the highest stability for for Fe25Ga75_c50Fe and Fe25Ga75_c75Fe, and the 50/50 composition has the highest stability for Fe50Ga50_c0Fe, Fe50Ga50_c25Fe and Fe50Ga50_c100Fe. The 75/25 composition has the lowest stability.

As one of the applications of bimetallic nanoparticles is their use as catalysts

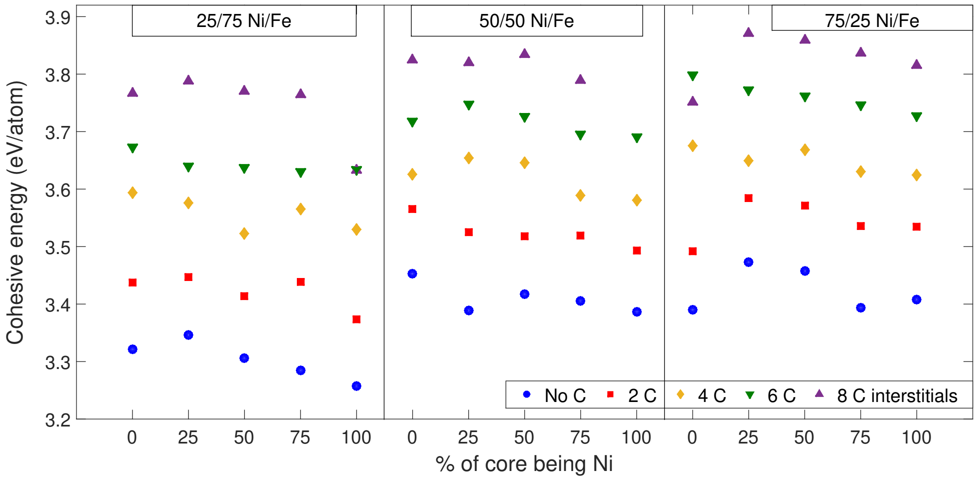

Figure 3.3: Stabilities of NiFe nanoparticles with carbon interstitials. The cohesive energy is computed through DFT calculations.

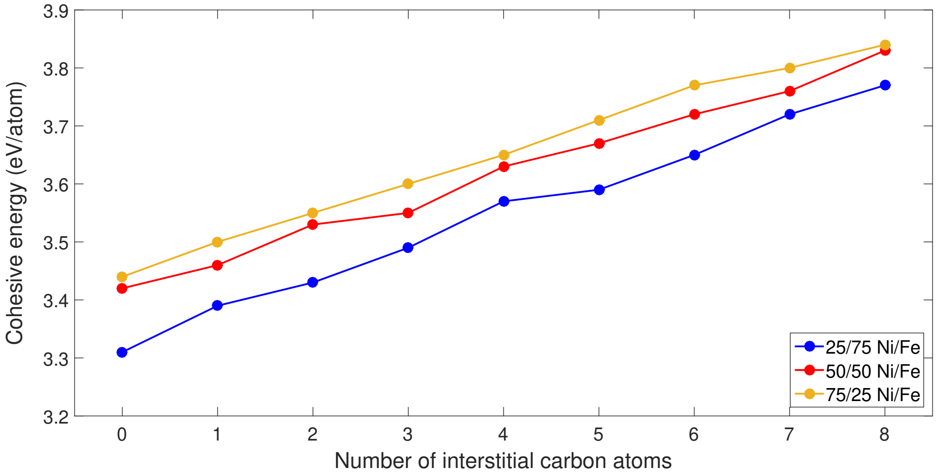

Figure 3.4: Boltzmann weighted average of cohesive energy over atom distributions.

for CNT growth, it is of interest to investigate the effect of carbon interstitials on their stability. We study this effect by comparing cohesive energies for various carbon concentrations. To further investigate the effect of the carbon interstitials on the nanoparticles' stabilities, the Boltzmann weighted average of the cohesive energy over different atom distributions was calculated. These stability results are given in figures 3.3 and 3.4.

Figure 3.3 shows the cohesive energies for all studied nanoparticles. These results indicate that the general trend of increasing nanoparticle stability when a larger part of the core consists of Fe, is mostly retained. Figure 3.4 shows the average cohesive energy, Boltzmann weighted at 1000 K per composition. These averaged results suggest that the 75/25 composition has the highest cohesive energy, and the 25/75 composition the lowest cohesive energy. Furthermore, figure 3.4 indicates an increase of the cohesive energy upon the addition of carbon interstitials. Therefore, we can conclude that carbon interstitials lead to an increase in the nanoparticles' stabilities, but that they only have a small influence on the general stability trend over metal atom distributions and compositions.

All previous computations correspond to static 0 K conditions. However, CCVD growth of CNTs is experimentally carried out at temperatures ranging from 600 to 1300 K. To investigate if the results on the influence of interstitial carbons are representative for nanoparticles in an environment at higher temperature, BOMD simulations were performed at 700 K. Such BOMD simulations were performed for the most stable NiFe nanoparticle of each composition. As mentioned before, these are Ni25Fe75_c25Ni, Ni50Fe50_c0Ni and Ni75Fe25_c25Ni. The average cohesive energies were computed based on snapshots over the last 1000 fs of the simulations with an interval of 1 fs, thus corresponding to 1000 data points. The results are shown in figure 3.5: Ni25Fe75_c25Ni in figure 3.5a, Ni50Fe50_c0Ni in figure 3.5b and Ni75Fe25_c25Ni in 3.5c. It can be observed in the figure that the cohesive energy, and thus the stability, indeed increases with the number of carbon interstitials. Since the BOMD results agree well with the DFT results at 0 K, the DFT results are representative for nanoparticles at higher temperatures. Notwithstanding this result, it should be realized that such small nanoparticles are likely to be liquid at elevated temperatures, due to the Gibbs-Thomson effect.[133,151,152]

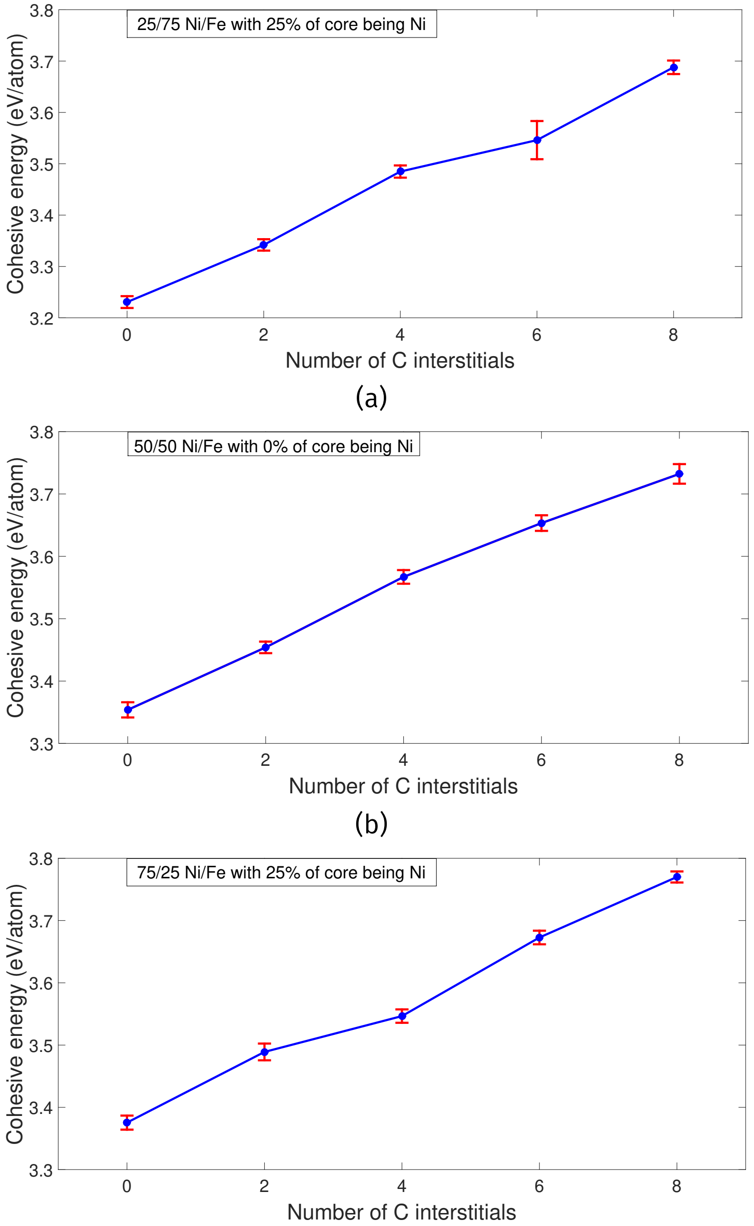

(a)

(b)

(c)

Figure 3.5: Stabilities of selected NiFe nanoparticles with carbon interstitials at 700 K: 25Ni75Fe_c25Ni (a), 50Ni50Fe_c0Ni (b), 75Ni25Fe_c25Ni (c). The cohesive energies are the averages of the second half of the BOMD simulations.

## 3.4 Conclusions

Stabilities of NiFe, NiGa and FeGa nanoparticles with various compositions and atom distributions have been computed through DFT calculations. In general, it was found that nanoparticles with more Fe in the core and more Ga on the surface are more stable. This trend is most obvious for FeGa. Which composition has the highest stability depends on the alloy and on the atom distribution. The influence of interstitial carbons on NiFe stabilities was investigated through both DFT and BOMD calculations. Both show that the stability of a NiFe nanoparticle increases with the number of carbon interstitials. In general, the trend in stability over atom distributions depends somewhat on the carbon content, but the overall trend of nanoparticles with more Fe in the core being more stable is maintained, as is the trend that 25/75 is the most stable composition for NiFe nanoparticles. These results provide insight into the influence of carbon interstitials on the nanoparticle stability and will hopefully stimulate the computational research into chirality-selective CNT growth.

# 4 Tuning single-walled carbon nanotube adhesion energies using bimetallic catalysts

The mechanisms underpinning chirality formation in single-walled carbon nanotube (SWCNT) growth have not yet unequivocally been determined. This chapter addresses the question whether the SWCNT adhesion energy can be tuned using bimetallic catalysts in order to achieve chirality-selective growth. Within a density functional theory framework, we analyse the adhesion energies of SWCNTs of various chiralities on Fe, Ni and FeNi bimetallic nanoparticles. We validate the computational results with existing experimental work on Ni and FeNi bimetallic catalysts. Our results show that the adhesion energy can be tuned by changing the FeNi composition of the catalyst. Based on our findings, we conclude that for $Fe_{1.0}$, $Ni_{1.0}$ and $Fe_{0.5}Ni_{0.5}$ compositions the adhesion energy show no chiral selectivity. However, for bimetallic catalysts of less equal compositions $Fe_{0.75}Ni_{0.25}$ and $Fe_{0.25}Ni_{0.75}$ our results point to zigzag and armchair selectivity respectively.

*Publication:* Charlotte Vets, Daniel Hedman, J. Andreas Larsson and Erik C. Neyts. Tuning Single-Walled Carbon Nanotube Adhesion Energies using Bimetallic Catalysts. *In preparation.*

*Author contribution:* DFT calculations and interpretation, comparison with experimental work of Chiang et al.[39]

## 4.1 Introduction

Single-walled carbon nanotubes (SWCNTs) show tremendous potential for a variety of applications, owing to their outstanding properties, such as a spectacular tensile strength[14] and elastic modulus.[13] Furthermore, the tunability of their electronic properties makes them particularly suitable for opto-electronic applications. Some examples include their use as channel material in field-effect transistors,[4,5] thermal conductors[7] and interconnects[6] in integrated circuits, and gas sensors.[8] Nevertheless, SWCNTs have not yet been able to fulfil their potential in these opto-electronic applications, as there is currently only limited control over their electronic properties. As the electronic properties are determined by the chirality (n,m) of the SWCNT, it is of paramount importance to achieve chirality-selective growth to gain full control of these properties.[18]
The SWCNT chirality is determined by the diameter and the roll direction of the graphene sheet. Since the SWCNT diameter is related to the diameter of the catalyst, tuning the nanoparticle (NP) diameter leads to diameter control of the SWCNT.[34] On the other hand, the roll direction, or chiral angle, is much more difficult to control but is crucial to achieving chirality-selective SWCNT growth.[35–38]
The driving factor for the chirality resulting from the growth is still a matter of debate. The thermodynamic stability of the system has been put forward as a possible driving factor.[37,44,45] Studies have focused on various reasons for this, such as a correlation between the catalyst structure and the SWCNTâĂŹs chirality,[46,47] the edge energy of a graphene strip with certain chirality,[48] or a combination of edge energy and curvature effects in a SWCNT.[49] The thermodynamic stability of the system can be investigated through, amongst others, the adhesion energy of a SWCNT attached to a NP. The adhesion energy has been deemed paramount for SWCNT growth and is therefore the more specific thermodynamic driving factor.[18,50,51] Other research however suggests that the adhesion energy differences between chiralities are too small to promote chirality-selective SWCNT growth.[52] Moreover, Neyts et al. have proven that the chirality is still subject to change during the nucleation phase.[53]
Bimetallic NPs may provide a solution for chirality-selective SWCNT growth. Experimentally, narrow chirality distributions have indeed been obtained with bimetallic catalysts, such as NiFe,[39] CoMo[153] and CoPt.[41] The reason for this may lie in the Goldilocks principle,[18] which states that SWCNTs can only be formed if the carbon-metal binding energy (adhesion energy) is situated in a certain energy range, i.e. the Goldilocks zone. Only a few metals follow the Goldilocks principle, but by combining metals with too weak and too strong adhesion energies, the corresponding Goldilocks zone can be reached for bimetallic NPs.
Considerable experimental research has been devoted to bimetallic NPs for chirality-selective SWCNT growth.[39,41,153] Similarly, a great effort has been made

to calculate adhesion energies of armchair and zigzag SWCNTs on monometallic NPs.[18,50,51] However, the computation of adhesion energies of SWCNTs on bimetallic NPs is still scarce.[154,155] This study therefore addresses the adhesion energies of SWCNTs with various chiralities on FeNi bimetallic NPs. We compute the adhesion energies using density functional theory (DFT) and analyse these results for various interstitial carbon concentrations in the NPs. These results are then compared with the results for pure Fe and Ni NPs. Moreover, we establish a link with existing experimental research on SWCNT growth from Ni and FeNi NPs. Based on these results, we discuss whether the adhesion energy can be tuned and whether or not it can be the driving force for the chirality.

## 4.2 Computational details

To keep the calculations feasible, NP-SWCNT complexes consisting of 55-atom nanoparticles and SWCNT-fragments having a length between 0.58 and 0.71 nm were modelled. Cuboctahedra NPs were chosen as catalyst systems to avoid wide spreads in adhesion energies that would arise from amorphous structures, due to local and random SWCNT-catalyst interactions. While the cuboctahedron is geometrically not a realistic model for real nanoparticles at experimental growth temperatures, this choice allows for a systematic screening of the interaction. The nanoparticles studied are Fe cuboctahedra, Ni cuboctahedra and FeNi cuboctahedra with three compositions $Fe_{0.75}Ni_{0.25}$, $Fe_{0.5}Ni_{0.5}$ and $Fe_{0.25}Ni_{0.75}$. For each composition, the most stable atom distributions as outlined in our previous work were chosen to build adhesion systems with.[27] Since carbon dissolved in nanoparticles is crucial for SWCNT growth, nanoparticles with 0, 4 and 8 interstitial carbon atoms are studied. As the diameter of the nanoparticles is about 0.8 nm, we choose seven hydrogen-passivated SWCNT-fragments with a similar diameter resulting in the following chiralities: (6,6), (6,5), (7,4), (8,3), (9,2), (9,1) and (9,0).[35] An illustration of a model system is shown in Figure 4.1.

The NP-SWCNT complexes and the individual SWCNT-fragments were geometrically optimized through DFT calculations. The NPs were optimized as described in our previous work[27] and reoptimized after detaching the SWCNT-fragment. The Vienna Ab initio Simulation Package (VASP) was used for all calculations.[95,96] All systems were optimized with no symmetry constraints using the generalized gradient approximation (GGA), employing the revised Perdew-Burke-Ernzerhof (RPBE) functional,[100] and with the projector augmented wave method (PAW).[78,79] The k-point mesh was $\Gamma$-centered (1 x 1 x 1) and the smearing method was Methfessel-Paxton of the first order.[101] Supercells of sizes (20 x 20 x 20) Å and (20 x 23 x 30) Å were used for the SWCNT-fragments and NP-SWCNT complexes respectively. Spin polarization with a high-spin ferromagnetic initia-

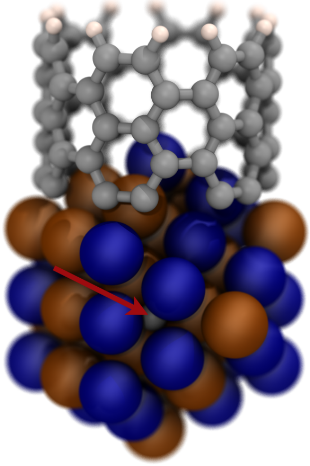

Figure 4.1: An illustration of a model system used in this work. This example model is comprised of a hydrogen-passivated (6,6) SWCNT attached to a $Fe_{0.5}Ni_{0.5}$ NP containing four C interstitials (one is indicated by the red arrow). Here blue atoms represents H, black C, grey Ni and gold Fe.

lization of the NPs was employed. The energy cutoff was set to 400 eV, and the energy convergence to $1 \times 10^{-6}$ eV. After geometrical optimization, vibrational analysis was performed in VASP with the finite differences method. With these results, zero-point analysis was then performed with the TAMkin package.[156] For each system, the adhesion energy is computed as follows

$$(n+m) \cdot E_{adh.} = E_{CX} - \left(E_{NP} + \hat{E}_{\overline{CNT}}\right), \tag{4.1}$$

where $E_{CX}$ is the total energy of the geometrically optimized complexes and $E_{NP}$ is the total energy of the optimized NPs. $\hat{E}_{\overline{CNT}}$ is the fragment stabilization[52,157] corrected total energy of the optimized SWCNT-fragment given by

$$\hat{E}^{n,m}_{\overline{CNT}} = E^{n+m,0}_{\overline{CNT}} + \left(\frac{E^{n,m}_{CNT} - E^{n+m,0}_{CNT}}{2}\right). \tag{4.2}$$

Here, $E_{\overline{CNT}}$ is the total energy of the SWCNT-fragments and $E_{CNT}$ is the energy of SWCNT-fragments with twice the length (both edges hydrogen-passivated). All energies include zero-point energy corrections, and due to the definition of Eq. 4.1 a more negative adhesion energy indicates a stronger bond. Because of the spread in the calculated adhesion energies (noise) caused by an imperfect SWCNT/NP interface the following equation (derived from [48]) was fitted to the

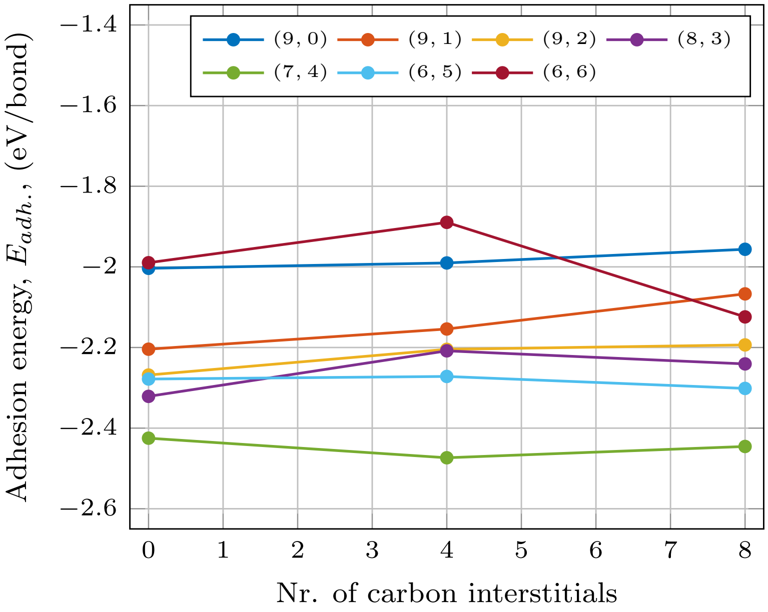

Figure 4.2: The effect of carbon interstitials on the adhesion energy for all chiralities attached to the $Ni_{1.0}$ NP. Here the dots represent the DFT calculated adhesion energies for 0, 4 and 8 carbon interstitials. The dots are connected by solid lines to help guide the eye.

data and used for further analysis:

$$E_{adh.} = \frac{2m}{n+m} E^{ac}_{adh.} + \frac{(n-m)}{n+m} E^{zz}_{adh.}. \tag{4.3}$$

## 4.3 Results & Discussion

The effect of carbon interstitials on the adhesion energy is shown in Figure 4.2 for Ni NPs. Here itâĂŹs clear that for 8 or fewer carbon interstitials, there is only a very small effect (max. $\pm 0.1$ eV/bond) on the adhesion energy. This is in agreement with previous studies on Ni catalysts[158] and our calculations for Fe and FeNi NPs show the same result. Thus, we conclude that carbon interstitials have a negligible effect on the adhesion energy and present the rest of the results for only zero carbon interstitials e.g. pure metallic NPs.

The computed adhesion energies are given as the dots in Figure 4.3a for all chiralities and NP compositions, here it is clear that the trends for all NPs are quite similar. For the pure Fe NP the local minimum in the DFT calculated adhesion energies is found at (7,4). Adding a small amount of Ni to the Fe NP, $Fe_{0.75}Ni_{0.25}$, shifts the local minimum towards zigzag, (9,2), where it is also found for the

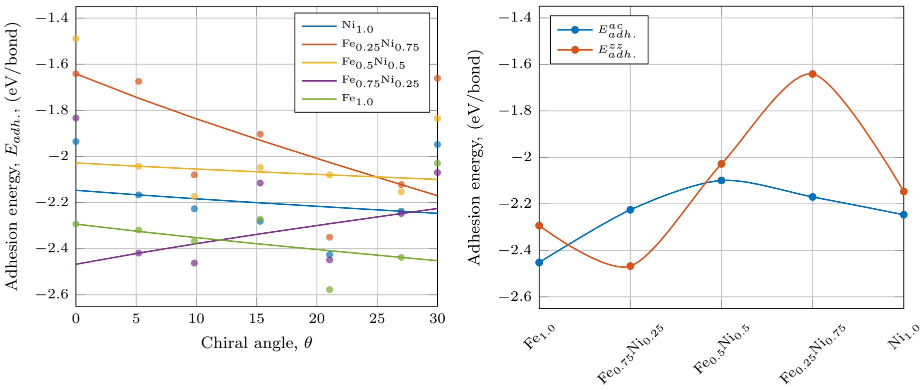

(a) (b)

Figure 4.3: Adhesion energies derived from the zero-point corrected DFT energies and from fitting Eq. (4.3) to the DFT data. (a) $E_{adh.}$ for all 7 H-terminated SWCNT-fragments: (9,0), (9,1), (9,2), (8,3), (7,4), (6,5) and (6,6) as a function of the chiral angle, $\theta$. Here, the dots represent adhesion energies derived from DFT and the solid lines are Eq. (4.3) fitted to the data. (b) Armchair, $E^{ac}_{adh.}$, and zigzag, $E^{zz}_{adh.}$, adhesion energies as a function of the NP composition. Here, the dots represent $E^{ac}_{adh.}$ and $E^{zz}_{adh.}$ obtained from the fitting of Eq. (4.3) in (a). The dots are connected by a spline curve to help guide the eye.

$Fe_{0.5}Ni_{0.5}$ composition. Further increasing the Ni content in the NP, $Fe_{0.25}Ni_{0.75}$, shifts the local minimum back towards armchair, (7,4), the same as for the pure Ni composition.

The adhesion energy differences between local minima and the other chiralities are quite small: $< 0.2$ eV/bond for most NP compositions, except for $Fe_{0.25}Ni_{0.75}$. Thus, for most of the NP compositions studied with DFT in this work, the difference in adhesion energies is too small to affect the chirality during growth, with the exception of those for $Fe_{0.25}Ni_{0.75}$.

However, due to the spread in adhesion energies (because of imperfect SWCNT /NP interfaces), it is hard to draw any firm conclusions about selectivity for specific chiralities. We note that our SWCNT-fragments have different numbers of edge atoms (n+m), which leads to variations in the number of metal atoms that are involved in perfect bonding to the edge, i.e. the number of bonding metal atoms is frequently $< (n+m)$. This is especially obvious for the (6,6) tube where the adhesion energy is very low, since it is the only tube with $n + m = 12$ edge atoms.

To further analyse the data, and remove the effects of any outliers, we fit Eq. (4.1) to the DFT calculated adhesion energies (solid lines in Figure 4.3a). Before discussing these results, we note that the difference in adhesion energies from DFT calculations and from fitting with Eq. (4.1) is quite large for some of the data points. This is most probably due to a combination of the interface and the reconfiguration energy. The interface energy, as discussed above, arises because of imperfect SWCNT/NP interfaces. The reconfiguration energy, on the other hand, emerges when the NPs are reoptimized after detaching the SWCNT-fragment. Therefore, outliers will be present in the DFT data. Their effect on the adhesion energy trends is thus removed by fitting with Eq. (4.1).

In Figure 4.3a, we can see that for $Fe_{1.0}$, $Fe_{0.5}Ni_{0.5}$ and $Ni_{1.0}$ the change in adhesion energy as a function of chirality is small: $< -0.2$ eV/bond from $\theta = 0$ to 30°. But for the remaining two compositions, $Fe_{0.25}Ni_{0.75}$ and $Fe_{0.75}Ni_{0.25}$, the change in adhesion energy is larger, $-0.53$ eV/bond from $\theta = 0$ to 30° and $0.24$ eV/bond from $\theta = 0$ to 30° respectively. Interestingly, the change in adhesion energy is positive for the $Fe_{0.75}Ni_{0.25}$ composition showing a preference towards zigzag chiralities, in agreement with the local minima analysis.

The same conclusion can be drawn from the armchair and zigzag adhesion energies, $E^{ac}_{adh.}$ and $E^{zz}_{adh.}$, obtained from fitting. As seen in Figure 4.3b the difference between $E^{ac}_{adh.}$ and $E^{zz}_{adh.}$ is small for $Fe_{1.0}$, $Fe_{0.5}Ni_{0.5}$ and $Ni_{1.0}$ but large for $Fe_{0.75}Ni_{0.25}$ and $Fe_{0.25}Ni_{0.75}$. Interestingly, here the zigzag adhesion energy for the $Fe_{0.25}Ni_{0.75}$ composition is outside the Goldilocks zone as defined in,[18] which points to strong selectivity towards armchair chiralities for the $Fe_{0.25}Ni_{0.75}$ composition.

We compare our results with the experimental work of Chiang et al.,[39] noting that the chiralities obtained by Chiang et al. are different from the chiralities used here. They used nanoparticles with a larger diameter (approximately 2.0 nm) which resulted in growth of SWCNT with diameters of 0.82 to 0.90 nm. As explained earlier, the chirality is related to the diameter and the chiral angle $\theta$, which can be seen in the chirality map in Figure 4.4.

The blue lines indicate $\theta$ = 0° (zigzag) and $\theta$ = 30° (armchair). The orange chiralities correspond to the SWCNTs studied here. These SWCNTs have diameters of about 0.8 nm, as indicated in the chirality map by the green line. The yellow chiralities correspond to the SWCNTs Chiang et al. determined using photoluminescence. The red lines are drawn on chiral angles of $\theta$ = 9.8°, $\theta$ = 15.3°, $\theta$ = 21.1° and $\theta$ = 27°, corresponding to our (9,2), (8,3), (7,4) and (6,5) SWCNTs. The chiral angle $\theta$ was calculated as follows

$$\theta = \tan^{-1}\left(\frac{\sqrt{3}m}{2n+m}\right), \tag{4.4}$$

where n and m are the chiral indices.

If two SWCNTs with different diameters have a similar chiral angle, we can assume that these nanotubes are strongly related. This can be observed using

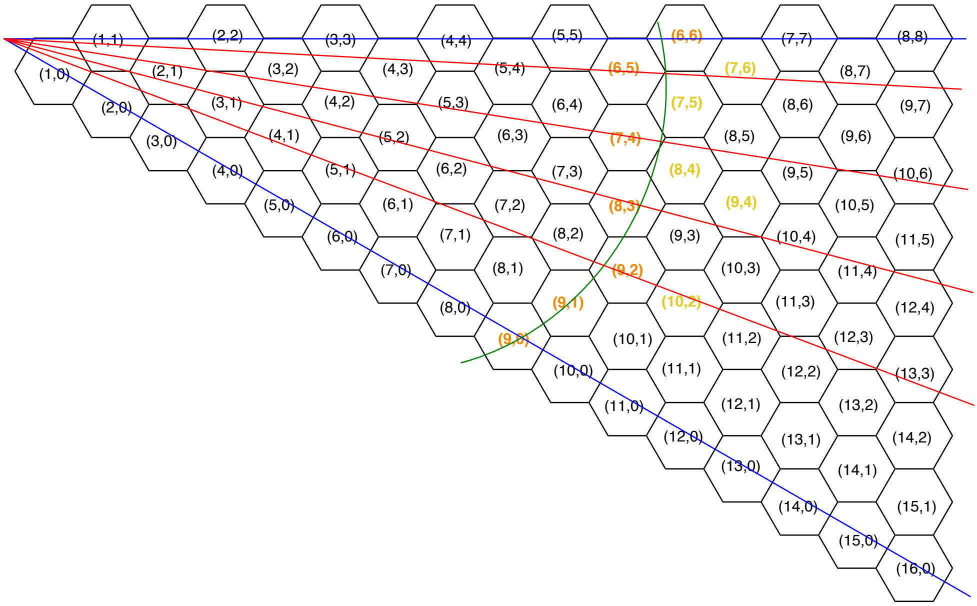

Figure 4.4: Chirality map, where blue lines indicate chiral angles of 0° and 30°, i.e. zigzag and armchair SWCNTs. Chiral indices marked in orange are the SWCNTs investigated in this paper, they have a diameter of about 0.8 nm as indicated with the green curve on the map. The yellow chiral indices are the SWCNTs obtained by Chiang et al.[39] Red lines correspond to (6,5), (7,4), (8,3) and (9,2) tubes with a chiral angle of 27°, 21.1°, 15.3° and 9.8° respectively, these lines intersect all SWCNTs on the chirality map with a similar chiral angle. Therefore, it can be used to check with which of the SWCNTs from Chiang et al.'s work our tubes can be compared.

the red lines in the chirality map in Figure 4.4 where chiralities that are intersected by the same red line are thus related. Chiang et al.'s chiralities which are similar to ours can therefore be collected from the chirality map. An overview of which of Chiang et al.'s SWCNTs that we will use for comparison to our results is given in Table 4.1.

Now we can observe that the results from fitting Eq.(4.3) are consistent with the experimental work of Chiang et al.,[39] as can be seen by comparing our calculated adhesion energies (Figure 4.3a) with the photoluminescence (PL) maps they obtained. They observed a much narrower chirality distribution for FeNi bimetallic catalysts than for pure Ni ones. This can be correlated with our results that show only a slight variation in adhesion energies for the different chiralities when using pure Fe or pure Ni NPs. In addition, Chiang et al.'s $Fe_{0.5}Ni_{0.5}$

Table 4.1: Chiral angles of SWCNTs obtained by Chiang et al.[39] and corresponding chiral angles of our SWCNTs.

| **Chiang et al.** | | **This work** | |
|---|---|---|---|
| (n,m) | $\theta$, (°) | (n,m) | $\theta$, (°) |
| (6,5) | 27 | (6,5) | 27 |
| (7,6) | 27.5 | (6,5) | 27 |
| (7,5) | 24.5 | (6,5) | 27 |
| (8,4) | 19.1 | (7,4) | 21.1 |
| (9,4) | 17.5 | (8,3) | 15.3 |
| (10,2) | 8.9 | (9,2) | 9.8 |

catalyst exhibited a narrower chirality distribution than the pure Ni catalyst, however it is still broader than for their other FeNi catalysts. Similarly, for our $Fe_{0.5}Ni_{0.5}$ catalyst only a slight variation in adhesion energies can be discerned. Whereas the adhesion energies for $Fe_{0.25}Ni_{0.75}$ and $Fe_{0.75}Ni_{0.25}$ bimetallic catalysts clearly favour armchair and zigzag chiralities respectively, in agreement with the results of Chiang et al.

## 4.4 Conclusions

Adhesion systems of various SWCNTs on Ni, Fe, and FeNi NPs have been modelled through DFT calculations. The influence of carbon interstitials was analysed and deemed not significant. The DFT results were fitted to compensate for the imperfect NP-SWCNT interface. Whereas the DFT results only show weak trends due to limitations of the systems used in this work, the fits showed trends consistent with previous experimental work by Chiang et al. Depending on the FeNi composition, no chiral preference or a preference towards armchair/zigzag chiralities could be observed. Pure metal NPs and $Fe_{0.5}Ni_{0.5}$ NPs showed no significant preference but $Fe_{0.75}Ni_{0.25}$ and $Fe_{0.25}Ni_{0.75}$ NPs on the other hand favour zigzag and armchair chiralities respectively.

# 5 Influence of catalyst structure on defect stabilities and healing in carbon nanotubes

Defect healing has been proposed as an important process in the chirality formation and chirality change during growth of carbon nanotubes. A central facet in defect healing is the influence of the contact between the defect and the metal catalyst nanoparticle. In this study, the defect healing process was explored through the defect stabilities. Drawing on molecular dynamics simulations, the stabilities of carbon nanotubes with 5-7 defects, Stone-Wales defects and vacancies were evaluated on five different Ni nanoparticles. Our study demonstrates that the structure of the nanoparticle contributes significantly to the defect healing process. Moreover, the impact on the relative defect stabilities is quite apparent. These results not only support the proposed influence of metal-defect interface, but also reveal a significant impact of the exact metal catalyst structure on the defect stability and on the probability of defect healing.

## 5.1 Introduction

Carbon nanotubes (CNTs) have exceptional properties, such as an extremely high tensile strength[14] and elastic modulus.[13] Nevertheless, they are mostly promising for a number of opto-electronic applications, such as field-effect transistors,[4,5] gas sensors,[8] and thermal conductors[7] and interconnects[6] in integrated circuits. This is owing to their highly attractive electronic properties. Moreover, not only are these electronic properties exceptional, but they are also tunable, which even increases the potential of CNTs. Unfortunately, complete control over CNTs' electronic properties has not yet been achieved. In order to tune their electronic properties, their chiralities need to be tuned. In spite of tremendous efforts to control CNTs' chiralities, complete chirality control has not been achieved as of yet.

Both the diameter and the chiral angle of the CNT determine its chirality.[18] Therefore, for chirality selective growth to be successful, both the diameter and the chiral angle should be controlled. The diameter can be selected by tuning the diameter of the catalyst nanoparticle.[34] Control of the chiral angle however is harder to reach, but nevertheless paramount.[35-38]

As the driving force for chirality formation during growth is still elusive, several potential routes for chirality control exist. On the one hand, chirality control through the thermodynamic stability has been suggested.[37,44,45] On the other hand, the exact role of the thermodynamic stability is still unclear,[52] and CNT growth is a non-equilibrium process, therefore also kinetics play a role in the growth, allowing the chirality to change even during the nucleation phase.[53] Two of the kinetic processes active during growth are defect formation and defect healing. When a defect grows into the CNT without being healed, it will cause the CNT chirality to change, which is not desirable for chirality control. Hence, defect healing is an important process to be taken into account for chirality selective growth.

The healing of a defect is aided by the proximity of a metal interface, which is proved by the example of a Stone-Wales (SW) defect. Healing a SW defect in a pure carbon network has an energy barrier in the order of 5 - 7 eV,[53] while healing the same defect in contact with the metal only has a barrier in the order of 1 - 2 eV.[54] During CNT growth, it is thus preferable that the defect be healed while still in contact with the metal catalyst.

For this reason, we studied CNTs with defects that are in contact with metallic nanoparticles. As Ni nanoparticles are often used as catalyst for CNT growth, we study Ni nanoparticles specifically. Using molecular dynamics (MD) simulations, we calculate the energy difference between model systems with defected CNTs and with perfect CNTs. This allows us to find out how likely the defect will heal. The likelihood of healing is studied for SW defects, 5-7 defects, and vacancies. It is then compared with information from visualizations of our MD simulations.

Based on our findings, we discuss the influence of the nanoparticle structure on healing of those defects.

## 5.2 Computational details

As mentioned previously, Ni nanoparticles (NPs) are used as catalysts in our simulations. The NPs are amorphous and consist of 55 Ni atoms. They contain an additional 17 C atoms, to account for the C dissolved in the catalyst during a real CNT growth experiment. Five different NPs were used, all with the same amount of atoms, but structurally different. This allows us to check the differences in defect healing for various NPs. On the NPs, CNTs are adsorbed. The starting point for all CNTs were (5,5) nanotubes that are hydrogen-passivated. Aside from the CNTs with perfect carbon network, there are three CNT model systems with various defects: a 5-7 defect, a Stone-Wales defect and a vacancy. This to compare the influence of the catalyst on the healing of various defects. Graphic representations of the models systems can be found in figure 5.1: a perfect CNT in figure 5.1a, a CNT with a 5-7 defect in figure 5.1b, a CNT with a SW defect in figure 5.1c, and a CNT with a vacancy in figure 5.1d.
The MD simulations were executed with the ReaxFF software,[102] using the Mueller reactive force field.[159] The NpT ensemble was employed, with a Nosé-Hoover chain thermostat. The temperature was set to 1000 K, a common temperature for CNT growth. The simulation was run for 10 ns, with a time step of 0.25 fs. The first ns of the simulation was not regarded for the results. Instead, we use the time average over the last 9 ns of the simulation to obtain the potential energy for each model system.

## 5.3 Results and discussion

First we investigate the averaged potential energies of the various CNTs over the five NPs. Averaging over the NPs allows us to study the results without the influence of the NP's structure. For the 5-7 defect, the SW defect and the vacancy, figure 5.2 exhibits the difference in average potential energy between the model systems with perfect CNT and with defective CNT ($\Delta E_{pot}$). The more negative this average potential energy is, the less stable the system with defective CNT is compared to the system with perfect CNT. As is expected, the 5-7 defect is the least stable with a $\Delta E_{pot}$ of -3.76 eV. This is followed by the vacancy, having a $\Delta E_{pot}$ of -1.75 eV, which is in turn closely followed by the SW defect, having a $\Delta E_{pot}$ of -1.35 eV.
Since these results are exactly as expected, it would be more useful to look at the results for each NP structure separately. These results are given in figure

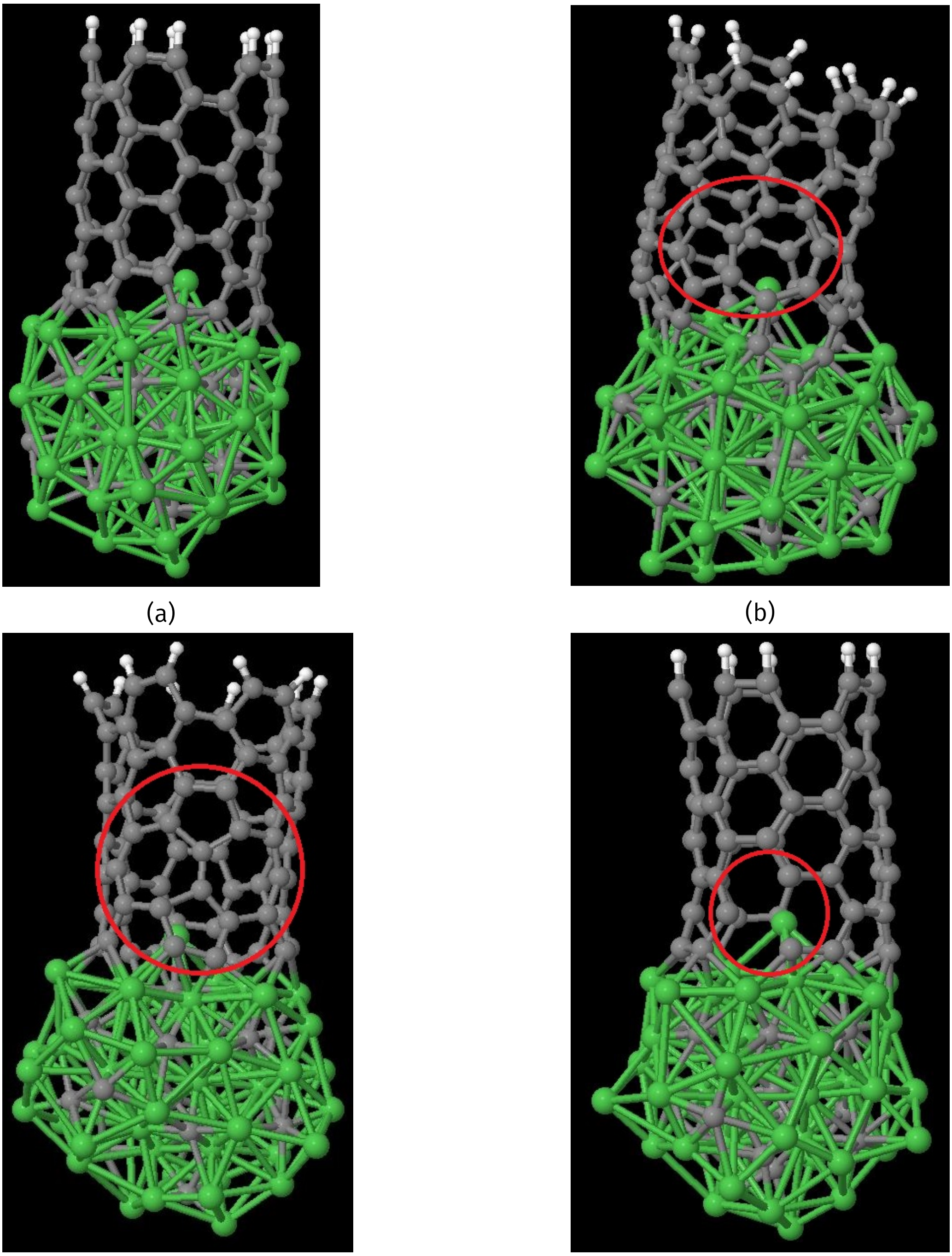

(a) (b) (c) (d)

Figure 5.1: Model systems used in this work with defects circled in red: perfect CNT (5.1a), CNT with 5-7 defect (5.1b), CNT with SW defect (5.1c), and CNT with vacancy (5.1d). Defects were put in contact with the Ni catalyst.

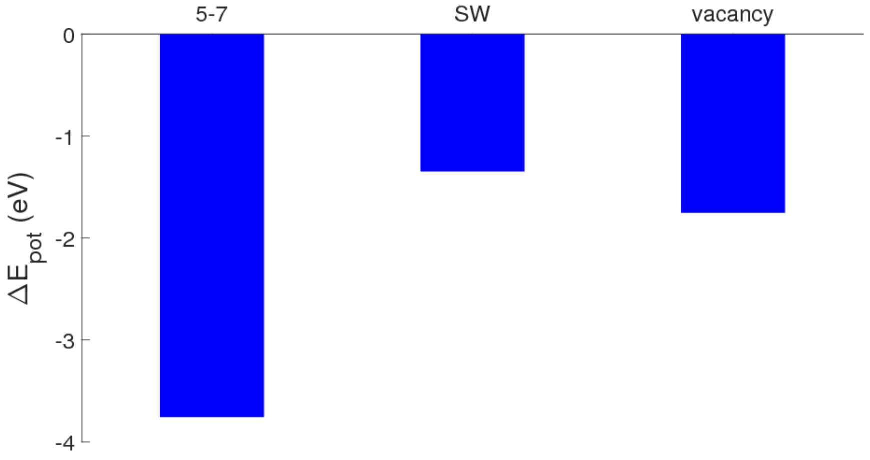

Figure 5.2: Potential energy differences $\Delta E_{pot}$ between systems with perfect CNT and defective CNT ($E_{pot,perfect} - E_{pot,defective}$). The differences were averaged over the five Ni NP structures.

5.3. This figure exhibits large differences in $\Delta E_{pot}$. For each of the five NPs, the 5-7 defect is the least stable defect. The range in $\Delta E_{pot}$ for the 5-7 defect is from -2.71 to -4.63 eV. For most of the NPs, the SW defect is the most stable defect, and for one of the NPs, it is even more stable than the perfect CNT. $\Delta E_{pot}$ ranges from 0.281 to -2.09 eV for the SW defect. Only for one of the NPs, the vacancy is more stable than the SW defect. Otherwise, its $\Delta E_{pot}$ lies between those for the SW defect and the 5-7 defect. $\Delta E_{pot}$ values for the vacancy are between -1.06 and -2.50 eV.
Thus far, these results are not very different from the averaged results in figure 5.2. However, investigating the model structures themselves sheds a slightly different light on the results. Firstly, we investigate the model structure where $\Delta E_{pot}$ is positive for the SW defect. We observed that the 5-ring that had been in contact with the NP at the start of the MD simulation, had disappeared after the simulation. Hence, the SW defect was not complete any more, which could explain the change in stability.

Subsequently, we watch our model systems during the MD simulations to examine whether defect healing occurs and compare this visual information with the results for $\Delta E_{pot}$. The potential energy difference is quite a bit more negative for the 5-7 defect than for the other defects, therefore healing should occur more easily for this defect. Furthermore, since the potential energy difference for the SW defect is least negative (and even positive for one NP structure), defect healing will not occur as often or not at all for this defect. The poten-

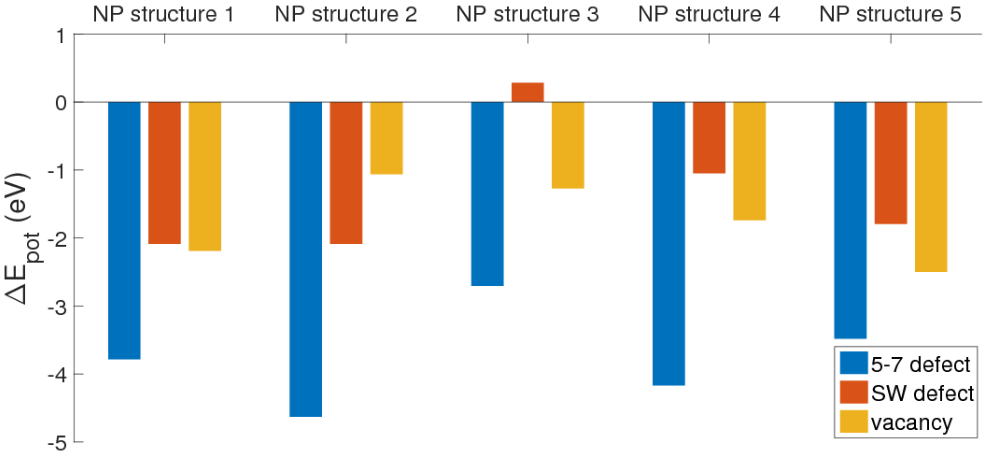

Figure 5.3: Potential energy differences $\Delta E_{pot}$ between perfect CNT and defective CNT ($E_{pot,perfect} - E_{pot,defective}$). $\Delta E_{pot}$ is given for each NP.

tial energy difference is slightly higher for the vacancy, so we expect a slightly higher, but still rare occurrence of defect healing in this case. These results for $\Delta E_{pot}$ are very similar to our visual observations of the model systems during the MD simulations, as we discuss below.

The 5-7 defect was healed on NP structures 2 and 3, but not on NP structures 1, 4 and 5. The vacancy was only healed on NP structure 1. On the other NP structures, the vacancy turned into other defects, i.e. a 5-ring on NP structures 2, 3 and 5, and a 7-ring on NP structure 4. However, no defect-free structures were obtained in these cases. On the other hand, the SW defect did not heal on any of the NP structures. These observations do indeed confirm the results for $\Delta E_{pot}$.

Then, our results give rise to two assumptions regarding the NP structure: besides the relative stability of various defects and perfect CNTs depending greatly on it, it also has a high impact on whether defect healing occurs or not. This could be due to the presence of Ni atoms at certain crucial locations on the NP-CNT interface. Their presence (or absence) could either aid the healing of a defect, or rather stabilize the defect. Therefore, we hypothesize that the NP structure will be important in chiral selectivity when we want to kinetically control the chirality.

It is important to emphasize that the computational set-up of this study limits our interpretations. This study was only performed for Ni NPs, and only for (5,5) CNTs. Consequently, our results remain valid for model systems consisting of Ni NPs and armchair CNTs.

## 5.4 Conclusion

Consistent with previous studies, this study demonstrated that the metal catalyst plays a crucial role in defect healing in CNTs. This study has established that the structure of the catalyst NP also impacts the healing of the defect. A possible explanation could be that the presence of metal atoms at certain locations on the NP-CNT interface is paramount for defect healing. This has implications for the chirality selective growth of CNTs, as defect healing can allow the chirality to remain the same during growth. Further research is imperative to establish whether these results are reproducible for other CNT chiralities and other metal catalysts.

# 6 Catalyzed growth of encapsulated carbyne

Carbyne is a novel material of current interest in nanotechnology. As is typically the case for nanomaterials, the growth process determines the resulting properties. While endohedral carbyne has been successfully synthesized, its catalyst and feedstock-dependent growth mechanism is still elusive. Here we study the nucleation and growth mechanism of different carbon chains in a Ni-containing double walled carbon nanotube using classical molecular dynamics simulations and first-principles calculations. We find that the understanding the competitive role of the metal catalyst and the hydrocarbon is important to control the growth of 1-dimensional carbon chains, including Ni or H-terminated carbyne. Also, we find that the electronic property of the Ni-terminated carbyne can be tuned by steering the H concentration along the chain. These results suggest catalyst-containing carbon nanotubes as a possible synthesis route for carbyne formation.

*Publication:* Umedjon Khalilov, Charlotte Vets, and Erik C. Neyts. Catalyzed growth of encapsulated carbyne. *Carbon*, 153:1-5, 2019. `https://doi.org/10.1016/j.carbon.2019.06.110`

*Author contribution:* DFT and density of states (DOS) calculations and interpretation

## 6.1 Introduction

Carbyne is a 1D carbon allotrope;[160] it is an infinitely long linear chain of sp-hybridized carbon atoms with extraordinary properties.[63,161,162] Specifically its mechanical properties such as the Young modulus (32.71 TPa), shear modulus (11.8 TPa), and specific stiffness (about $10^9$ Nm/kg) significantly outperform any other material including carbon nanotubes, graphene and diamond.[55] Also, its very high thermal conductivity (80 kWm$^{-1}$K$^{-1}$ at room temperature),[11] structure-dependent electronic,[163] and other properties are very attractive.[9,10]
Carbyne is produced using various growth techniques including arc discharge,[57,164,165] laser ablation,[63,166] on-surface synthesis,[167,168] electrochemical synthesis,[169] and others.[64,170] However, the synthesis of long carbyne is extremely difficult due to its high chemical reactivity and instability.[57,58] Nevertheless, such long carbon chains have successfully been obtained to some extent.[65,66,164] Especially, the inner space of carbon nanotubes has been recognized as an ideal location for the carbyne chain[58,61] and thus the endohedral carbyne growth is actively being investigated. In particular, spontaneous formation of linear carbon chains with several tens of C atoms in double walled carbon nanotube (DWNT) has been observed through insertion of precursor molecules, e.g., polyyne $C_nH_2$ molecules[65] and adamantane ($C_{10}H_{16}$).[66] Also, Zhao and colleague reported long linear C chain more than 100 carbon atoms inside multi-walled carbon nanotube (MWNT) obtained by hydrogen arc discharge evaporation of carbon rods.[165] Recently, Shi et al. have experimentally grown record-long carbyne chain with 6000 C atoms inside a DWNT.[61] Several investigations indicate that the high-temperature treatment of MWNT, especially DWNT with suitable innermost diameter allows for the synthesis of long carbon chains [19, 22, 23].[58,61,62]
In the formation of endohedral carbyne from hydrocarbon species, a metal catalyst can facilitate bond breaking and C-C bond formation after feedstock adsorption by decreasing the activation energy barriers of these reactions. In particular, transition metals are used as a catalyst in the steam methane reforming for producing syngas,[171] in the Fischer-Tropsch reactions for producing hydrocarbons,[172] in the synthesis of nanostructures using chemical vapor deposition technique,[32] etc. However, the metal-catalyzed growth of the encapsulated carbyne is not reported yet. Consequently, the growth mechanism, and the role of the catalyst and the feedstock for the case of endohedral carbyne synthesis are still elusive. In order to elucidate these phenomena, we here study the Ni-catalyzed nucleation and growth of carbon chains in DWNT from carbon ($C_2$) and hydrocarbon ($C_2H$ or $C_2H_2$) species, using both reactive Molecular Dynamics (MD) simulations and Density Functional Theory (DFT) calculations.

## 6.2 Computational methodology

In the reactive MD simulations, we use the ReaxFF potential[102] with parameters developed by Zou et al.[103] To grow the endohedral carbyne a (5,5)@(10,10) DWNT is chosen, as shown in Fig. 6.1. The inner ($d_{in}$) and outer ($d_{out}$) diameters of the DWNT are 0.70 nm and 1.39 nm, respectively. These values are in agreement with experimentally reported tube diameters, viz. 0.63 nm $< d_{in} <$ 0.79 nm and 1.3 nm $< d_{out} <$ 1.6 nm.[173] Also, the inner (5,5) nanotube with diameter of about 0.7 nm is optimal to stabilize a carbon chain, in very good agreement with experiments as well.[58, 61, 65] Periodicity is applied along the z-axis, mimicking an infinitely long DWNT. Subsequently, Ni atoms are inserted in the inner tube, mimicking the experimental embedded Ni nanoclusters in carbon nanotubes.[174] Due to weak Ni-C $\pi$ bonds, endohedral Ni-atoms can easily move on the tube wall.

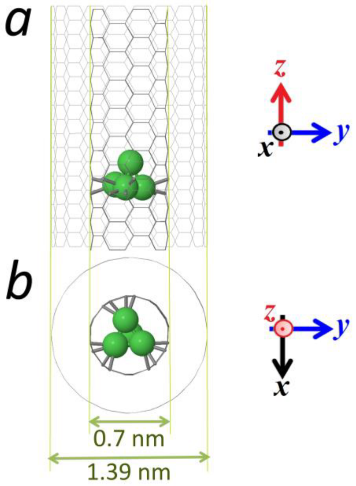

Figure 6.1: Front (a) and top view (b) of Ni-containing (5,5)@(10,10) double-walled carbon nanotubes (DWNTs). In sake of clarity, carbon atoms in DWNT are not shown: light and dark grey wireframes are outer and inner walls of DWNT, respectively. Ni atoms are in green color.

The simulated system is initially equilibrated at the desired temperature applying the Berendsen thermostat,[84] in the NpT ensemble. Subsequently, the Bussi thermostat[104] is used to control the temperature in the canonical NVT simulations. During the simulations, the chosen growth species, i.e., $C_2$, $C_2H$ and $C_2H_2$ are inserted in the inner tube (see Fig. 6.2, first column) with an interval of 25 ps and 250 ps at high (1700 K) and low (500 K) temperatures, respectively. In general, the tube diameters and growth temperatures are chosen according to theoretical suggestions and experimental findings.[175]

All DFT calculations are carried out using the VASP software.[95,96] All optimizations are carried out in the generalized gradient approximation (GGA), employing the revised Perdew-Burke-Ernzerhof (RPBE) functional.[100] All calculations employ the projector augmented wave method (PAW),[78,79] Gaussian smearing,[105,106] and a $\Gamma$-centered (1 x 1 x 1) k-point mesh, with supercells of size (20 x 20 x 20) Å. We employ spin polarization and no symmetry constraints. The energy cutoff is set to 400 eV and the energy convergence is set to $1 \times 10^{-4}$ eV. While the van der Waals corrections are not included in DFT calculations, test calculations including van der Waals interactions (using the Perdew-Burke-Ernzerhof (PBE) functional[73,176] and the Tkatchenko-Scheffler method[177]) indicate that the effect is negligible.

## 6.3 Results and discussion

The nucleation and growth steps of Ni-catalyzed endohedral carbyne from carbon ($C_x$) and hydrocarbon ($C_xH_y$) species are depicted in Figure 6.2. The simulations show that the sticking probability and the adsorption energies of new-inserted feedstock on the metal cluster inversely depend on the ratio of $N_H/N_C$. The adsorption energies are seen to decrease with increasing $N_H/N_C$ ratio in the feedstock. While the absolute value of the adsorption energies in DFT and MD differ by a factor of almost 2 (-3.68, -2.88 eV and -1.36 eV for $C_2$, $C_2H$ and $C_2H_2$, respectively, in MD, vs. -6.43 eV, -5.14 eV and -1.91 eV for DFT), the trend is maintained.

When the inserted molecule impinges on the metal nanocluster either (1) it connects to another adsorbed molecule or (2) it gradually loses its H atoms at the high or low feedstock pressure (flux) conditions, respectively. In the first case (dimerization), the adsorbed feedstocks molecules directly associate on the nanocluster, prior to breaking their C-H bonds, as is demonstrated in Figure 6.3. MD-NEB calculations[178] show that the formation of initial carbon chains from the feedstock dimerization requires association activation barriers of about 0.1 eV, 0.26 eV and 0.3 eV for $C_2$, $C_2H$ and $C_2H_2$, respectively.

In the second case (dehydrogenation), C-H bonds of the adsorbed molecule are gradually broken. In particular, in the case of acetylene ($C_2H_2$), the dissociation of the adsorbed feedstock occurs through step-wise dehydrogenation,[171] i.e., $C_2H_2 \Rightarrow C_2H \Rightarrow C_2$. While the C-C bonds break before C-H bonds on a flat Ni(111) surface, the presence of steps on the surface lowers the activation barrier for C-H bond cleavage.[179] Our Ni nanoparticle behaves like the stepped surface rather than the flat surface and it thus preferably breaks C-H bond instead of the C-C bond. As acetylene chemisorbs, its two C-C $\pi$ bonds can each be broken to form Ni-C $\sigma$ bonds (without fragmenting) to the nickel cluster. In the case that the molecule connects to a single Ni atom, however, one $\pi$ bond remains

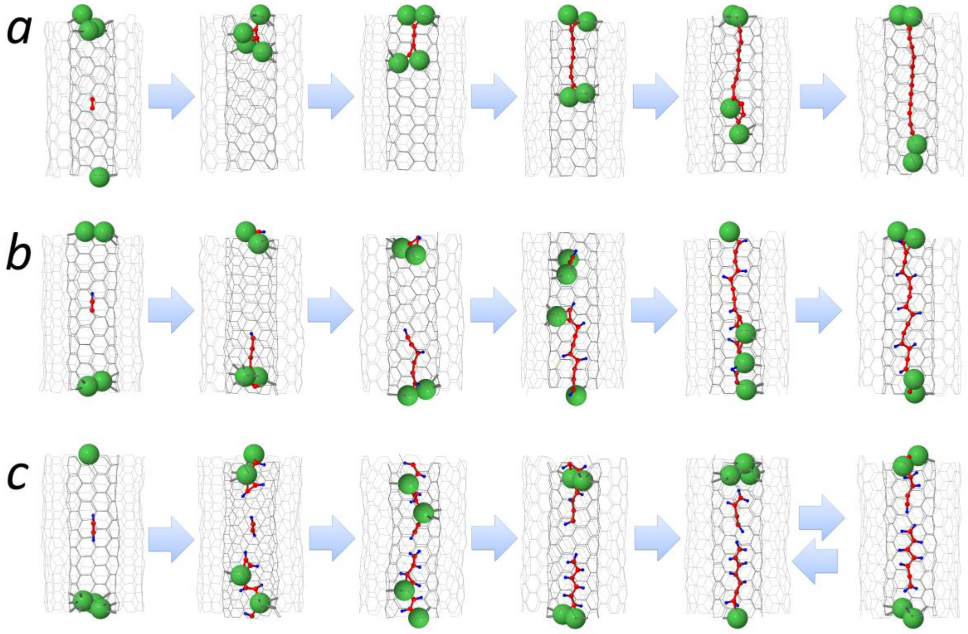

Figure 6.2: Ni-assisted carbyne nucleation and growth in a (5,5)@(10,10) tube from $C_2$ (a), $C_2H$ (b) and $C_2H_2$ (c) precursors. Inserted C and H atoms are highlighted in red and blue colors, respectively.

such that a double C-C bond is retained (e.g., see Fig. 6.2c, frame 2). In moderate pressure cases, dehydrogenation and dimerization can simultaneously occur. In all cases, consecutive carbon (with or without hydrogen) connections eventually initiate the formation of the incipient carbon chain (Fig. 6.2, second and third columns). The total energy of the carbon chain gradually decreases when the carbon concentration increases in the carbon chain. In particular, the change in the system energy per C addition is -6.42 eV, which is very close to the DFT values ranging between -5.77 eV and -7.67 eV for finite carbyne.[55,63,180] In the $C_x$ case, the continuous extension of the chain length induces the nanocluster to split into two smaller fragments, which bind respectively at both ends of the carbon chain (see Fig. 6.2 a, frame 3). The termination by Ni atoms as well as van der Waals interaction with the inner tube facilitates the carbyne growth. While such end-terminations preferable occur, we do not find the carbon chain is embedded into the cluster during the simulations.[181] Due to the Ni-termination of both ends, the undesired connection of the carbyne with the tube wall does not occur. When a single Ni atom is used as a catalyst, however, the interaction probability of the catalyst-free end of the carbyne with the tube wall significantly increases. Similar experimental observations were reported by Kano et

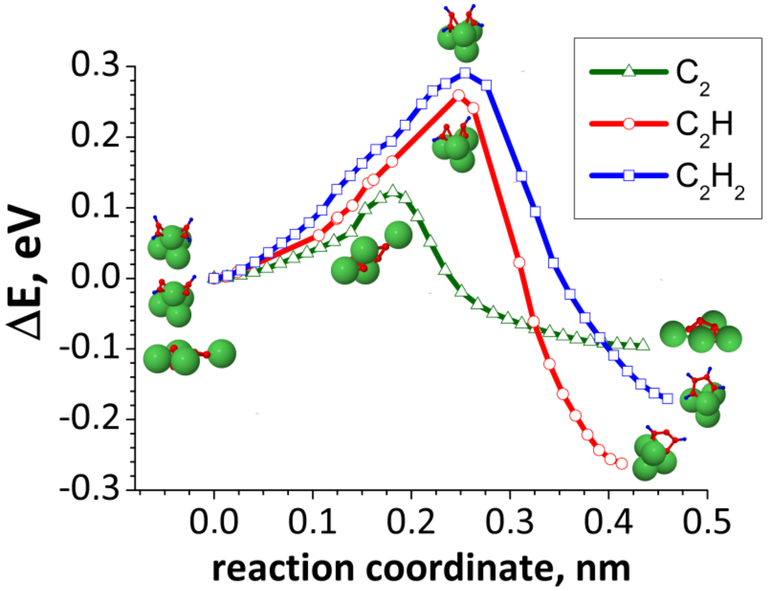

Figure 6.3: Association/dissociation steps and activation barriers in the onset of Ni-assisted nucleation of carbon chain from $C_2$ (green line with open triangles), $C_2H$ (red line with open circles) and $C_2H_2$ (blue line with open squares) feedstocks.

al., i.e., when one Pt atom connects to one end of the obtained carbon chain on a graphene flake, its Pt-free end becomes very unstable.[167] Consequently, chain-tube connections may result in a considerable reduction of the carbyne growth and defect creation in the host tube.[164] While the termination of both ends of the carbyne chain is required in the growth from $C_x$ growth species, the carbyne ends are devoid of such chain-tube influence during the growth from hydrocarbon ($C_xH_y$) feedstocks. Namely, the catalyst-free carbyne tail is quickly terminated by a H atom and undesirable reactions are thus prevented (Fig. 6.2 b and c, second and third columns), indicating that in this case the single Ni atom could also be applied as a catalyst in the growth process.

The overall results indicate that catalyst and hydrogen have opposite effects during the chain nucleation and growth. Namely, the catalyst facilitates the formation of C-C connections and thus enhances the chain elongation. In contrast, hydrogen quickly blocks the chain tail and thus delays or prevents continued chain growth. In the $Ni_n$ cluster case, both catalyst and hydrogen atoms can move along the growing chain as well. Due to this phenomenon, the catalyst atom is seen to bind to the tail of the chain terminated by H and stimulates the chain to grow again (Fig. 6.2 b, third, fourth and fifth columns). Consequently, the obtained carbon chains can be partially or fully hydrogenated and terminated by nickel and/or hydrogen atoms.

In the growth processes, we find several types of carbon chains, viz., polyyne, cumulene and polyene chains[182] with complete or partial termination by metal or hydrogen atom(s), as demonstrated in Fig. 6.4 a.

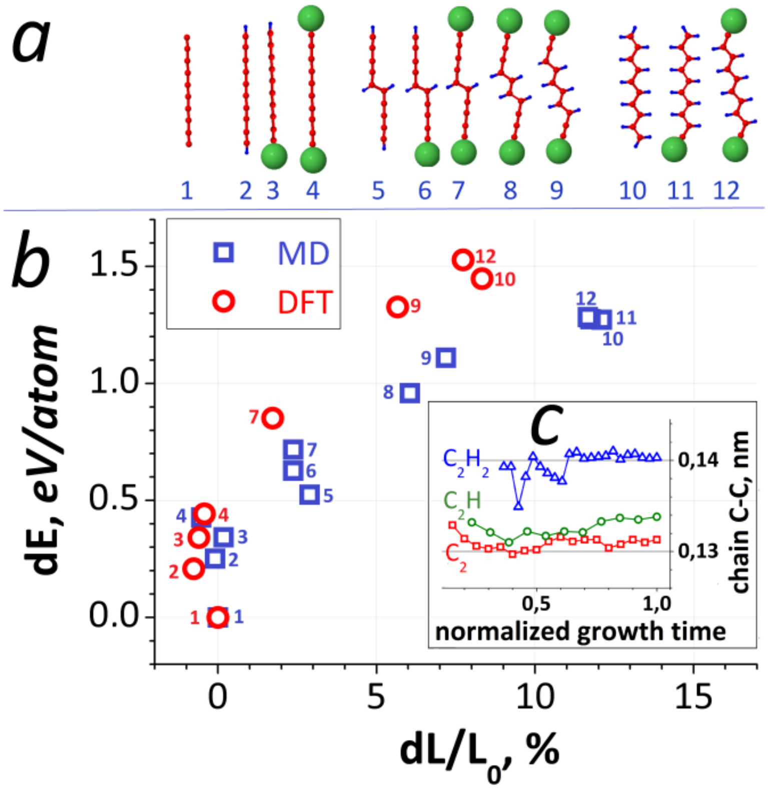

Figure 6.4: (a) Possible chain structures in the catalyzed growth; (b) Dependence of the energy change on the relative extension of chain length; (c) Average C-C bond length during the growth from $C_2$, $C_2H$ and $C_2H_2$ feedstocks.

Every model structure contains 10 C atoms. The aforementioned simulation results indicate in the case of $C_2$ feedstock that the obtained metal-terminated chain is cumulene-like (...=C=C=C=...) (see structure 4 in Fig. 6.4 a) with a bond distance (r) of about 0.13 nm (see $C_2$ in Fig. 6.4 c), which is very close to the experimental value (0.131 nm) for the C-C bond length in a metalated carbyne.[168] Normally, carbyne favours a polyyne structure (...-C≡C-C≡C-...) with C-C bond length alternation (BLA= $|r_1 - r_2|$) due to the Peierls instability. However, zero-point atomic vibrations eliminate such bond alternation making the cumulene $C_n$ chain a stable carbyne structure as well.[183] According to DFT calculations, the energy difference between polyyne and cumulene structures is 2 meV per carbon.[55] At absolute zero, therefore, the carbyne chain is polyyne-like, e.g., in our MD calculations the BLA is 14 pm ($r_1/r_2$ = 0.12/0.134). While this value is higher than our DFT value of 3 pm ($r_1/r_2$ = 0.128/0.131), it is in close agreement with the experimental value, i.e., BLA = 10 pm ($r_1/r_2$ = 0.123/0.133). At non-zero temperature, the BLA tends to zero due to the temperature-dependent chain fluctuations. In addition, such polyyne-cumulene transitions occur due to changing H-termination to $H_2$-termination[182] or due to the elongation of the chain length.[183] The length of the carbon chain relatively extends depending on the degree of hydrogenation of the chain, i.e., the average C-C bond in the chains for the $C_2$, $C_2H$ and $C_2H_2$ cases are 0.13 nm, 0.134 nm and 0.14 nm, respectively (Fig. 6.4 c). Also, the connection of the catalyst atom(s) or/and H atom(s) to the carbon chain can affect both its length and stability. While the length of Ni or H-terminated carbyne structures does not alter significantly, their relative potential energy decreases somewhat (see 1-4 in Fig. 6.4 b). Note that Ni atoms have the positive partial charges (oxidation state of Ni is maximum +2) and consequently the neighboring C atoms have negative partial charges due to partially ionic character of the Ni-C bond. The total charge of the structures is zero in both MD and DFT calculations. On the other hand, both length and stability of hydrogenated carbon chains terminated by either Ni/Ni (structures 4, 7-9, 12 in Fig. 6.4 a) or Ni/H (structures 3, 6, 11 in Fig. 6.4 a) or H/H (structures 2, 5, 10 in Fig. 6.4 a) increase by increasing the H concentration in the chain (see 5-12 in Fig. 6.4 b). Also, consecutive H addition leads the transformation of the chain structure from a "linear" cumulene/polyyne allotrope to a "zigzag" polyene structure.[182] Such additions do not only alter the morphology of the structures, they can change the electronic property of the obtained carbon chains as well.

Fig. 6.5 a shows the calculated density of states (DOS) from -5.0 eV to 5.0 eV, for four carbon chains, i.e., structures 1, 4, 7 and 12 from Fig. 6.4 a. The figure shows that different structures have different gap. As our carbyne structure is calculated as a non-periodic structure, the DOS looks different from other works,[183,184] where only one (large) band gap (around 2.20 eV) can be observed for those periodic carbyne structures. However, our gap values are close to ab-initio calculation results for confined carbon chains.[56,170] The gap widths for each structure are shown separately in Fig. 6.5 b. The figures indicate that the most prominent gap (1.25 eV) appears in case of a finite carbyne (structure 1). When the ends of the carbyne chain are terminated by Ni atoms (structure 4), this prominent gap considerably decreases to 0.69 eV (-45%). Subsequently, this gap decreases further when H atoms are added along the carbyne chain. In particular, maximum gap widths for Ni-terminated carbyne with 2 H atoms (structure 7) and Ni-terminated carbyne with 8 H atoms (structure 12) are 0.62 eV (-50%) and 0.16 eV (-88%), respectively. Indeed, Fig. 6.5 demonstrates that the overall gap widths significantly decrease when H atoms are added along the

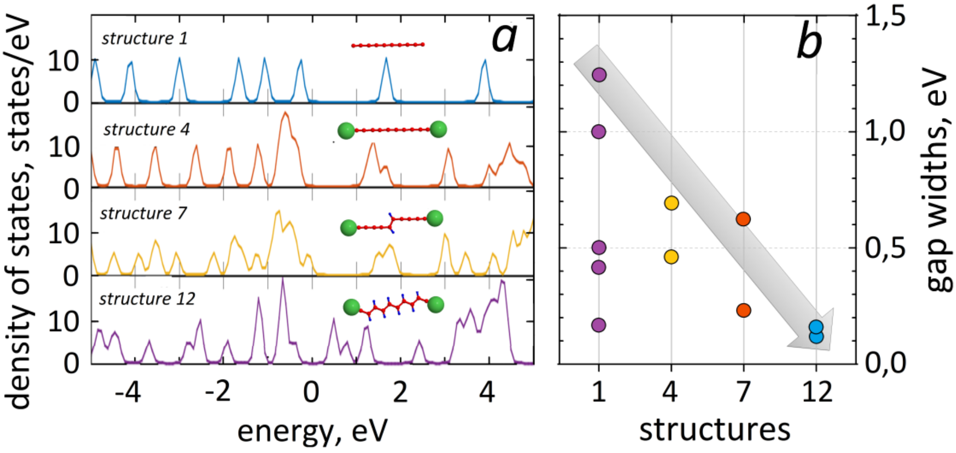

Figure 6.5: (a) Density of states (DOS) and (b) gap dispersion in DOS for various carbon chains.

Ni-terminated carbyne chain, as the dispersion moves towards smaller values.

## 6.4 Conclusion

We study the Ni-catalyzed growth of carbyne inside a double-walled carbon nanotube from carbon and hydrocarbon feedstocks using MD simulations and DFT calculations. We find that a confined long carbyne can be grown from carbon species assisted by Ni as a catalyst. However, in the case of growth from hydrocarbon species, the carbyne chain growth can be hindered by the H addition. Competition between the metal and hydrogen results in various Ni or H-terminated carbon chains with varying degrees of hydrogenation in the tube. The length and stability of the grown chains are also dependent on the type of chain termination and the degree of hydrogenation. We also find that the band gap in metal-terminated carbyne is significantly decreased when H atoms adsorbed along the chain. The overall simulation/calculation results are in agreement with available experimental and theoretical evidences and strongly indicate that the formation of finite carbyne structure with controllable electronic properties is possible.

# 7 Conclusions and outlook

In this thesis, carbon nanotubes and carbyne were studied because of their promise for opto-electronic applications. To enable their use in these applications, their electric properties, and thus their structural properties, must be controlled. Hence, tuning their respective growth processes, in which the structures of these materials are defined, is of paramount importance. How to tune these growth processes is still not entirely known. Therefore, using computational methods, we studied properties with an important influence in the growth processes of CNTs and carbyne.

## 7.1 Carbon nanotubes

The driving factor behind chirality formation in CNT growth is, as we mentioned, still elusive. Both the thermodynamic stability of the CNT-NP complex[37, 44, 45] and kinetic processes have been suggested as a possible driving factor.

We investigated the thermodynamic stability of the CNT-NP catalyst complex using the adhesion energy of a CNT attached to a NP. First of all, we did a study on potential catalysts for chirality selective carbon nanotube growth. Stabilities of NiFe, NiGa and FeGa nanoparticles with various compositions and atom distributions were computed through DFT calculations. Nanoparticles with more Fe in the core and more Ga on the surface were more stable. This trend is most obvious for FeGa. The alloy and the atom distribution determine the composition that will have the highest stability. Furthermore, the influence of interstitial carbons on NiFe stabilities was investigated through both DFT and BOMD calculations. The stability of a NiFe nanoparticle would increase with the number of carbon interstitials. In general, the trend in stability over atom distributions depends somewhat on the carbon content, but the overall trend of nanoparticles with more Fe in the core being more stable is maintained, as is the trend that 25/75 is the most stable composition for NiFe nanoparticles. The results of this study were then used in our calculations on the CNT-metal adhesion systems.

Then, adhesion systems of various CNTs on Ni, Fe, and FeNi NPs were modelled through DFT calculations. The influence of carbon interstitials was analysed and was deemed insignificant. Using a fitting procedure on the DFT results, the imperfect NP-SWCNT interface was compensated for. Whereas the DFT results only exhibited weak trends due to the limitations of the systems used, the fits exhibited trends consistent with previous experimental work by Chiang et al. Depending on the FeNi composition, no chiral preference or a preference towards armchair/zigzag chiralities could be observed. No significant preference was observed in the case of pure metal NPs and $Fe_{0.5}Ni_{0.5}$ NPs, but zigzag and armchair chiralities were favoured on the other hand by $Fe_{0.75}Ni_{0.25}$ and $Fe_{0.25}Ni_{0.75}$ NPs respectively.

Finally, we also explored a kinetic process, namely defect healing. Many underlying kinetic processes exist in CNT growth, and yet the process of defect healing is particularly interesting. Defects growing into the CNT can cause the chirality to change, something that is not desirable for chirality selective growth. Therefore, the ability of the catalyst to heal defects on the CNT-NP interface is deemed an important factor to control the chirality during growth.[53] In this thesis, we focused on the energies of defects in CNTs adhered to a Ni catalyst, to investigate whether healing the defect will be energetically favoured or not. Consistent with previous studies, we demonstrated that the metal catalyst plays a crucial role in defect healing in CNTs. We established that the structure of the catalyst NP has an impact the healing of the defect. The presence of metal atoms at certain locations on the NP-CNT interface being paramount for defect healing is possibly the explanation for this. The chirality resulting from the growth is influenced by whether a defect heals or not, and consequently, also by the structure of the NP. Further research is imperative to establish whether these results are reproducible for other CNT chiralities and other metal catalysts.

Our overall results suggest that various factors are at play during CNT growth and that one driving factor cannot be found (yet). Future research is of the utmost importance to confirm whether these results hold for all types of metallic catalysts and all CNTs.

## 7.2 Carbyne

Long linear carbyne chains have been grown inside DWCNTs. This endohedral carbyne synthesis can be aided by embedding a metal catalyst in the DWCNT. When the precursor adsorbs on the catalyst, precursor bond breaking and C-C bond formation can be facilitated, owing to the lowering of activation energy barriers of those reactions by the metal. We examined the roles of the catalyst and of the precursor in endohedral carbyne growth.

The Ni-catalyzed growth of carbyne inside a double-walled carbon nanotube from carbon and hydrocarbon feedstocks was studied using MD simulations and DFT calculations. It was found that, when growing from carbon species, a confined long carbyne can be grown assisted by Ni as a catalyst. However, when growing from hydrocarbon species, the carbyne chain growth can be hindered by the H addition. Competition between the metal and hydrogen resulted in various Ni- or H-terminated carbon chains with varying degrees of hydrogenation in the tube. The type of chain termination and the degree of hydrogenation both influence the length and stability of the grown chains. We also found that the band gap in metal-terminated carbyne is significantly decreased when H atoms are adsorbed along the chain. Besides that the overall computational results were in agreement with available experimental and theoretical results, they also indicate that the formation of finite carbyne structures with selective electric properties is possible.

## 7.3 Outlook

Based on our results, we here discuss some possibilities for future research towards chirality selective CNT growth and carbyne growth.

This work provides a step in the right direction of narrowing the chirality distribution of CNTs. However, further investigations are necessary to improve the performance of metallic catalysts in order to achieve complete chirality selective CNT growth.

Our results in chapters 4 and 5 confirm that a metal catalyst has a significant impact on the chirality of the CNT. However, neither of these processes can be proven to be *the* driving force for chirality selective CNT growth. This raises the question whether one such driving force can be found. Moreover, an important aspect to be considered here are the final adhesion energy results. We discussed the trend in adhesion energy as a function of chirality, but we also found that such a trend was only present once the DFT results were fitted with equation 4.3. This gives rise to the assumption that the adhesion energy will undoubtedly have a significant influence on the chirality formation, but that it cannot be considered *the* driving force. We contend that other factors must be at play too, for example, the defect healing process. The question remains whether there are even more factors working on chirality formation, and what the relative importance of all factors will be.

Besides the driving forces for chirality formation, future research could also address what type of catalyst is most suitable. Our research into NiFe and other works in the field of bimetallic catalysts suggest that bimetallic catalysts remain indeed promising. However, many options remain, such as Ga-based (chapter 3) and W-based alloys,[46] and further study is required to find optimal alloys. As mentioned in section 1.2.2, suitable catalysts must obey the Goldilocks principle. Furthermore, an optimum must be found in their influences on the driving forces for chirality formation. Optimizing these catalysts is thus imperative to obtain narrow chirality distributions.

Carbyne is a material with promise in the field of electronics. It has some very interesting properties, such as electric properties that are tunable, as we showed in chapter 6. Nevertheless, the field of carbyne is still wide open. There are still many questions regarding both the growth process of carbyne and its implementation in electronics. Hence, in both fields there are still many opportunities for improvement. The electric properties of carbyne could be explored further: are there other ways to tune them, to what extend can they be tuned, etc. Other possible precursors and their potential influence on the tuning could be investigated. The influence of tuning of carbyne's electric properties on its use in electronic applications is yet another domain that should be addressed. Both carbon nanomaterials have enormous potential for a large number of electronic applications. Nonetheless, limitations in their respective growth processes have so far prevented these materials to live up to their promise. For this reason, it is imperative that the growth processes of these materials keep receiving attention. Both computational and experimental work is needed for the progress of the field, with a view to finally achieving real electronic applications with those carbon nanomaterials.

# Academic CV

# List of publications

## Related to this thesis

1. **Charlotte Vets**, Daniel Hedman, J. Andreas Larsson and Erik C. Neyts. Tuning single-walled carbon nanotube adhesion energies using bimetallic catalysts. **In preparation**.
2. Umedjon Khalilov, **Charlotte Vets**, and Erik C. Neyts. Catalyzed growth of encapsulated carbyne. *Carbon* **153**, 1-5 (2019).
3. **Charlotte Vets** and Erik C. Neyts. Stabilities of bimetallic nanoparticles for chirality-selective carbon nanotube growth and the effect of carbon interstitials. *J. Phys. Chem. C* **121**, 15430-15436 (2017).

## Not included in this thesis

1. Umedjon Khalilov, **Charlotte Vets**, and Erik C. Neyts. Molecular evidence for feedstock-dependent nucleation mechanism of CNTs. *Nanoscale Horizons* **4**, 674-682 (2019).

# List of presentations

## Conference contributions

1. Charlotte Vets, Daniel Hedman, J. Andreas Larsson, and Erik C. Neyts. The carbon nanotube-metal adsorption energy: key to chirality selective growth? *30th International Conference on Diamond & Carbon Materials 2019*, Seville, Spain, September 8-12, 2019. **Oral presentation.**

2. Charlotte Vets, Daniel Hedman, J. Andreas Larsson, and Erik C. Neyts. The CNT-metal adsorption energy: key to chirality selective growth? *14th Symposium on Computational Challenges in Two-Dimensional Materials and Nanotubes*, Würzburg, Germany, July 22-23, 2019. **Oral presentation.**

3. Charlotte Vets and Erik C. Neyts. Thermodynamic screening of bimetallic nanoparticles for chirality-selective carbon nanotube growth. *iPlasmaNano-VIII - 8th International Conference on Plasma Nanoscience*, Antwerp, Belgium, July 2-6, 2017. **Poster presentation.**

4. Charlotte Vets and Erik C. Neyts. Bimetallic nanoparticles: computational screening for chirality-selective carbon nanotube growth. *VSC Users Day*, Brussels, Belgium, June 2, 2017. **Poster and oral flash presentation.**

5. Charlotte Vets and Erik C. Neyts. Computational study of chirality controlled growth of carbon nanotubes on bimetallic catalysts. *Chemical Research in Flanders*, Blankenberge, Belgium, October 24-26, 2016. **Poster presentation.**

6. Charlotte Vets and Erik C. Neyts. Thermodynamic screening of bimetallic catalysts for chirality controlled growth of CNTs. *11th Symposium on Computational Challenges and Tools for Nanotubes*, Vienna, Austria, August 13, 2016. **Oral presentation.**

7. Charlotte Vets and Erik C. Neyts. Thermodynamic screening of bimetallic catalysts for chirality controlled growth of CNTs. *17th International Conference on the Science and Applications of Nanotubes and low-dimensional materials*, Vienna, Austria, August 7-12, 2016. **Poster presentation.**

## Science communication

1. Op weg naar nog betere smartphones. *Mini-lecture for children, Dag van de Wetenschap*, Antwerp, Belgium, November 24, 2019. **Oral presentation.**
2. Je smartphone minder vaak opladen dankzij nanobuisjes van koolstof. *Wetenschap Uitgedokterd*, Antwerp, Belgium, June 19, 2019. **Internet movie clip:** https://www.sciencefiguredout.be/charging-your-smartphone-less-frequently-thanks-carbon-nanotubes.
3. Hoe het materiaal in je potlood helpt om energie te besparen. *Wetenschapsbattle 2019*, Antwerp, Belgium, March 19, 2019. **Oral presentation.**
4. Nanobuisjes van koolstof: het hindernissenparcours naar betere elektronica. *PRESS>SPEAK 2019 presentation contest (University of Antwerp)*, Antwerp, Belgium, February 14, 2019. **Oral presentation.**

# Awards and grants

## Awards

1. **3$^{rd}$ place** in *PRESS>SPEAK 2017 writing contest (University of Antwerp)* for the science communication article "Op weg naar een betere smartphone", Antwerp, Belgium, March 19, 2017.

## Grants

1. **FWO travel grant** for a research visit to the Luleå University of Technology in Luleå, Sweden, March - May 2018.
2. **Tier-1 project grant** for computing time on the Tier-1 infrastructure of the VSC, July - December 2017.
3. **Tier-1 project grant** for computing time on the Tier-1 infrastructure of the VSC, July - December 2016.
4. **FWO PhD fellowship strategic basic research** (2 + 2 years), January 2016 - December 2019.

# A Stabilities of bimetallic nanoparticles for chirality-selective carbon nanotube growth and the effect of carbon interstitials: Supplementary information

## A.1 Nanoparticles visualization

Pictures of NiFe nanoparticles in 25/75 composition to visualize the five different atom distributions were included in figure A.1. In figure A.2, visualizations are given for interstitials sites in the cuboctahedra and carbon atoms in these sites. In figures A.2a and A.2b octahedral and tetrahedral sites are shown, respectively. In figure A.2c, the octahedral site is filled by a carbon atom, and in figure A.2d, some surface Fe atoms were removed to show this more clearly.

## A.2 Enthalpy Change of Solution of NiFe Nanoparticles with Carbon Interstitials

The enthalpy change of solution of NiFe nanoparticles with carbon interstitials was calculated to further investigate the nanoparticles' stabilities. This $\Delta H_{sol}$ is calculated as the energy difference of two nanoparticles upon adding one carbon atom:

$$\Delta H_{sol} = E_{Ni_m Fe_n C_k} - E_{Ni_m Fe_n C_{k-1}} - E_C \tag{A.1}$$

where $E_{Ni_m Fe_n C_k}$ and $E_{Ni_m Fe_n C_{k-1}}$ are the total energies of NiFe nanoparticles with $k$ and $k-1$ carbon atoms respectively, and $E_C$ is the total energy of a single carbon atom. This enthalpy change of solution was calculated for all NiFe nanoparticles, with the number of carbon interstitials ranging from 1 to 8. No trend in the enthalpy change was found. In the former results, new carbon atoms were added randomly, but in order to obtain a trend, it was also attempted to add a new carbon atom in the octahedral position as far away as possible from the carbon atoms already present. These enthalpy changes of solution were

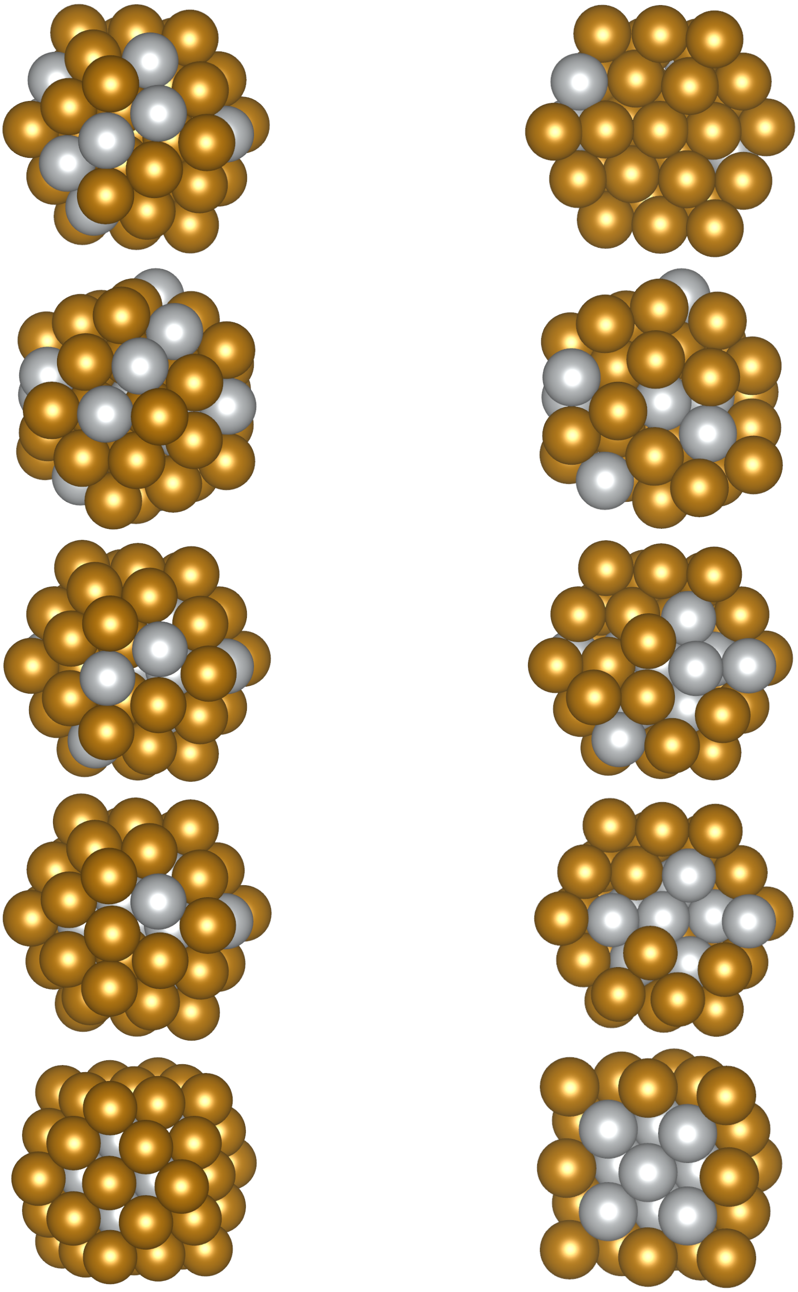

Figure A.1: NiFe nanoparticles with 25/75 compositions are visualized. The silver-colored atoms are Ni, the gold-colored atoms are Fe. The top line presents the nanoparticle with a full Fe core, the second line with 25% of the core being Ni, the third with 50%, the fourth with 75%, and the last line with a full Ni core. The left column shows the full nanoparticles, the right column their cross-sections.

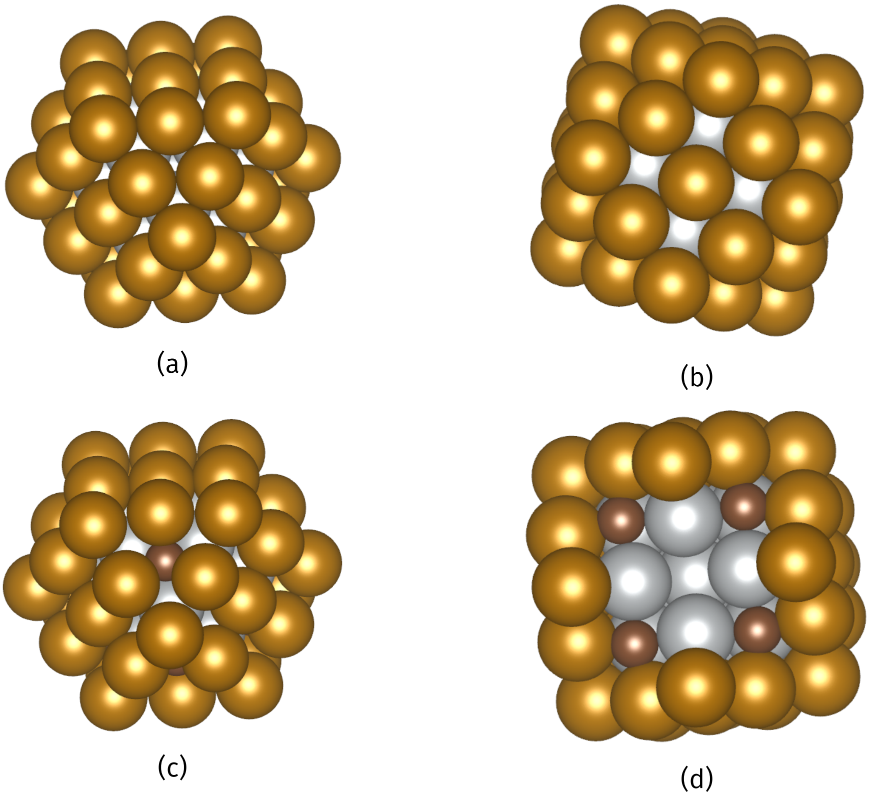

Figure A.2: A 25/75 NiFe nanoparticle with full Ni core and 8 interstitial carbons is shown. The silver-colored atoms are Ni, the gold-colored atoms are Fe, and the brown atoms are C. Carbon atoms are included in octahedral sites (a and c), as tetrahedral sites (b) are too small to accommodate carbons. Figure (d) shows carbons in octahedral sites of the nanoparticle. (Some Fe atoms at the surface were removed for the sake of clarity.)

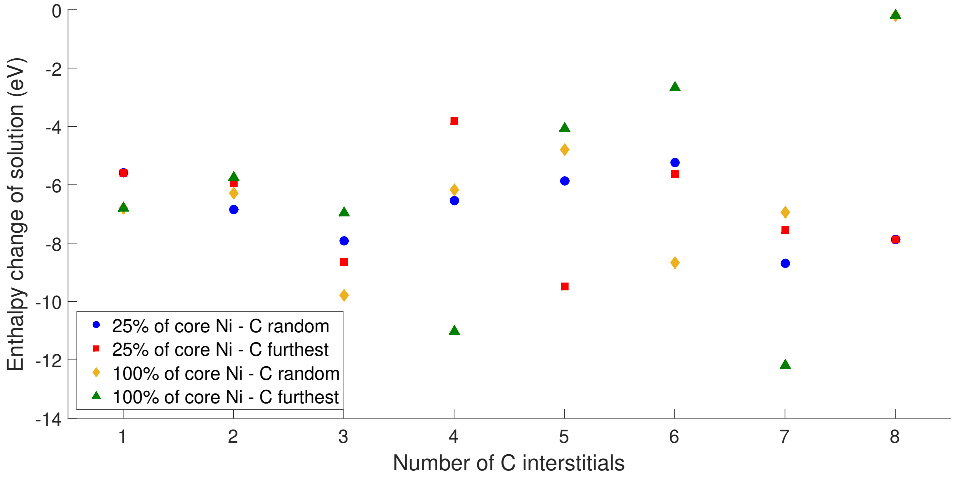

Figure A.3: Enthalpy change of solution for selected nanoparticles with interstitial C.

calculated for two NiFe nanoparticles with 25/75 composition: one with 25% of the core being Ni and the other with a full Ni core. A comparison of the results obtained with both manners to add carbon atoms is given in figure A.3. Unfortunately in neither of these cases, a trend in enthalpy change of solution can be observed.

# B Computational resources

In this thesis, various computational infrastructures were used. They are discussed in section B.1. Computing times for all the studied systems were very diverse, and we thus describe those briefly in section B.2. Finally, benchmarking of some calculations was conducted in the framework of Tier-1 project applications. The benchmarking tests are discussed in section B.3.

## B.1 Computational infrastructure

Three types of infrastructure were used. Firstly, for most of the calculations the Tier-2 infrastructure of the University of Antwerp was used. This infrastructure is also part of the Vlaams Supercomputer Centrum (VSC). Both of the University of Antwerp's current clusters, Hopper and Leibniz, were used, as well as the old cluster, Turing.[185] Leibniz consists of 152 compute nodes that each have two 14-core Intel Xeon E5-2680v4 Broadwell generation CPUs connected through an EDR InfiniBand network. Most of the nodes have 128 GB RAM. Hopper consists of 168 compute nodes that each have two 10-core Intel Xeon E5-2680v2 Ivy Bridge generation CPUs connected through a FDR10 InfiniBand network. Most of the nodes have 64 GB RAM.

Tier-2 infrastructure typically reaches ten to twenty teraflops, so then, also Tier-1 infrastructure, which reaches 100 to 200 teraflops, was used for the more computationally intensive systems. To use the Tier-1 infrastructure of the VSC, a project grant must be applied for. Two such project grants were received, one on the old Tier-1 cluster located at University of Gent, Muk, and one on the new Tier-1 cluster located at KULeuven, BrENIAC.[186] BrENIAC has 580 Broadwell nodes and 408 Skylake nodes. We used the Broadwell nodes, that each have two 14-core Intel Xeon E5-2680v4 CPUs connected through an EDR Infiniband network. Those nodes have 128 GB RAM.

Lastly, for some calculations also the local cluster of our research group, fistUA, was used.

The Tier-2 infrastructure was used for most calculations, since it is not computationally feasible to run VASP for our systems on a smaller cluster. Tier-1 infrastructure was mainly used for calculations on adhesion systems because of their size, whereas the fistUA cluster was used for the defect healing simulations, as the simulations in ReaxFF did not require as much computational power.

## B.2 Computing time

Obviously, computing times were very different for different systems, since their sizes and composing elements are not the same. DFT optimizations of CNT systems were finished in 30 to 60 minutes, using two nodes on the Tier-2 cluster Hopper. These calculations are quite fast owing to the fact that only simple atoms, i.e. C and H, are present. DFT optimizations of metal NPs were much more computationally expensive, and the computing time highly depends on the type of elements in the NP. For example, using one node on Hopper, the optimization of a NiFe NP can take about 12 hours, whereas the optimization of a NiGa NP can take about 92 hours. On the other hand, when C interstitials are added to the NiFe NP, the computing time can increase steeply. To illustrate this, we look at the optmization of a NiFe NP with seven C interstitials: the computing time here is about 157 hours, and two nodes instead of one were used.
BOMD calculations were mainly done on the Tier-1 infrastructure. On Muk, a BOMD calculation with zero C interstitials took about 75 hours using 3 nodes. On BrENIAC, a BOMD calculation with zero C interstitials took about 50 hours using 2 nodes, wheras a calculation with eight C interstitials took about 65 hours using the same amount of nodes.
Initial DFT calculations of adhesion systems were done on the Tier-1 infrastructure BrENIAC using 8 nodes. A calculation when zero C interstitials are present in the NP typically took between 10 and 20 hours, whereas calculations with eight C interstitials in the NP took about 30 hours. DFT calculations of adhesion systems when we added a magnetic moment in the NP were done on the Tier-2 infrastructure Leibniz using 5 nodes. Only calculations without C interstitials in the NP were done in this case, and they took between 20 and 30 hours. However, in some cases the computing time was much longer, i.e. about 60 hours.
Defect healing simulations were done on the fistUA infrastructure. We did not run ReaxFF in parallel. The computing time was between 30 and 80 hours, depending on the type of defect and on the NP structure.
DFT calculations on carbyne were done on Leibniz, using one node. The number of processors used depended on the system being optimized. First, adsorption calculations for $C_2$, $C_2H$, and $C_2H_2$ on a small Ni cluster took between 30 and 60 minutes, while the optimizations of just the Ni cluster and just the (hydro)carbons took about five minutes. DFT optimizations of various carbyne chains, as depicted in figure 6.4, typically took between 10 and 40 minutes, although for some chains the computing time went up to six hours. DFT self-consistent energy calculations to obtain the DOS only took a couple of minutes.

## B.3 Benchmarking for Tier-1

In a Tier-1 project application, it is required to include scaling tests conducted with the software to be used. The system used for the scaling tests should be comparable to the system that will actually be simulated when the Tier-1 project is granted. I did this benchmarking both on Muk and on BrENIAC. Table B.1 and figure B.1 demonstrate the scaling tests on Muk, and table B.2 and figure B.2 demonstrate the scaling tests on BrENIAC.

Table B.1: Scaling tests for the relaxation of a hydrogen passivated (15,0) CNT with 120 C atoms and 15 H atoms on Muk.

| Nodes | Number of cores | Absolute timing (days) | Speedup | Efficiency |
|---|---|---|---|---|
| 3 | 48 | 4.383 | 1 | 1 |
| 6 | 96 | 2.425 | 1.81 | 0.904 |
| 12 | 192 | 1.629 | 2.69 | 0.673 |

Table B.2: Scaling tests for the relaxation of a hydrogen passivated (15,0) CNT with 90 C atoms and 30 H atoms on BrENIAC.

| Nodes | Number of cores | Wall clock time (s) | Speedup | Efficiency |
|---|---|---|---|---|
| 1 | 28 | 103500 | 1 | 1 |
| 2 | 56 | 53514 | 1.93 | 0.967 |
| 4 | 112 | 27434 | 3.77 | 0.943 |
| 8 | 224 | 14700 | 7.04 | 0.880 |
| 16 | 448 | 8078 | 12.8 | 0.801 |

Each table shows the number of nodes and the number of cores that were used for the test calculations, and the total computing time of each calculation. From this, the speedup that can be obtained with the Tier-1 system is computed, as well as the efficiency of using more nodes. The speedup is calculated using the following equation:

$$speedup = \frac{t_{comp,init}}{t_{comp,cur}}, \tag{B.1}$$

where $t_{comp,init}$ is the computing time for the calculation with the lowest number of nodes, and $t_{comp,cur}$ is the computing time for the current calculation. The efficiency is then calculated as:

$$efficiency = speedup \times \frac{n_{cores,init}}{n_{cores,cur}}, \tag{B.2}$$

where $n_{cores,init}$ is the number of cores used for the calculation with the lowest number of nodes, and $n_{cores,cur}$ is the number of cores for the current calculation.

The speedup is then plotted as a function of the number of cores. Besides plotting the real speedup, we also plot the ideal speedup, which is linear and equals the number of nodes used for the test calculation divided by the number of nodes used for the calculations with the lowest number of cores. This graphical representation allows to see clearly which would be the optimal number of nodes to be used for that calculation using that software on that Tier-1 system. The scaling test on BrENIAC, for instance, exhibits a speedup that is still close to the ideal one when 8 nodes are used, while the speedup for 16 nodes is significantly below the ideal speedup. This is confirmed by the efficiencies in table B.2. Therefore, we used 8 nodes for our calculations on BrENIAC (see section B.2).

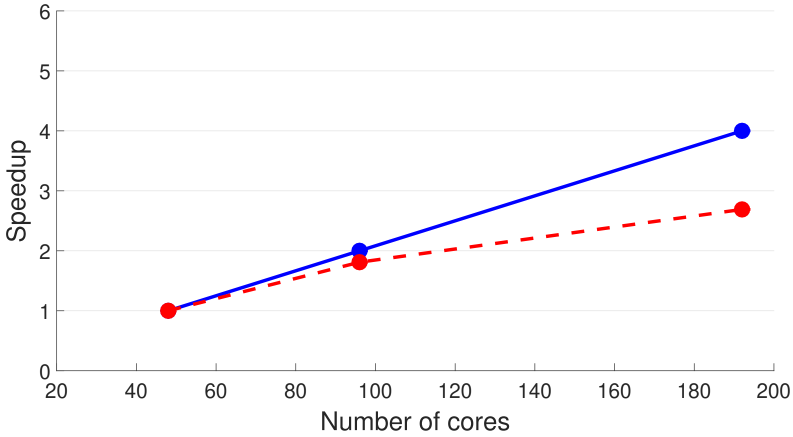

Figure B.1: Scaling tests for the relaxation of a hydrogen passivated (15,0) CNT with 120 C atoms and 15 H atoms on Muk. Ideally, the speedup is linear (blue dots and full line), whereas the real speedup is always lower. In this case the real speedup is given by the red dots and dotted line.

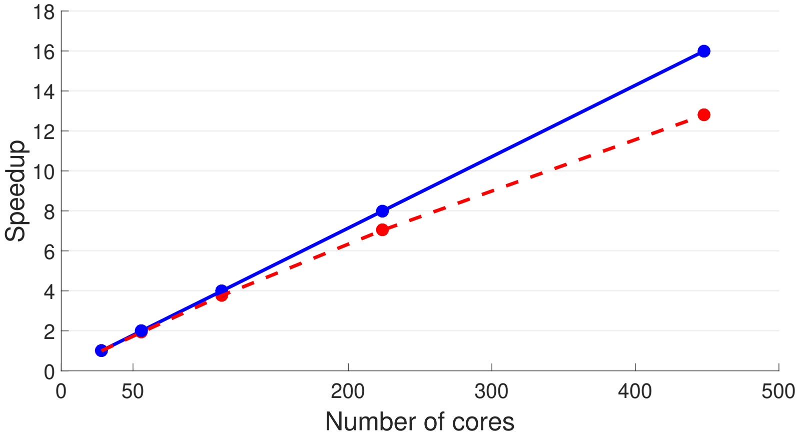

Figure B.2: Scaling tests for the relaxation of a hydrogen passivated (15,0) CNT with 90 C atoms and 30 H atoms on BrENIAC. Ideally, the speedup is linear (blue dots and full line), whereas the real speedup is always lower. In this case the real speedup is given by the red dots and dotted line.

# Bibliography

[1] M. C. Lemme, T. J. Echtermeyer, M. Baus, and H. Kurz. A Graphene Field-Effect Device. *IEEE Electron Device Lett.*, 28(4):282–284, 2007.

[2] A. Das, S. Pisana, B. Chakraborty, S. Piscanec, S. K. Saha, U. V. Waghmare, K. S. Novoselov, H. R. Krishnamurthy, A. K. Geim, A. C. Ferrari, and A. K. Sood. Monitoring dopants by Raman scattering in an electrochemically top-gated graphene transistor. *Nat. Nanotechnol.*, 3:210–215, 2008.

[3] N. S. Sariciftci, D. Braun, C. Zhang, V. I. Srdanov, A. J. Heeger, G. Stucky, and F. Wudl. Semiconducting polymer-buckminsterfullerene heterojunctions: Diodes, photodiodes, and photovoltaic cells. *Appl. Phys. Lett.*, 62:585, 1993.

[4] A. D. Franklin, M. Luisier, S. J. Han, G. Tulevski, C. M. Breslin, L. Gignac, M. S. Lundstrom, and W. Haensch. Sub-10 nm carbon nanotube transistor. *Nano Lett.*, 12(2):758–762, 2012.

[5] N. Patil, A. Lin, J. Zhang, H. Wei, K. Anderson, H. S. P. Wong, and S. Mitra. VMR: VLSI-compatible metallic carbon nanotube removal for imperfection-immune cascaded multi-stage digital logic circuits using carbon nanotube FETs. In *Tech. Dig. - Int. Electron Devices Meet. IEDM*, pages 573–576, Baltimore, Maryland, 2009. Institute of Electrical and Electronics Engineers (IEEE).

[6] H. Li, W. Liu, A. M. Cassell, F. Kreupl, and K. Banerjee. Low-resistivity long-length horizontal carbon nanotube nundles for interconnect applications-Part II: Characterization. *Electron Devices, IEEE Trans.*, 60(9):2870–2876, 2013.

[7] S. Kaur, N. Raravikar, B. A. Helms, R. Prasher, and D. F. Ogletree. Enhanced thermal transport at covalently functionalized carbon nanotube array interfaces. *Nat. Commun.*, 5:141–144, 2014.

[8] T. Someya, J. Small, P. Kim, C. Nuckolls, and J. T. Yardley. Alcohol vapor sensors based on single-walled carbon nanotube field effect transistors. *Nano Lett.*, 3(7):877–881, 2003.

[9] Z. Zanolli, G. Onida, and J. Charlier. Quantum Spin Transport in Carbon Chains. *ACS Nano*, 4(9):5174–5180, 2010.

[10] S. Tongay, R. T. Senger, S. Dag, and S. Ciraci. Ab-initio Electron Transport Calculations of Carbon Based String Structures. *Phys. Rev. Lett.*, 93(13):136404, 2004.

[11] M. Wang and S. Lin. Ballistic Thermal Transport in Carbyne and Cumulene with Micron-Scale Spectral Acoustic Phonon Mean Free Path. *Sci. Rep.*, 5:18122, 2015.

[12] A. K. Geim and K. S. Novoselov. The rise of graphene. *Nat. Mater.*, 6:183–191, 2007.

[13] M. M. J. Treacy, T. W. Ebbesen, and J. M. Gibson. Exceptionally high Young's modulus observed for individual carbon nanotubes. *Nature*, 381:678–680, 1996.

[14] F. Li, H. M. Cheng, S. Bai, G. Su, and M. S. Dresselhaus. Tensile strength of single-walled carbon nanotubes directly measured from their macroscopic ropes. *Appl. Phys. Lett.*, 77(20):3161–3163, 2000.

[15] C. T. White and T. N. Todorov. Carbon nanotubes as long ballistic conductors. *Nature*, 393:240–242, 1998.

[16] H. Dai, A. Javey, E. Pop, D. Mann, W. Kim, and Y. Lu. Electrical transport properties and field effect transistors of carbon nanotubes. *Nano Br. Reports Rev.*, 1(1):1–13, 2006.

[17] E. Pop, D. Mann, Q. Wang, K. Goodson, and H. Dai. Thermal Conductance of an Individual Single-Wall Carbon Nanotube above Room Temperature. *Nano Lett.*, 6(1):96–100, 2006.

[18] F. Silvearv, P. Larsson, S. L. T. Jones, R. Ahuja, and J. A. Larsson. Establishing the most favorable metal-carbon bond strength for carbon nanotube catalysts. *J. Mater. Chem. C*, 3(14):3422–3427, 2015.

[19] C. Singh and W. Song. Carbon nanotube structure, synthesis, and applications. In K. Donaldson, C. Poland, R. Duffin, and J. Bonner, editors, *Toxicol. Carbon Nanotub.*, pages 1–37. Cambridge University Press, Cambridge, 2012.

[20] M. Roberts, Y. W. Jin, J. M. Kim, M. C. LeMieux, S. Barman, and Z. Bao. Self-Sorted, Aligned Nanotube Networks for Thin-Film Transistors. *Science*, 321:101–104, 2008.

[21] G. Zhang, P. Qi, X. Wang, Y. Lu, X. Li, R. Tu, S. Bangsaruntip, D. Mann, L. Zhang, and H. Dai. Selective Etching of Metallic Carbon Nanotubes by Gas-Phase Reaction. *Science*, 314:974–977, 2006.

[22] P. G. Collins, M. S. Arnold, and P. Avouris. Engineering Carbon Nanotubes and Nanotube Circuits Using Electrical Breakdown. *Science*, 292:706–709, 2001.

[23] E. C. Neyts. PECVD growth of carbon nanotubes: from experiment to simulation. *J. Vac. Sci. Technol. B*, 30:030803, 2012.

[24] M.-F. C. Fiawoo, A.-M. Bonnot, H. Amara, C. Bichara, J. Thibault-Pénisson, and A. Loiseau. Evidence of correlation between catalyst particles and the single-wall carbon nanotube diameter: A first step towards chirality control. *Phys. Rev. Lett.*, 108(19):1–5, 2012.

[25] M. He, P. V. Fedotov, A. Chernov, E. D. Obraztsova, H. Jiang, N. Wei, H. Cui, J. Sainio, W. Zhang, H. Jin, M. Karppinen, E. I. Kauppinen, and A. Loiseau. Chiral-selective growth of single-walled carbon nanotubes on Fe-based catalysts using CO as carbon source. *Carbon*, 108:521–528, 2016.

[26] S. Maruyama, R. Kojima, Y. Miyauchi, S. Chiashi, and M. Kohno. Low-temperature synthesis of high-purity single-walled carbon nanotubes from alcohol. *Chem. Phys. Lett.*, 360(3-4):229–234, 2002.

[27] C. Vets and E. Neyts. Stabilities of bimetallic nanoparticles for chirality-selective carbon nanotube growth and the effect of carbon interstitials. *J. Phys. Chem. C*, 121(28):15430–15436, 2017.

[28] E. Neyts, Y. Shibuta, and A. Bogaerts. Bond switching regimes in nickel and nickel-carbon nanoclusters. *Chem. Phys. Lett.*, 488:202–205, 2010.

[29] S. Haghighatpanah, A. Mohsenzadeh, H. Amara, C. Bichara, and K. Bolton. Computational studies of catalyst-free single walled carbon nanotube growth. *J. Chem. Phys.*, 139(5):054308, 2013.

[30] J. R. Sanchez-Valencia, T. Dienel, O. Gröning, I. Shorubalko, A. Mueller, M. Jansen, K. Amsharov, P. Ruffieux, and R. Fasel. Controlled synthesis of single-chirality carbon nanotubes. *Nature*, 512:61–64, 2014.

[31] J. Pang, A. Bachmatiuk, I. Ibrahim, L. Fu, D. Placha, G. S. Martynkova, B. Trzebicka, T. Gemming, J. Eckert, and M. H. Rümmeli. CVD growth of 1D and 2D sp2 carbon nanomaterials. *J. Mater. Sci.*, 51(2):640–667, 2016.

[32] V. Jourdain and C. Bichara. Current understanding of the growth of carbon nanotubes in catalytic chemical vapour deposition. *Carbon*, 58:2–39, 2013.

[33] M. He, Y. Magnin, H. Jiang, H. Amara, E. Kauppinen, A. Loiseau, and C. Bichara. Growth Modes and Chiral Selectivity of Single-Walled Carbon Nanotubes. *Nanoscale*, 10:6744–6750, 2018.

[34] M. Chhowalla, K. B. K. Teo, C. Ducati, N. L. Rupesinghe, G. A. J. Amaratunga, A. C. Ferrari, D. Roy, J. Robertson, and W. I. Milne. Growth process conditions of vertically aligned carbon nanotubes using plasma enhanced chemical vapor deposition. *J. Appl. Phys.*, 90(10):5308–5317, 2001.

[35] V. I. Artyukhov, E. S. Penev, and B. I. Yakobson. Why nanotubes grow chiral. *Nat. Commun.*, 5:4892, 2014.

[36] K. K. K. Koziol, C. Ducati, and A. H. Windle. Carbon nanotubes with catalyst controlled chiral angle. *Chem. Mater.*, 22(17):4904–4911, 2010.

[37] E. J. G. Santos, J. K. Norskov, A. R. Harutyunyan, and F. Abild-Pedersen. Toward controlled growth of helicity-specific carbon nanotubes. *J. Phys. Chem. Lett.*, 6(12):2232–2237, 2015.

[38] F. Ding, A. R. Harutyunyan, and B. I. Yakobson. Dislocation theory of chirality-controlled nanotube growth. *Proc. Natl. Acad. Sci.*, 106(8):2506–2509, 2009.

[39] W.-H. Chiang and R. M. Sankaran. Linking catalyst composition to chirality distributions of as-grown single-walled carbon nanotubes by tuning $\text{Ni}_x\text{Fe}_{1-x}$ nanoparticles. *Nat. Mater.*, 8(11):882–886, 2009.

[40] B. Wang, C. H. P. Poa, L. Wei, L.-j. Li, Y. Yang, and Y. Chen. (n,m) selectivity of single-walled carbon nanotubes by different carbon precursors on Co-Mo catalysts. *J. Am. Chem. Soc.*, 129(4):9014–9019, 2007.

[41] B. Liu, W. Ren, S. Li, C. Liu, and H.-M. Cheng. High temperature selective growth of single-walled carbon nanotubes with a narrow chirality distribution from a CoPt bimetallic catalyst. *Chem. Commun.*, 48(18):2409–2411, 2012.

[42] G. Rossi, A. Rapallo, C. Mottet, A. Fortunelli, F. Baletto, and R. Ferrando. Magic polyicosahedral core-shell clusters. *Phys. Rev. Lett.*, 93(10):105503, 2004.

[43] M. Aslan, J. B. A. Davis, and R. L. Johnston. Global optimization of small bimetallic Pd-Co binary nanoalloy clusters: a genetic algorithm approach at the DFT level. *Phys. Chem. Chem. Phys.*, 18(18):6676–6682, 2016.

[44] S. Reich, L. Li, and J. Robertson. Control the chirality of carbon nanotubes by epitaxial growth. *Chem. Phys. Lett.*, 421:469–472, 2006.

[45] D. Hedman, H. Reza Barzegar, A. Rosén, T. Wågberg, and J. Andreas Larsson. On the stability and abundance of single walled carbon nanotubes. *Sci. Rep.*, 5:16850, 2015.

[46] F. Yang, X. Wang, D. Zhang, J. Yang, D. Luo, Z. Xu, J. Wei, J.-Q. Wang, Z. Xu, F. Peng, X. Li, R. Li, Y. Li, M. Li, X. Bai, F. Ding, and Y. Li. Chirality-specific growth of single-walled carbon nanotubes on solid alloy catalysts. *Nature*, 510:522–524, 2014.

[47] D. A. Gomez-Gualdron, J. Zhao, and P. B. Balbuena. Nanocatalyst structure as a template to define chirality of nascent single-walled carbon nanotubes. *J. Chem. Phys.*, 134(1):014705, 2011.

[48] Y. Liu, A. Dobrinsky, and B. I. Yakobson. Graphene edge from armchair to zigzag: The origins of nanotube chirality? *Phys. Rev. Lett.*, 105(23):235502, 2010.

[49] D. Hedman and J. A. Larsson. Length dependent stability of single-walled carbon nanotubes and how it affects their growth. *Carbon*, 116:443–447, 2017.

[50] P. Larsson, J. A. Larsson, R. Ahuja, F. Ding, B. I. Yakobson, H. Duan, A. Rosén, and K. Bolton. Calculating carbon nanotube-catalyst adhesion strengths. *Phys. Rev. B*, 75(11):115419, 2007.

[51] F. Ding, P. Larsson, J. A. Larsson, R. Ahuja, H. Duan, A. Rosén, and K. Bolton. The importance of strong carbon-metal adhesion for catalytic nucleation of single-walled carbon nanotubes. *Nano Lett.*, 8:463–468, 2008.

[52] J. D. Baran, W. Kolodziejczyk, P. Larsson, R. Ahuja, and J. A. Larsson. On the stability of single-walled carbon nanotubes and their binding strengths. *Theor. Chem. Acc.*, 131:1270, 2012.

[53] E. C. Neyts, A. C. T. van Duin, and A. Bogaerts. Changing Chirality during Single-Walled Carbon Nanotube Growth : A Reactive Molecular Dynamics / Monte Carlo Study. *J. Am. Chem. Soc.*, 133:17225–17231, 2011.

[54] Q. Yuan, Z. Xu, B. I. Yakobson, and F. Ding. Efficient defect healing in catalytic carbon nanotube growth. *Phys. Rev. Lett.*, 108(24):245505, 2012.

[55] M. Liu, V. I. Artyukhov, H. Lee, F. Xu, and B. I. Yakobson. Carbyne from First Principles: Chain of C atoms, a Nanorod or a Nanorope? *ACS Nano*, 7:10075–10082, 2013.

[56] L. Shi, P. Rohringer, M. Wanko, A. Rubio, S. Waßerroth, S. Reich, S. Cambré, W. Wenseleers, P. Ayala, and T. Pichler. Electronic band gaps of confined

linear carbon chains ranging from polyyne to carbyne. *Phys. Rev. Mater.*, 1:075601, 2017.

[57] N. F. Andrade, T. L. Vasconcelos, C. P. Gouvea, B. S. Archanjo, C. A. Achete, Y. A. Kim, M. Endo, C. Fantini, M. S. Dresselhaus, and A. G. Souza Filho. Linear carbon chains encapsulated in multiwall carbon nanotubes: Resonance Raman spectroscopy and transmission electron microscopy studies. *Carbon*, 90:172–180, 2015.

[58] V. Scuderi, S. Scalese, S. Bagiante, G. Compagnini, L. D'Urso, and V. Privitera. Direct observation of the formation of linear C chain/carbon nanotube hybrid systems. *Carbon*, 47(8):2134–2137, 2009.

[59] W. A. Chalifoux and R. R. Tykwinski. Synthesis of polyynes to model the sp-carbon allotrope carbyne. *Nat. Chem.*, 2:967–971, 2010.

[60] M. Liu, V. I. Artyukhov, H. Lee, F. Xu, and B. I. Yakobson. Carbyne from first principles: chain of C atoms, a nanorod or a nanorope. *ACS Nano*, 7:10075–10082, 2013.

[61] L. Shi, P. Rohringer, K. Suenaga, Y. Niimi, J. Kotakoski, J. C. Meyer, H. Peterlik, M. Wanko, S. Cahangirov, A. Rubio, Z. J. Lapin, L. Novotny, P. Ayala, and T. Pichler. Confined linear carbon chains as a route to bulk carbyne. *Nat. Mater.*, 15(6):634–639, 2016.

[62] L. Sheng, A. Jin, L. Yu, K. An, Y. Ando, and X. Zhao. A simple and universal method for fabricating linear carbon chains in multiwalled carbon nanotubes. *Mater. Lett.*, 81:222–224, 2012.

[63] B. Pan, J. Xiao, J. Li, P. Liu, C. Wang, and G. Yang. Carbyne with finite length: The one-dimensional sp carbon. *Sci. Adv.*, 1(9):1–11, 2015.

[64] C. Jin, H. Lan, L. Peng, K. Suenaga, and S. Iijima. Deriving carbon atomic chains from graphene. *Phys. Rev. Lett.*, 102(20):1–4, 2009.

[65] C. Zhao, R. Kitaura, H. Hara, S. Irle, and H. Shinohara. Growth of linear carbon chains inside thin double-wall carbon nanotubes. *J. Phys. Chem. C*, 115(27):13166–13170, 2011.

[66] J. Zhang, Y. Feng, H. Ishiwata, Y. Miyata, R. Kitaura, J. E. P. Dahl, R. M. K. Carlson, H. Shinohara, and D. Tomanek. Synthesis and transformation of linear adamantine assemblies inside carbon nanotubes. *ACS Nano*, 6(10):8674–8683, 2012.

[67] K. Govaerts. *First-principles study of homologous series of layered Bi-Sb-Te-Se and Sn-O structures*. Doctoral dissertation, University of Antwerp, Belgium, 2015.

[68] M. Born and R. Oppenheimer. Zur Quantentheorie der Molekeln. *Ann. Phys.*, 84:4361, 1927.

[69] P. Hohenberg and W. Kohn. Inhomogeneous electron gas. *Phys. Rev.*, 136(B864-B871), 1964.

[70] W. Kohn and L. J. Sham. Self-Consistent Equations Including Exchange and Correlation Effects. *Phys. Rev.*, 140:A1133–A1138, 1965.

[71] D. S. Sholl and J. A. Steckel. *Density Functional Theory - A Practical Introduction*. John Wiley & Sons, Inc., Hoboken, New Jersey, USA, 2009.

[72] J. P. Perdew and Y. Wang. Accurate and simple analytic representation of the electron-gas correlation energy. *Phys. Rev. B*, 45:13244, 1992.

[73] J. P. Perdew, K. Burke, and M. Ernzerhof. Generalized Gradient Approximation Made Simple. *Phys. Rev. Lett.*, 77(18):3865–3868, 1996.

[74] H. Hellmann and F. Deuticke. Einführung in die Quantenchemie. *Angew. Chemie*, 54:156, 1937.

[75] R. P. Feynman. Forces in molecules. *Phys. Rev.*, 56:340–343, 1939.

[76] M. Bercx. *First-principles spectroscopic screening of materials for potential photovoltaic absorbers using the PBE functional*. Masters dissertation, University of Antwerp, Belgium, 2015.

[77] F. Bloch. Über die Quantenmechanik der Elektronen in Kristallgittern. *Zeitschrift für Phys.*, 52:555–600, 1929.

[78] P. E. Blöchl. Projector augmented-wave method. *Phys. Rev. B*, 50:17953, 1994.

[79] G. Kresse and D. Joubert. From ultrasoft pseudopotentials to the projector augmented-wave method. *Phys. Rev. B*, 59:1758, 1999.

[80] H. Dixit. *First-principles electronic structure calculations of transparent conducting oxide materials*. Doctoral dissertation, University of Antwerp, Belgium, 2012.

[81] F. Jensen. *Introduction to Computational Chemistry*. John Wiley & Sons Ltd, Chichester, UK, 2007.

[82] W. Greiner, L. Neise, and H. Stöcker. Number of microstates Omega and entropy S. In *Thermodyn. Stat. Mech.*, pages 123–141. Springer, New York, 1995.

[83] M. P. Allen. Introduction to molecular dynamics simulation. In N. Attig, K. Binder, H. Grubmüller, and K. Kremer, editors, *Comput. Soft Matter From Synth. Polym. to . . .*, volume 23, pages 1–28, Jülich, 2004. NIC-Directors.

[84] H. J. C. Berendsen, J. P. M. Postma, W. F. van Gunsteren, A. DiNola, and J. R. Haak. Molecular dynamics with coupling to an external bath. *J. Chem. Phys.*, 81:3684, 1984.

[85] H. C. Andersen. Molecular dynamics simulations at constant pressure and/or temperature. *J. Chem. Phys.*, 72:2384, 1980.

[86] S. Nosé. A unified formulation of the constant temperature molecular dynamics methods. *J. Chem. Phys.*, 81(1):511–519, 1984.

[87] W. G. Hoover. Canonical dynamics: Equilibrium phase-space distributions. *Phys. Rev. A*, 31(3):1695–1697, 1985.

[88] K. Bal. *New ways to bridge the gap between microscopic simulations and macroscopic chemistry*. Doctoral dissertation, University of Antwerp, Belgium, 2018.

[89] U. H. Hansmann. Parallel tempering algorithm for conformational studies of biological molecules. *Chem. Phys. Lett.*, 281(1-3):140–150, 1997.

[90] Y. Sugita and Y. Okamoto. Replica-exchange molecular dynamics method for protein folding. *Chem. Phys. Lett.*, 314(1-2):141–151, 1999.

[91] A. Laio and M. Parrinello. Escaping free-energy minima. *Proc. Natl. Acad. Sci.*, 99:12562–12566, 2002.

[92] M. R. Sørensen and A. F. Voter. Temperature-accelerated dynamics for simulation of infrequent events. *J. Chem. Phys.*, 112:9599–9606, 2000.

[93] A. F. Voter. A method for accelerating the molecular dynamics simulation of infrequent events. *J. Chem. Phys.*, 106:4665–4677, 1997.

[94] A. F. Voter. Parallel replica method for dynamics of infrequent events. *Phys. Rev. B*, 57:R13985–R13988, 1998.

[95] G. Kresse and J. Furthmüller. Efficiency of ab-initio total energy calculations for metals and semiconductors using a plane-wave basis set. *Comput. Mater. Sci.*, 6(1):15–50, jul 1996.

[96] G. Kresse and J. Furthmüller. Efficient iterative schemes for ab initio total-energy calculations using a plane-wave basis set. *Phys. Rev. B*, 54:11169, 1996.

[97] G. Kresse and J. Hafner. Ab initio molecular dynamics for liquid metals. *Phys. Rev. B*, 47:558, 1993.

[98] G. Kresse and J. Hafner. Ab initio molecular-dynamics simulation of the liquid-metal-amorphous-semiconductor transition in germanium. *Phys. Rev. B*, 49:14251, 1994.

[99] G. Kresse, M. Marsman, and J. Furthmüller. The VASP manual, 2019.

[100] B. Hammer, L. Hansen, and J. Nørskov. Improved adsorption energetics within density-functional theory using revised Perdew-Burke-Ernzerhof functionals. *Phys. Rev. B*, 59(11):7413–7421, 1999.

[101] M. Methfessel and A. T. Paxton. High-precision sampling for Brillouin-zone integration in metals. *Phys. Rev. B*, 40(6):3616–3621, 1989.

[102] A. C. T. van Duin, S. Dasgupta, F. Lorant, and W. A. Goddard. ReaxFF: A Reactive Force Field for Hydrocarbons. *J. Phys. Chem. A*, 105(41):9396–9409, 2001.

[103] C. Zou, Y. K. Shi, A. C. T. van Duin, H. Fang, and Z.-K. Liu. Molecular dynamics simulations of the effects of vacancies on nickel self-diffusion, oxygen diffusion and oxidation initiation in nickel, using the ReaxFF reactive force field. *Acta Mater.*, 83:102–112, 2015.

[104] G. Bussi, D. Donadio, and M. Parrinello. Canonical sampling through velocity-rescaling. *J. Chem. Phys.*, 126:014101, 2007.

[105] K.-M. Ho, C.-L. Fu, B. N. Harmon, W. Weber, and D. R. Hamann. Vibrational Frequencies and Structural Properties of Transition Metals via Total-Energy Calculations. *Phys. Rev. Lett.*, 49(9):673–676, 1982.

[106] C.-L. Fu and K.-M. Ho. First-principles calculation. *Phys. Rev. B*, 28(10):5480–5486, 1983.

[107] A. Rapallo, G. Rossi, R. Ferrando, A. Fortunelli, B. C. Curley, L. D. Lloyd, G. M. Tarbuck, and R. L. Johnston. Global optimization of bimetallic cluster structures. I. Size-mismatched Ag-Cu, Ag-Ni, and Au-Cu systems. *J. Chem. Phys.*, 122(19):194308, 2005.

[108] G. Rossi, R. Ferrando, A. Rapallo, A. Fortunelli, B. C. Curley, L. D. Lloyd, and R. L. Johnston. Global optimization of bimetallic cluster structures. II. Size-matched Ag-Pd, Ag-Au, and Pd-Pt systems. *J. Chem. Phys.*, 122(19):194309, 2005.

[109] D. A. Kilimis and D. G. Papageorgiou. Density functional study of small bimetallic Ag-Pd clusters. *J. Mol. Struct. THEOCHEM*, 939(1-3):112–117, 2010.

[110] C. Song, Q. Ge, and L. Wang. DFT studies of Pt/Au bimetallic clusters and their interactions with the CO molecule. *J. Phys. Chem. B*, 109(47):22341–22350, 2005.

[111] Q. Ge, C. Song, and L. Wang. A density functional theory study of CO adsorption on Pt-Au nanoparticles. *Comput. Mater. Sci.*, 35(3):247–253, 2006.

[112] P. B. Balbuena, D. Altomare, N. Vadlamani, S. Bingi, L. A. Agapito, and J. M. Seminario. Adsorption of O, OH, and H2O on Pt-based bimetallic clusters alloyed with Co, Cr, and Ni. *J. Phys. Chem. A*, 108(30):6378–6384, 2004.

[113] W. H. Qi and S. T. Lee. Phase stability, melting, and alloy formation of Au-Ag bimetallic nanoparticles. *J. Phys. Chem. C*, 114(21):9580–9587, 2010.

[114] S.-P. Huang and P. B. Balbuena. Melting of bimetallic Cu-Ni nanoclusters. *J. Phys. Chem. B*, 106:7225–7236, 2002.

[115] J. I. Park, M. G. Kim, Y. W. Jun, J. S. Lee, W. R. Lee, and J. Cheon. Characterization of superparamagnetic core-shell nanoparticles and monitoring their anisotropic phase transition to ferromagnetic solid solution nanoalloys. *J. Am. Chem. Soc.*, 126(29):9072–9078, 2004.

[116] W. L. Zhou, E. E. Carpenter, J. Lin, A. Kumbhar, J. Sims, and C. J. O'Connor. Nanostructures of gold coated iron core-shell nanoparticles and the nanobands assembled under magnetic field. *Eur. Phys. J. D*, 16:289–292, 2001.

[117] J. P. Wilcoxon and P. P. Provencio. Heterogeneous growth of metal clusters from solutions of seed nanoparticles. *J. Am. Chem. Soc.*, 126(20):6402–6408, 2004.

[118] R. Ferrando, J. Jellinek, and R. L. Johnston. Nanoalloys: From theory to applications of alloy clusters and nanoparticles. *Chem. Rev.*, 108(3):846–904, 2008.

[119] A. E. Russel and A. Rose. X-ray absorption spectroscopy of low temperature fuel cell catalysts. *Chem. Rev.*, 104(10):4613–4636, 2004.

[120] U. A. Paulus, A. Wokaun, G. G. Scherer, T. J. Schmidt, V. Stamenkovic, V. Radmilovic, N. M. Markovic, and P. N. Ross. Oxygen reduction on carbon-supported Pt-Ni and Pt-Co alloy catalysts. *J. Phys. Chem. B*, 106(41):4181–4191, 2002.

[121] I. D. Enache, J. K. Edwards, P. Landon, B. Solsona-Espriu, A. F. Carley, A. A. Herzing, M. Watanabe, C. J. Kiely, D. W. Knight, and G. J. Hutchings. Solvent-free oxidation of primary alcohols to aldehydes using Au-Pd/TiO2 catalysts. *Science*, 311(5759):362–365, 2006.

[122] Z. L. Liu, X. Y. Ling, X. D. Su, and J. Y. Lee. Carbon-supported Pt and PtRu nanoparticles as catalysts for a direct methanol fuel cell. *J. Phys. Chem. B*, 108(24):8234–8240, 2004.

[123] Y. Takasu, H. Itaya, T. Kawaguchi, W. Sugimoto, and Y. Murakami. Characteristics of highly active PtRu/C anode catalysts for DMFC. *Stud. Surf. Sci. Catal.*, 145:279–282, 2003.

[124] Y. Engelmann, A. Bogaerts, and E. C. Neyts. Thermodynamics at the nanoscale: Phase diagrams of nickel-carbon nanoclusters and equilibrium constants for phase transition. *Nanoscale*, 6(20):11981–11987, 2014.

[125] Y. Magnin, A. Zappelli, H. Amara, F. Ducastelle, and C. Bichara. Size dependent phase diagrams of nickel-carbon nanoparticles. *Phys. Rev. Lett.*, 115(20):205502, 2015.

[126] B. Chen, S. Li, H. Imai, L. Jia, J. Umeda, M. Takahashi, and K. Kondoh. Load transfer strengthening in carbon nanotubes reinforced metal matrix composites via in-situ tensile tests. *Compos. Sci. Technol.*, 113:1–8, 2015.

[127] N. R. Wilson and J. V. Macpherson. Carbon nanotube tips for atomic force microscopy. *Nat. Nanotechnol.*, 4:483–491, 2009.

[128] R. Das, M. E. Ali, S. B. A. Hamid, S. Ramakrishna, and Z. Z. Chowdhury. Carbon nanotube membranes for water purification: A bright future in water desalination. *Desalination*, 336(1):97–109, 2014.

[129] C. H. Lee, N. Johnson, J. Drelich, and Y. K. Yap. The performance of superhydrophobic and superoleophilic carbon nanotube meshes in water-oil filtration. *Carbon*, 49(2):669–676, 2011.

[130] L. Li, S. Reich, and J. Robertson. Ab Initio Simulations of the Nucleation of Single-Walled Carbon Nanotubes. *Solid State Phenom.*, 121-123:1037–1040, 2007.

[131] H. Amara, C. Bichara, and F. Ducastelle. Understanding the nucleation mechanisms of carbon nanotubes in catalytic chemical vapor deposition. *Phys. Rev. Lett.*, 100(5):056105, 2008.

[132] M. Diarra, A. Zappelli, H. Amara, F. Ducastelle, and C. Bichara. Importance of carbon solubility and wetting properties of nickel nanoparticles for single wall nanotube growth. *Phys. Rev. Lett.*, 109(18):185501, 2012.

[133] A. Jiang, N. Awasthi, A. N. Kolmogorov, W. Setyawan, A. Börjesson, K. Bolton, A. R. Harutyunyan, and S. Curtarolo. Theoretical study of the thermal behavior of free and alumina-supported Fe-C nanoparticles. *Phys. Rev. B*, 75(20):205426, 2007.

[134] O. V. Yazyev and A. Pasquarello. Effect of metal elements in catalytic growth of carbon nanotubes. *Phys. Rev. Lett.*, 100(15):156102, 2008.

[135] I. V. Yudanov, K. M. Neyman, and N. Rosch. Density functional study of Pd nanoparticles with subsurface impurities of light element atoms. *Phys. Chem. Chem. Phys.*, 6:116–123, 2004.

[136] F. Ding, A. Rosen, and K. Bolton. Molecular dynamics study of the catalyst particle size dependence on carbon nanotube growth. *J. Chem. Phys.*, 121(6):2775–2779, 2004.

[137] H. R. Barzegar, F. Nitze, T. Sharifi, M. Ramstedt, C. W. Tai, A. Malolepszy, L. Stobinski, and T. Wagberg. Simple dip-coating process for the synthesis of small diameter single-walled carbon nanotubes-effect of catalyst composition and catalyst particle size on chirality and diameter. *J. Phys. Chem. C*, 116(22):12232–12239, 2012.

[138] R. Rao, K. G. Eyink, and B. Maruyama. Single-walled carbon nanotube growth from liquid gallium and indium. *Carbon*, 48(13):3971–3973, 2010.

[139] L. Yuliati, H. Itoh, and H. Yoshida. Photocatalytic conversion of methane and carbon dioxide over gallium oxide. *Chem. Phys. Lett.*, 452(1-3):178–182, 2008.

[140] F. F. De Sousa, H. S. A. De Sousa, M. C. C. Junior, A. P. Ayala, E. B. Barros, B. C. Viana, J. M. Filho, and A. C. Oliveira. Nanostructured Ni-containing spinel oxides for the dry reforming of methane: Effect of the presence of cobalt and nickel on the deactivation behaviour of catalysts. *Int. J. Hydrogen Energy*, 37(4):3201–3212, 2012.

[141] G. de Souza, N. R. Marcilio, and O. W. Perez-Lopez. Dry reforming of methane at moderate temperatures over modified Co-Al co-precipitated catalysts. *Mater. Res.*, 17(4):1047–1055, 2014.

[142] I. V. Vernyhora, V. Tatarenko, and S. M. Bokoch. Thermodynamics of fcc-NiFe alloys in a static applied magnetic field. *ISRN Thermodyn.*, 212:917836, 2012.

[143] B. Predel. Ga-Ni (Gallium-Nickel). In O. Madelung, editor, *Ga-Gd – Hf-Zr, Vol. 5 Ser. Landolt-Börnstein - Gr. IV Phys. Chem.*, chapter Ga-Ni, pages 1–4. Springer Berlin Heidelberg, Berlin, 1996.

[144] H. Okamoto. The Fe-Ga (iron-gallium) system. *Bull. Alloy Phase Diagrams*, 11(6):576–581, 1990.

[145] D. S. Sholl and J. A. Steckel. Ab inito molecular dynamics. In *Density Funct. Theory - A Pract. Introd.*, chapter Ab initio, pages 198–200. John Wiley & Sons, Inc., Hoboken, New Jersey, 2009.

[146] C. Kittel. *Introduction to solid state physics*, volume 3. John Wiley & Sons, Inc., Hoboken, New Jersey, 8 edition, 2005.

[147] R. D. Shannon and C. T. Prewitt. Effective ionic radii in oxides and fluorides. *Acta Crystallogr. Sect. B*, 25:925–946, 1969.

[148] R. D. Shannon. Revised effective ionic radii and systematic studies of interatomic distances in halides and chalcogenides. *Acta Crystallogr. Sect. A*, 32(5):751–767, 1976.

[149] F. Aqra and A. Ayyad. Surface energies of metals in both liquid and solid states. *Appl. Surf. Sci.*, 257(15):6372–6379, 2011.

[150] L. Vitos, A. V. Ruban, H. L. Skriver, and J. Kollár. The surface energy of metals. *Surf. Sci.*, 411:186–202, 1998.

[151] Y. Shibuta, Y. Watanabe, and T. Suzuki. Growth and melting of nanoparticles in liquid iron: A molecular dynamics study. *Chem. Phys. Lett.*, 475(4-6):264–268, 2009.

[152] E. C. Neyts and A. Bogaerts. Numerical study of the size-dependent melting mechanisms of nickel nanoclusters. *J. Phys. Chem. C*, 113:2771–2776, 2009.

[153] L. L. Wang and D. D. Johnson. Density functional study of structural trends for late-transition-metal 13-atom clusters. *Phys. Rev. B*, 75(23):1–10, 2007.

[154] Z. Li, J. A. Larsson, P. Larsson, R. Ahuja, J. M. Tobin, J. O'Byrne, M. A. Morris, G. Attard, and J. D. Holmes. Copper / Molybdenum Nanocomposite Particles as Catalysts for the Growth of Bamboo-Structured Carbon Nanotubes. *J. Phys. Chem. C*, 112:12201–12206, 2008.

[155] J. P. O'Byrne, Z. Li, J. M. Tobin, J. A. Larsson, P. Larsson, R. Ahuja, and J. D. Holmes. Growth of carbon nanotubes from heterometallic palladium and copper catalysts. *J. Phys. Chem. C*, 114(18):8115–8119, 2010.

[156] A. Ghysels, T. Verstraelen, K. Hemelsoet, M. Waroquier, and V. Van Speybroeck. TAMkin: A versatile package for vibrational analysis and chemical kinetics. *J. Chem. Inf. Model.*, 50(9):1736–1750, 2010.

[157] Y. Li, R. Ahuja, and J. A. Larsson. Communication: Origin of the difference between carbon nanotube armchair and zigzag ends. *J. Chem. Phys.*, 140(9):091102, 2014.

[158] A. Börjesson and K. Bolton. First principles studies of the effect of nickel carbide catalyst composition on carbon nanotube growth. *J. Phys. Chem. C*, 114:18045–18050, 2010.

[159] J. E. Mueller, A. C. T. van Duin, and W. A. Goddard. Development and Validation of ReaxFF Reactive Force Field for Hydrocarbon Chemistry Catalyzed by Nickel. *J. Phys. Chem. C*, 114(11):4939–4949, 2010.

[160] R. J. Lagow, J. J. Kampa, H.-C. Wei, S. L. Battle, J. W. Genge, D. A. Laude, C. J. Harper, R. Bau, R. C. Steven, J. F. Haw, and E. Munson. Synthesis of linear Acetylenic Carbon: The “sp” Carbon Allotrope. *Science*, 267(5196):362–367, 1995.

[161] C. S. Casari and A. Milani. Carbyne: From the elusive allotrope to stable carbon atom wires. *MRS Commun.*, 8(2):207–219, 2018.

[162] S. Heeg, L. Shi, L. V. Poulikakos, T. Pichler, and L. Novotny. Carbon Nanotube Chirality Determines Properties of Encapsulated Linear Carbon Chain. *Nano Lett.*, 18(9):5426–5431, 2018.

[163] Y. Zhu, H. Bai, and Y. Huang. Electronic property modulation of one dimensional extended graphdiyne nanowires from a first-principle crystal orbital view. *ChemistryOpen*, 5:78–87, 2016.

[164] W. Q. Neves, R. S. Alencar, R. S. Ferreira, A. C. Torres-Dias, N. F. Andrade, A. San-Miguel, Y. A. Kim, M. Endo, D. W. Kim, H. Muramatsu, A. L. Aguiar, and A. G. Souza Filho. Effects of pressure on the structural and electronic properties of linear carbon chains encapsulated in double wall carbon nanotubes. *Carbon*, 133:446–456, 2018.

[165] X. Zhao, Y. Ando, Y. Liu, M. Jinno, and T. Suzuki. Carbon Nanowire Made of a Long Linear Carbon Chain Inserted Inside a Multiwalled Carbon Nanotube. *Phys. Rev. Lett.*, 90:187401, 2003.

[166] D. W. Boukhvalov, I. S. Zhidkov, E. Z. Kurmaev, E. Fazio, S. O. Cholakh, and L. D’Urso. Atomic and electronic structures of stable linear carbon chains on Ag-nanoparticles. *Carbon*, 128:296–301, 2018.

[167] E. Kano, A. Hashimoto, and M. Takeguchi. In-situ TEM Observation of Pt-terminating Carbyne on Graphene. *Microsc. Microanal.*, 20(S3):1742–1743, 2014.

[168] Q. Sun, L. Cai, S. Wang, R. Widmer, H. Ju, J. Zhu, L. Li, Y. He, P. Ruffieux, R. Fasel, and W. Xu. Bottom-Up Synthesis of Metalated Carbyne. *J. Am. Chem. Soc.*, 138(4):1106–1109, 2016.

[169] M. Kijima, Y. Sakai, and H. Shirakawa. Electrochemical synthesis of carbyne catalyzed by nickel complex. *Synth. Met.*, 71:1837–1840, 1995.

[170] W. A. Chalifoux and R. R. Tykwinski. Synthesis of polyynes to model the sp-carbon allotrope carbyne. *Nat. Chem.*, 2:967–971, 2010.

[171] J. R. Rostrup-Nielsen. Production of synthesis gas. *Catal. Today*, 18(4):305–324, 1993.

[172] H. Schulz. Short history and present trends of Fischer-Tropsch synthesis. *Appl. Catal. A Gen.*, 186:3–12, 1999.

[173] G. Chen, S. Bandow, E. R. Margine, C. Nisoli, A. N. Kolmogorov, V. H. Crespi, R. Gupta, G. U. Sumanasekera, S. Iijima, and P. C. Eklund. Chemically Doped Double-Walled Carbon Nanotubes: Cylindrical Molecular Capacitors. *Phys. Rev. Lett.*, 90:257403, 2003.

[174] H. Shiozawa, A. Briones-Leon, O. Domanov, G. Zechner, Y. Sato, K. Suenaga, T. Saito, M. Eisterer, E. Weschke, W. Lang, H. Peterlik, and T. Pichler. Nickel clusters embedded in carbon nanotubes as high performance magnets. *Sci. Rep.*, 5:15033, 2015.

[175] Y. Deng and S. W. Cranford. Mapping temperature and confinement dependence of carbyne formation within carbon nanotubes. *Carbon*, 141:209–217, 2019.

[176] J. P. Perdew, K. Burke, and M. Ernzerhof. Erratum: Generalized Gradient Approximation Made Simple. *Phys. Rev. Lett.*, 78:1396, 1997.

[177] A. Tkatchenko and M. Scheffler. Accurate Molecular van Der Waals Interactions from Ground-State Electron Density and Free-Atom Reference Data. *Phys. Rev. Lett.*, 102:073005, 2009.

[178] G. A. Henkelman, B. P. Uberuaga, and H. Jonsson. Climbing Image Nudged Elastic Band Method for Finding Saddle Points and Minimum Energy Paths. *J. Chem. Phys.*, 113(2):9901–9904, 2000.

[179] S. Lehwald and H. Ibach. Decomposition of hydrocarbons on flat and stepped Ni(111) surfaces. *Surf. Sci.*, 89:425–445, 1979.

[180] A. Timoshevskii, S. Kotrechko, and Y. Matviychuk. Atomic structure and mechanical properties of carbyne. *Phys. Rev. B*, 91:245434, 2015.

[181] S. E. Muller and A. K. Nair. Carbyne as a fiber in metal-matrix nanocomposites: A first principle study. *Comput. Mater. Sci.*, 159(187-193), 2019.

[182] J. A. Januszewski and R. R. Tykwinski. Synthesis and properties of long [n]cumulenes ($n \geq 5$). *Chem. Soc. Rev.*, 43(9):3184–3203, 2014.

[183] V. I. Artyukhov, M. Liu, and B. I. Yakobson. Mechanically induced metal-insulator transition in carbyne. *Nano Lett.*, 14(8):4224–4229, 2014.

[184] C. Ming, F. X. Meng, X. Chen, J. Zhuang, and X. J. Ning. Tuning the electronic and optical properties of monatomic carbon chains. *Carbon*, 68:487–492, 2014.

[185] Vlaams Supercomputer Centrum - Our offer - Infrastructure, 2019.

[186] Vlaams Supercomputer Centrum - Project access Tier-1, 2019.